A. R. A. P.

AERONAUTICAL RESEARCH ASSOCIATES *of* PRINCETON, INC.

DISCLAIMER NOTICE

THIS DOCUMENT IS THE BEST QUALITY AVAILABLE.

COPY FURNISHED CONTAINED A SIGNIFICANT NUMBER OF PAGES WHICH DO NOT REPRODUCE LEGIBLY.

HYPERVELOCITY KILL MECHANISMS PROGRAM

ARPA Order No. 149-60

Aerothermal Phase

ARAP REPORT NO. 64

EXPERIMENTS ON THE OBLIQUE IMPINGEMENT OF UNDEREXPANDED JETS ON A FLAT PLATE

by

Richard S. Snedeker

and

Coleman duP. Donaldson

This research was supported by the Advanced Research Projects Agency, Ballistic Missile Defense Systems Branch, and was monitored by the U.S. Naval Research Laboratory (Code 6240) under Contract No. Nonr-390(00)(X).

Aeronautical Research Associates of Princeton, Inc.

50 Washington Road, Princeton, New Jersey

April 1965

ABSTRACT

An experimental investigation was made of the general behavior of an air jet impinging obliquely on a circular flat plate. Surface pressure distributions and velocity profiles of the resulting wall jet were measured. Typical stagnation point radial velocity gradients, their dependence on impingement angle, and their correlation with local free jet properties were also determined. Throughout the range of impingement angles studied ($90^\circ \geq \alpha \geq 45^\circ$), the wall jet thickness was found to be relatively constant around the plate perimeter. The azimuthal variation of momentum flux per radian depended strongly on impingement angle and only slightly on jet strength and impingement distance.

TABLE OF CONTENTS

PREFACE

This report presents the results of an experimental study of the behavior of jet flows which impinge obliquely on a flat plate. The work was performed as a part of ARAP's basic experimental program under the Aerothermal Phase of the Hypervelocity Kill Mechanisms Program. The primary aim of these studies has been to aid in the understanding of basic jet impingement effects under a wide range of conditions analogous to those which might occur in the interior of a punctured reentry vehicle. The detailed results of that portion of these studies dealing with free jet characteristics and normal impingement have been given in [1]. Since the present report on oblique impingement effects is intended to be a complement to this earlier report, the discussion herein of topics common to both is somewhat less detailed. Together, the two reports cover ARAP's complete experimental jet impingement program.

1. INTRODUCTION

The results of an experimental investigation of the properties of free and impinging underexpanded jets from a convergent nozzle have been reported elsewhere [1]. In that study, surface pressure distributions were measured for the normal impingement of jets under a variety of conditions determined by jet strength, impingement distance, and surface shape. By making use of highly detailed pressure distribution measurements in the stagnation region, the stagnation point heat transfer parameter $(du_e/dr)_{r=0}$ was evaluated for each case. A concurrent study of the free jet alone provided data for determining the degree of correlation between values of $(du_e/dr)_{r=0}$ and the local free jet properties. For this case, because of axial symmetry, a knowledge of $(du_e/dr)_{r=0}$ based on the pressure distribution measured along a single diameter through the stagnation point was sufficient to estimate the heat transfer characteristics of the entire impinging and wall jet flow by means of standard boundary layer analysis techniques.

The present report covers the results of an extension of the earlier work to cases of oblique impingement. The study was limited to impingement on a flat plate so that the effects of surface shape revealed in [1] were not determined. The impingement angle α was varied in most cases from normal impingement $(\alpha = 90^\circ)$ to a minimum oblique angle of 45°. Because of the asymmetry introduced under such conditions, the problem of estimating the distribution of heat transfer on the surface is more complex. In this case, a true stagnation point heat transfer parameter cannot be represented by the value of $(du_e/dr)_{r=0}$ measured along a single diameter since there is an azimuthal variation of the pressure distribution upon which this gradient depends.

Thus, for example, different values of $(du_e/dr)_{r=0}$ would be expected to result from pressure distributions measured along diameters normal and parallel to the plate's tilt axis. It is also necessary that the azimuthal distributions of momentum and energy flux in the resulting radial wall jet be known in order to determine the heat transfer on the surface away from the stagnation point. Knowledge of these distributions is also useful in cases where the wall jet itself impinges on a bounded surface.

In the experimental program about to be described, the wall jet flux distributions were found for each of several impingement conditions on the basis of velocity profiles measured at a number of points along the plate perimeter. Measurements of the stagnation point pressure distributions, however, were made only along a diameter normal to the plate tilt axis and so were not sufficient to compute the true heat transfer parameter. Nevertheless, values of the radial velocity gradient were computed from these distributions in order to provide a measure of the effects of obliqueness. This gradient is designated by $[(du_e/dr)_{r=0}]_1$ in order to distinguish it from the value $(du_e/dr)_{r=0}$ which has been used to represent the actual stagnation point heat transfer parameter for normal impingement.

The importance of considering certain secondary factors when interpreting measured jet characteristics has been discussed in [1]. Such factors include the effects of obstructions in the entrained flow field, as well as the overall stability of the jet proper. Since the present measurements were made with the same apparatus, it is clear that similar factors apply in this case, although a quantitative estimate of their importance has not been attempted. In particular, it

appears that the obliqueness of the impingement plate can produce a varying degree of asymmetry in the entrained flow which, because of the "closed-loop" nature of the flow system, can in turn affect the impingement process itself. Thus, for example, the measured change in location of the stagnation point due to a change in impingement angle may be a function not only of the uniqueness of the experimental setup, but also of the degree of asymmetry produced in the entrained flow at each impingement angle.

While there have been numerous previous investigations of impinging jet flows (see [1], Cited References), very few have been concerned with the normal or oblique impingement of underexpanded jets. Of these few, only [2, 3, and 4] represent cases which have a close bearing on the present problem. In [2], the exhaust from a rocket engine was impinged on a flat surface at small impingement angles ($\alpha \ll 90^{\circ}$), and a limited number of velocity profiles were measured in the resulting deflected jet. A more pertinent set of measurements is to be found in [3] wherein air jets of several supersonic Mach numbers were impinged upon a circular flat plate. Pressure distributions on the plate surface were measured for a wide range of impingement angles at several axial locations in the jet. Air jets from several underexpanded supersonic nozzles were used in [4] for a study of interaction effects on a simulated lunar surface. Limited data for slightly oblique impingement cases are presented. The impingement of the edge of an underexpanded jet on a flat surface held parallel to its axis is the subject of another report [5] having a less direct bearing in this instance. Several other cases of pressure distribution measurements for obliquely impinging low subsonic jets are to be found in the literature of the V/STOL field.

2.1. Basic flow characteristics.

The flow field produced by the impingement of a turbulent, axially symmetric air jet against a flat surface whose diameter is large compared to that of the jet is conveniently described in terms of three flow regimes as follows:

(1) The free jet regime upstream of any strong local interaction effects due to impingement.

(2) The impingement regime wherein the interaction of the jet with the impingement surface produces a change in flow direction.

(3) The wall jet regime consisting of essentially radial flow along the surface beyond the point at which the strong interactions of impingement cause any local effects.

Although these three regimes can be considered separately because of certain basic differences, they are not, of course, independent; even the flow leaving the plate edge in the wall jet determines to some extent the distribution of the impinging jet entrainment flow, especially when the entire region is closely confined by solid boundaries. The flow regimes are illustrated schematically in Figure 1, which also serves to define the quantities of interest.

The free jets used in this study were of three types, each representing one of the basic flow conditions possible for a convergent nozzle. These jets were the same as those used in the earlier study of normal impingement, i.e. a subsonic jet ($p_\infty/p^o_{sc} = .800$), a moderately underexpanded jet ($p_\infty/p^o_{sc} = .372$), and a highly underexpanded jet ($p_\infty/p^o_{sc} = .148$). The basic features of each type are shown in Figure 2. It is seen that the primary difference between the two underexpanded jets lies in the existence of a normal shock

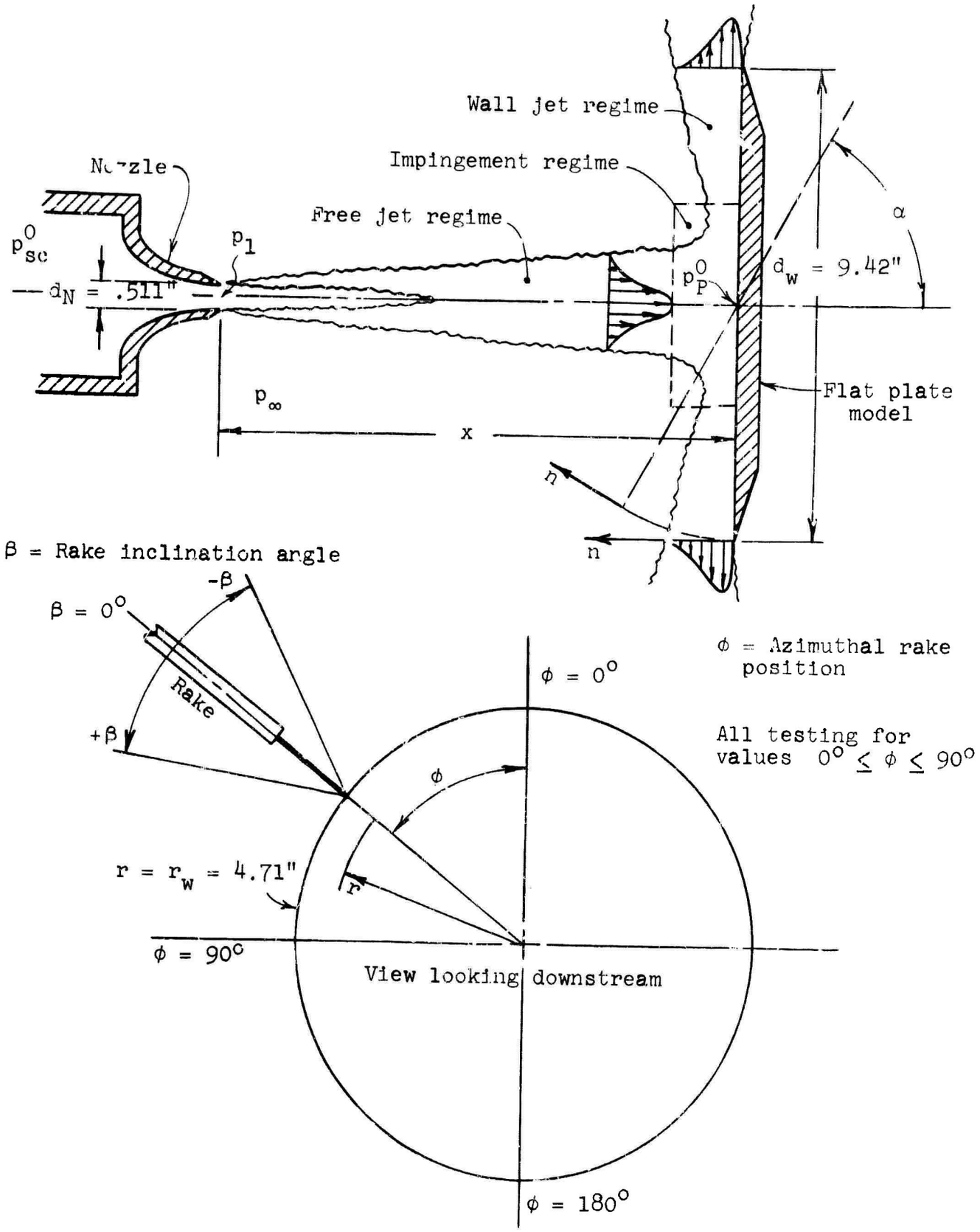

Figure 1. Schematic views of test setup showing notation used.

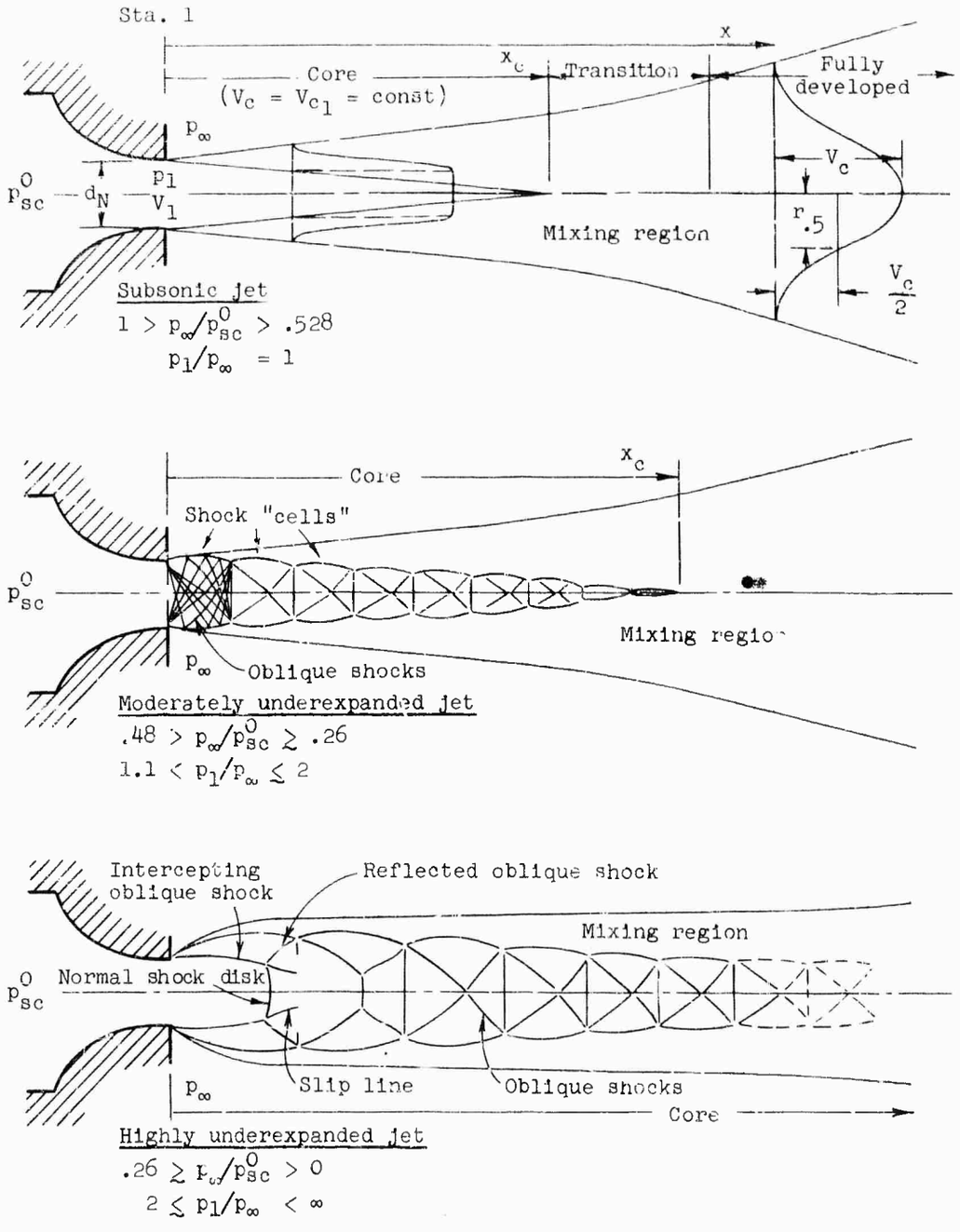

Figure 2. Three major variations of jet flow from a convergent nozzle.

disk for the stronger jet. Pressure distributions resulting from the impingement of the core region of such jets show a marked dependence on the exact local conditions as determined by the shock structure. Large radial pressure gradients can occur in this region which for at least one type of jet can cause separation of the flow along the surface. Such a condition has been observed near the stagnation point for the impingement at close range of a highly underexpanded jet where the flow just downstream of the normal shock disk is subsonic while the surrounding flow is supersonic [1]. In the wall jet regime, the flow can be thought of as consisting of an inner boundary layer-like region and an outer free mixing region. Because of the action of the laminar sublayer at the wall, however, the velocity profiles of the boundary layer and free shear layer portions develop at different rates thus preventing the formation of an exactly self-similar velocity profile for the entire wall jet.

When the impingement angle is made oblique, more mass and momentum flux are concentrated in the downstream direction. There is also a shift of the stagnation point in the upstream direction. For a two-dimensional or axially symmetric flow, it can be shown that this is a result of the manner in which the mass and momentum fluxes are distributed in each direction. At the same time, the angle at which the stagnation streamline impinges remains normal to the surface. It is clear that such a condition will produce radial pressure distributions which vary with azimuthal position about the stagnation point. The distribution will be symmetric along a diameter parallel to the tilt axis ($\phi = 90^{\circ}$ and 270°) and will become increasingly asymmetric for diameters approaching that normal to the tilt axis ($\phi = 0^{\circ}$

and 180°). Under such conditions a velocity gradient based on only one of these distributions is insufficient to define completely the heat transfer. In the present experiments, it was possible to measure the distribution only for $\phi = 0^\circ$ and 180°. Thus the computed stagnation point velocity gradients $[(du_e/dr)_{r=0}]_1$ must be thought of as only indicative of changes in the actual heat transfer. However, the asymmetry present in the measured distributions for these cases can be shown to be of large scale compared to that of the stagnation point boundary layer so that the analysis used to relate the radial velocity gradient to the curvature of the local pressure distribution remains valid. Using a characteristic value of $(du_e/dr)_{r=0} = 10^4 \text{sec}^{-1}$ found for normal impingement, we have

$$\delta_{r=0} = \sqrt{\nu/a} = .0036 \text{ inch}$$

where $a = (du_e/dr)_{r=0}$. Although the pressure distributions in the present study are less precise than those measured for normal impingement, they are sufficiently detailed to show little if any asymmetry at distances as great as $20\delta_{r=0}$ from the stagnation point. Thus the expression used to relate the pressure distributions and the radial velocity gradient can be the same as that derived in [1] for normal impingement, with the restriction that it does not define the true stagnation point heat transfer. The relation is as follows:

$$\left[\left(\frac{du_e}{dr}\right)_{r=0}\right]_1 = \sqrt{\frac{2R}{r_w^2}}\sqrt{\frac{T^o}{(r/r_w)^2}\left(1 - \frac{p}{p_p^o}\right)} \qquad (1)$$

where p_p^o is the surface pressure at the stagnation point, T^o is the flow stagnation temperature, r_w is the wetted radius of the plate, and R is the specific gas constant.

2.2. Apparatus and Instrumentation.

The impinging air jet used in these experiments issued from a convergent circular nozzle with an exit diameter d_N = .511 inch. The nozzle was mounted on a 4.75-inch i.d. settling chamber which was supplied with air from a storage tank through an automatic regulator valve. A maximum settling chamber stagnation pressure of 125 psig was available. The flat plate impingement model was of aluminum, 1/2 inch thick and 9.42 inches in diameter. There were 27 surface pressure taps along the vertical diameter and 15 along the horizontal diameter. The four taps just above the center were spaced 1/16 inch apart. The remaining holes had coarser spacing, but were located symmetrically with respect to the center. Several pairs of these outer holes were used to make plate alignment checks with respect to the flow by nulling the pressure difference between them. The lateral and vertical positions of the plate were controlled by means of screw adjustments built into the mount. The axial distance was changed by sliding the plate and its mounting structure along a pair of steel angle rails affixed to the settling chamber mounting stand. The plate was mounted on a pivoting steel tube in such a way that the pivot axis passed along the plate surface through its center. A jack screw was used to adjust the impingement angle. With this arrangement, the position of the plate center tap remained fixed for all impingement angles. The nozzle and plate assembly just described was the same as that used in the detailed study of normal impingement reported in [1]. The setup is shown in Figure 3.

For the purpose of determining the azimuthal distribution of the wall jet, velocity profiles were measured at the edge of the plate by means of a total head rake.

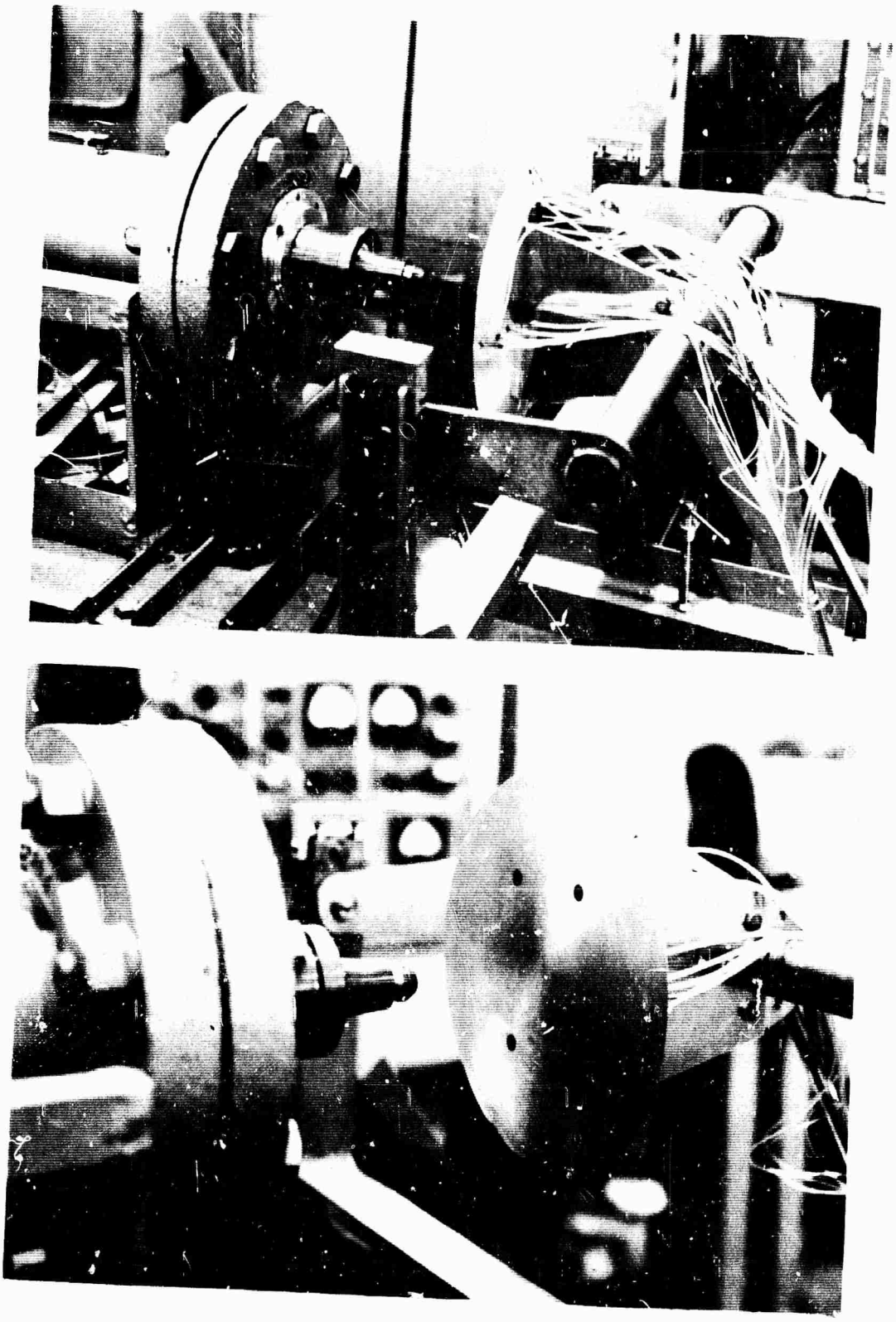

Figure 3. Views of convergent nozzle and flat plate apparatus.

This rake consisted of eight parallel tubes, each of .032-inch o.d. stainless steel tubing and mounted 3/16 inch apart. The rake was held on a quadrant to the rear of the model in such a way that it could be located along the plate perimeter anywhere between $\phi = 0^\circ$ and 90° (see Figure 1 for definition of ϕ). Thus the rake tilted with the plate when the impingement angle α was changed. A screw adjustment provided travel of the rake in a direction n normal to the plate surface. In addition, it was possible to pivot the rake about a line through the tips of the total head tubes so that an accurate measure could be made of any flow leaving the plate in a nonradial direction. In order to determine the true direction of any such nonradial flow, a direction-sensitive wedge-type probe was mounted at one end of the rake. The rake assembly is shown in position on the plate in Figure 4.

Pressures were measured by means of liquid manometers or Bourdon-type test gauges according to the pressure level involved. The settling chamber stagnation temperature T°_{sc} was taken to be equal to the ambient air temperature T_∞, an assumption which was found to be valid during the earlier part of the program when T°_{sc} was measured directly.

2.3. Results of Pressure Distribution Measurements and Photographic Studies.

2.3.1. Pressure distributions. The program of pressure distribution measurements consisted of 12 basic jet strength-impingement distance combinations. Each of the three types of jet already described was impinged on the flat plate at four different axial locations. In terms of nozzle diameters downstream of the nozzle exit, these distances were $x/d_N = 1.96$, 7.32, 23.5 and 39.1. (For

Figure 4. Wall jet rake in position on flat plate.

the subsonic (p_∞/p^o_{sc} = .800) and moderately underexpanded (p_∞/p^o_{sc} =.372) jets, x/d_N = 1.96 falls in the core region, x/d_N = 7.32 is near the end of the core, and x/d_N = 23.5 and 39.1 are in the fully developed region. The core of the highly underexpanded jet (p_∞/p^o_{sc} = .148) probably extends beyond x/d_N = 23.5 .) The effect of changing the angle of impingement was then observed for each of those 12 impingement conditions. In general, impingement angles of 90°, 75°, 60°, and 45° were used. In a few cases, angles of 30° and 15° were tried, although little useful information resulted.

In order to obtain the greatest possible detail near the stagnation point and to trace its movement with α, a special procedure was required. The high resolution distributions obtained in the earlier study of normal impingement by means of a model translation technique could not be duplicated in the present case without the application of cumbersome α-dependent corrections to specify the exact location of each pressure tap for each run since the model pivot axis translated with the model. In view of the large number of runs to be made, it was decided to measure each distribution just twice for each impingement condition, once with the plate set at α^o and once with it set at $(180 - \alpha)^o$. By reversing the distribution resulting in the latter case and superimposing it upon that of the former, it was possible, in effect, to double the number of data points in each distribution and to extend the range of closely spaced pressure taps to either side of the center. Nevertheless, the minimum spacing of data points thus achieved was still only 1/16 inch. Therefore, it must be assumed that values of the velocity gradient $[(du_e/dr)_{r=0}]_1$ determined from the local curvature of these distributions at the stagnation point are inherently less accurate than those

found in the previous study for $\alpha = 90^{\circ}$ in which at least four times as many data points were recorded. In addition, several other factors should be considered in assessing the accuracy of the present results. One of these is the vertical flow asymmetry introduced by the plate when tilted at angles of α and $180 - \alpha$. Because of interaction with the structural members below the model, the entrained flow field may have been sufficiently different in the two cases to cause a change in the stagnation point shift, thus affecting the superposition of the data. In addition, slight errors in the initial alignment for $\alpha = 90^{\circ}$ could account for a similar spurious stagnation point shift, since the model tilt axis would not pass through the normal stagnation point. A third possible error source, that of structural deflection under the highest impingement loads, is felt to have been negligible. Although each of these factors is minor in itself, their combined effect may not be negligible.

The degree of superposition achieved by plotting the raw data for α with that for $180 - \alpha$ was somewhat erratic. In some cases it was evident that the disagreement involved not only a different stagnation point displacement, but also a difference in magnitude of the stagnation pressure. Such a condition could only be confirmed for $\alpha = 90^{\circ}$ in which the local maximum of the pressure distribution was defined by each set of data independently. While this situation could also have been due in part to the combined effects already mentioned, it is more likely that a difference in the jet stagnation pressure for the two runs was to blame.

An attempt was made to apply a systematic compensating correction for at least a part of the over-all error effect just described. This was done in the case of the initial vertical misalignment. Since the runs for each impingement

ase started with a measurement of the distribution for $\alpha = 90^{\circ}$, a geometric correction based on the measured lack of symmetry for that case could be used. Although the plate was aligned vertically by nulling the pressure difference between symmetrically opposed holes before each series of runs at a particular x/d_N , the data indicate that this initial alignment may not have been maintained for subsequent 90° cases (other axial locations) in the same series. The procedure for making the correction is illustrated in Figure 5. The distance between the true jet centerline, as defined by the pressure distribution peak, and the assumed centerline, as represented by the center tap of the plate for $\alpha = 90^{\circ}$, is defined as ϵ . The locations on the plate of the shifted stagnation point are designated by δr_1 and δr_2 for oblique impingement angles α and $180 - \alpha$, respectively, while the correction to be applied to the radial coordinate for each set of data is Δ . The true centerline location is chosen such that

$$(\delta r_2 - \Delta) - (\delta r_1 - \Delta) = 0 \qquad (2)$$

where

$$\Delta = \frac{\epsilon}{\sin\alpha} \qquad (3)$$

and where the signs are as indicated in the sketch. In Figure 5(b) , this hypothetical case is shown in terms of the pressure distributions. For an actual case, a comparison is made in Figure 5(c) between the correction based upon Equation 3 and that required to bring the two sets of data into coincidence. In the case shown, the value of $\epsilon = .019$ represents an actual misalignment of .09 inch at a distance of 20 inches from the nozzle exit. The amount by which the points in Figure 5(c) miss the curve is taken to represent the cumulative effect of all other errors including the small axial displacement $\Delta\cos\alpha$ which was not mentioned earlier.

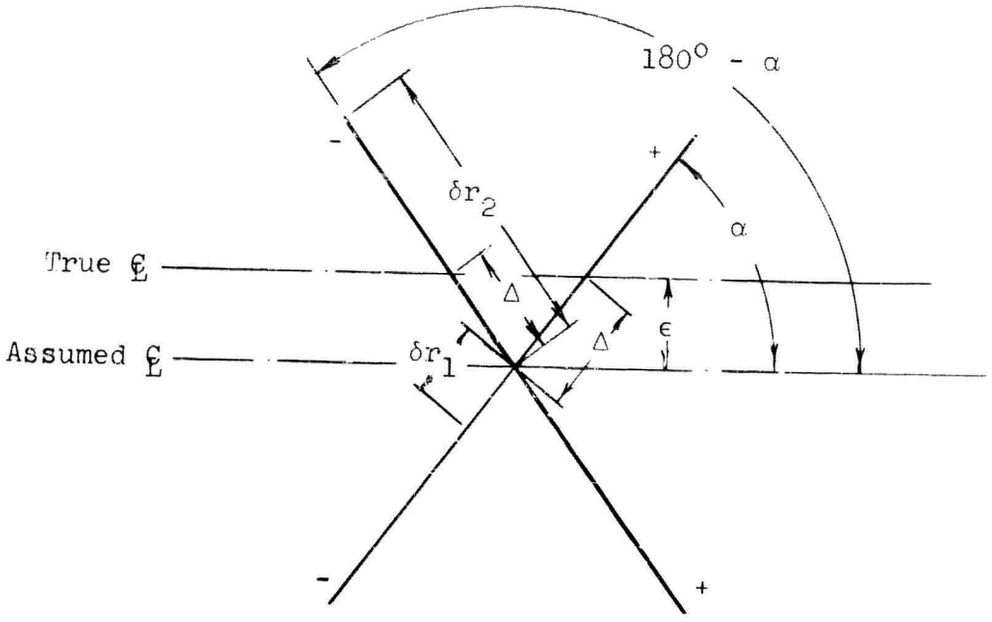

(a)

Typical example:

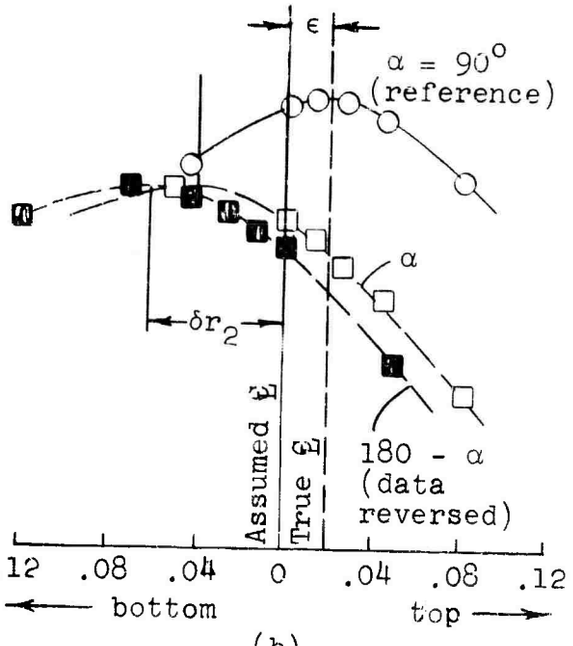

(b)

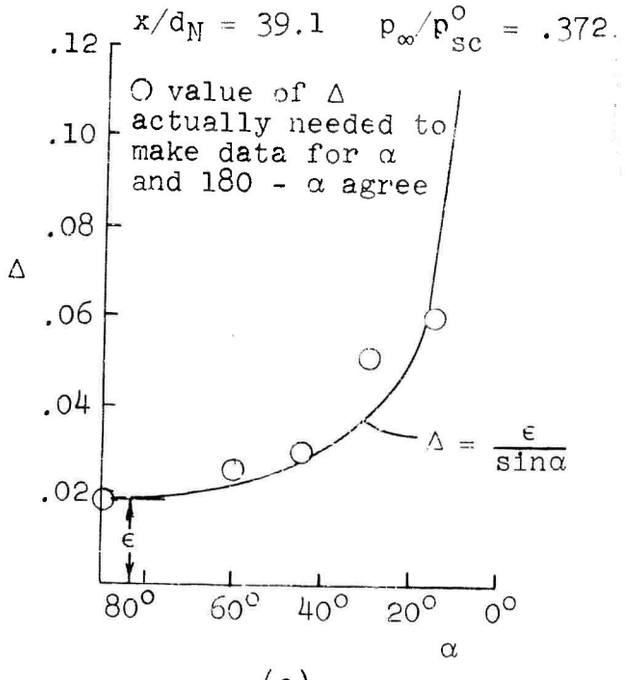

(c)

Figure 5. Illustration of procedure for correcting for error in plate alignment.

The results of the stagnation region pressure distribution measurements are presented in Figures 6 through 17. The pressures are given in the form of a coefficient referred to the stagnation point pressure for normal impingement, i.e.

$$\bar{P} = \frac{p - p_\infty}{(p_P^o)_{90} - p_\infty}$$

It is apparent that the application of the above-mentioned correction has resulted in cases of both under- and over-compensation as well as approximately correct compensation. The latter cases must be considered fortuitous, however, since the remaining error sources were undoubtedly still present. Because it was felt that the over-all success of the applied correction was thus somewhat limited, it was decided that the most meaningful distribution could be achieved by using a curve representing the average of the data for α and $180 - \alpha$. With a few exceptions, such curves were used to determine the location and magnitude of the shifted stagnation point as well as the radial velocity gradient. Data for two cases ($\alpha = 75^\circ$ and 60° for $p_\infty/p_{sc}^o = .372$ at $x/d_N = 39.1$) were eliminated because of obvious large errors in the jet stagnation pressure. The distribution curve in these instances was based on data for the remaining run of the pair, i.e. $\alpha = 105^\circ$ and 120°.

The behavior of the stagnation point for oblique impingement is shown for each jet strength in Figures 18, 19, and 20. Values of stagnation point pressure p_P^o are referred to the jet settling chamber stagnation pressure p_{sc}^o and the radial shift Δr is given as a per cent of the plate wetted radius r_w. In general, the pressure is seen to decrease and the displacement to increase when α is decreased. For $x/d_N = 1.96$, however, the stagnation

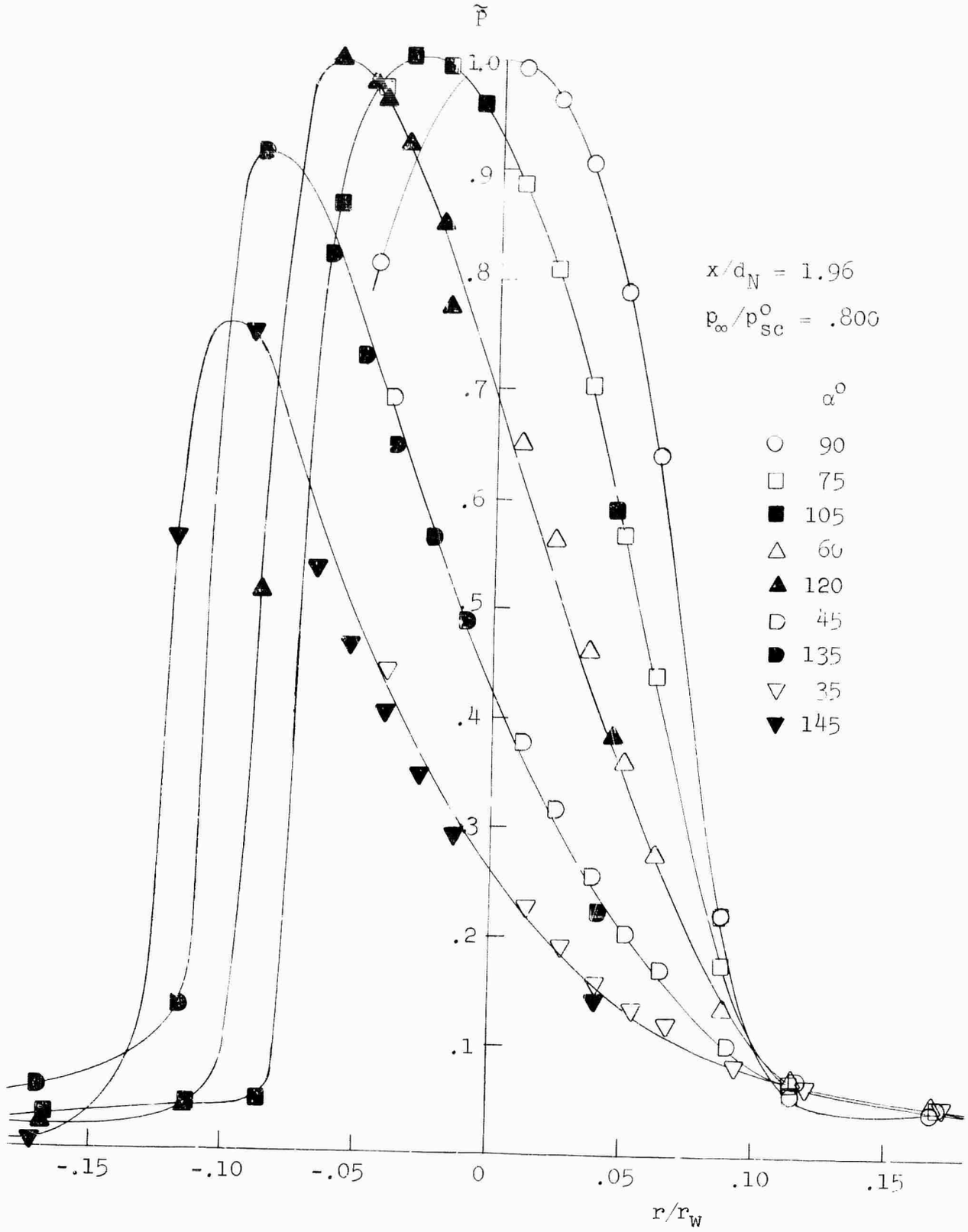

Figure 6. Pressure distribution on flat plate near the point of impingement.

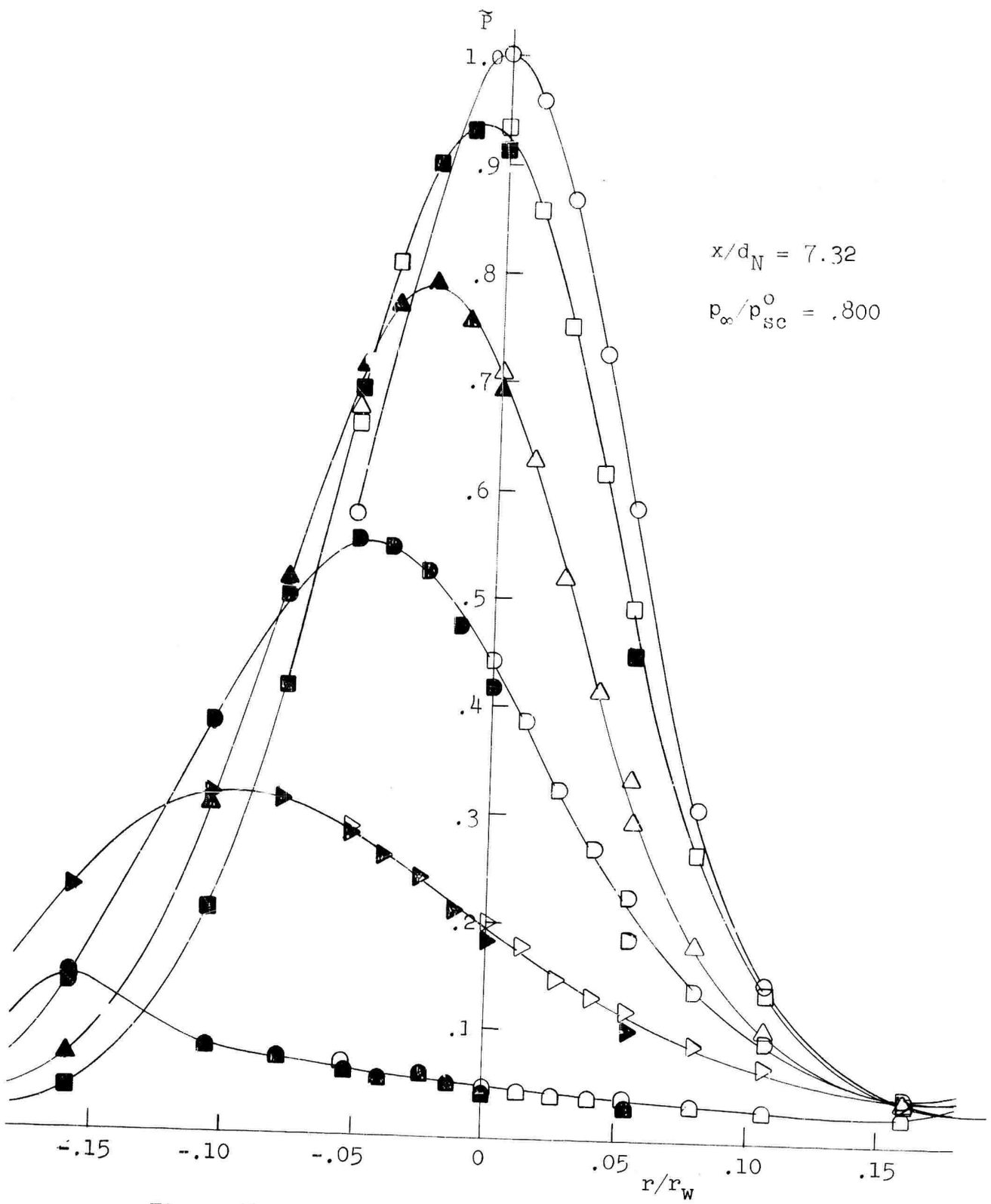

Figure 7. Pressure distribution on flat plate near the point of impingement.

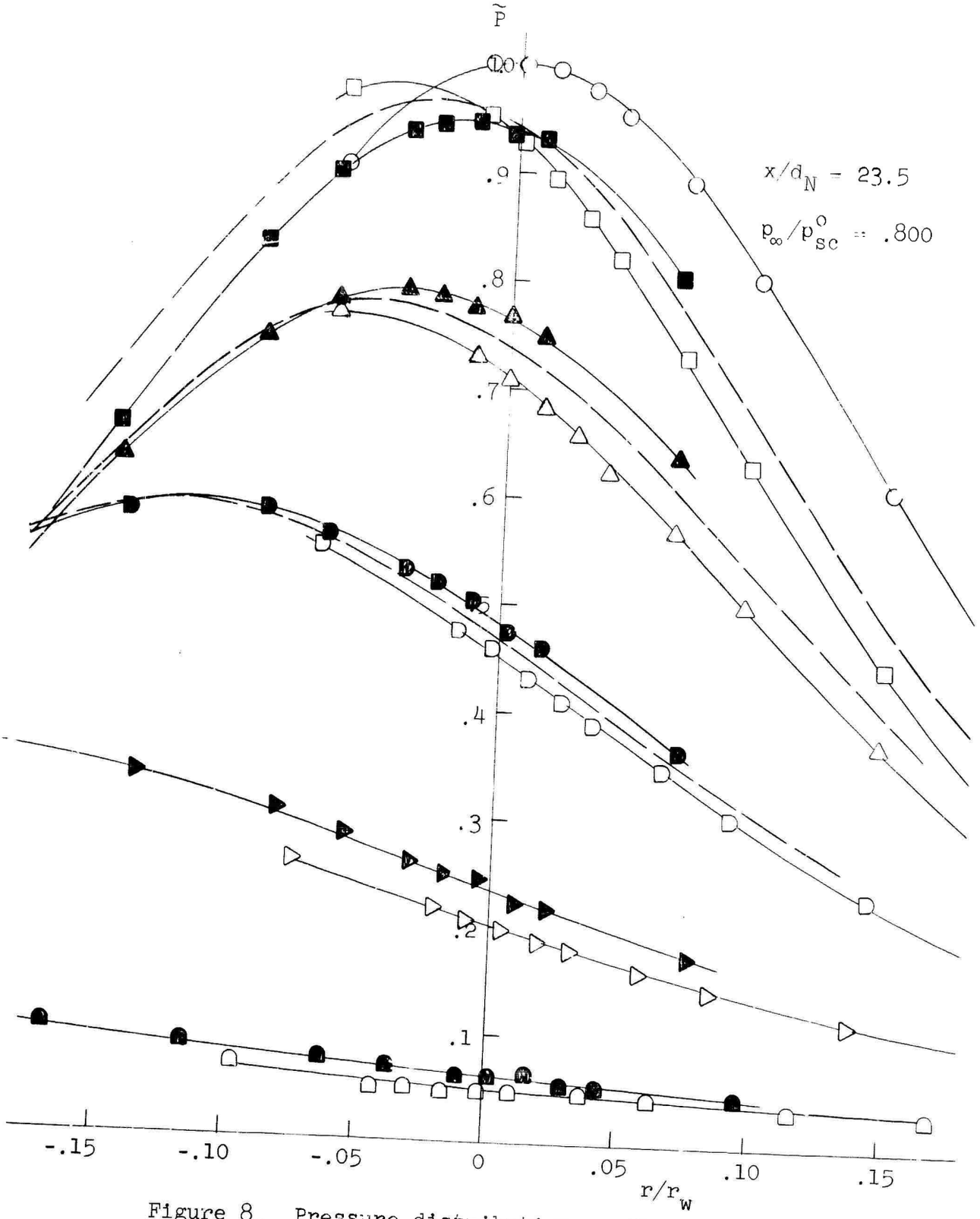

Figure 8. Pressure distribution on flat plate near the point of impingement.

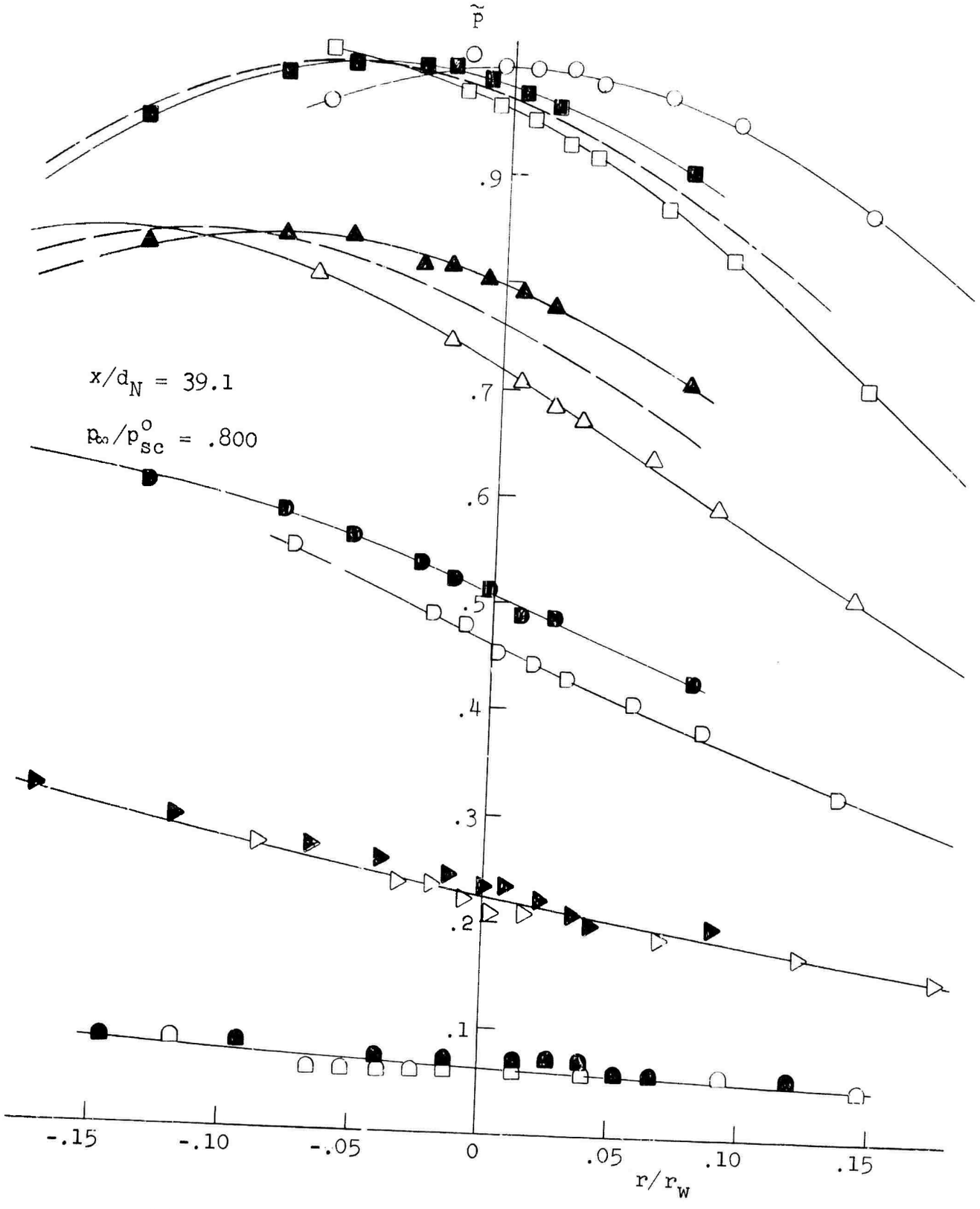

Figure 9. Pressure distribution on flat plate near the point of impingement.

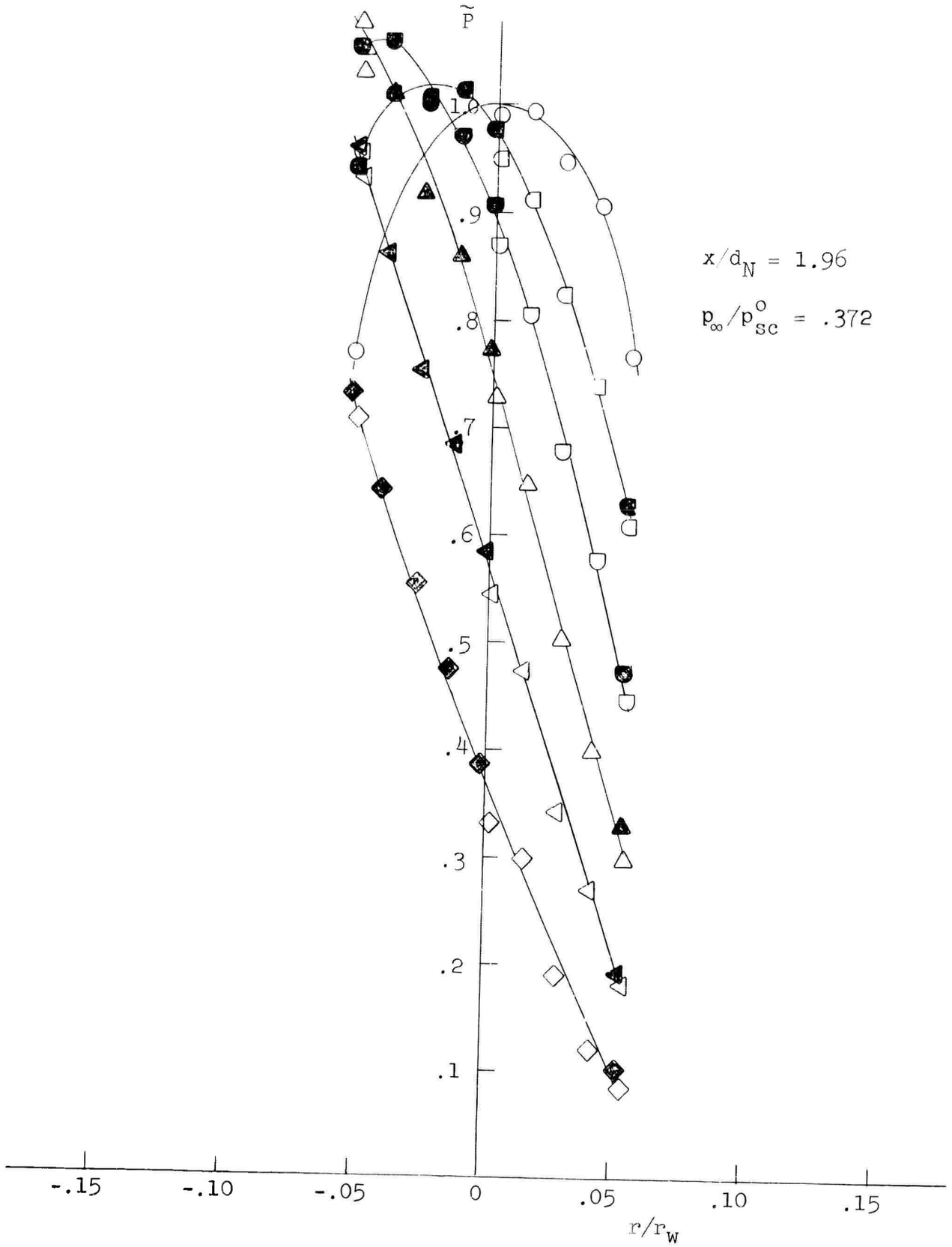

Figure 10. Pressure distribution on flat plate near the point of impingement.

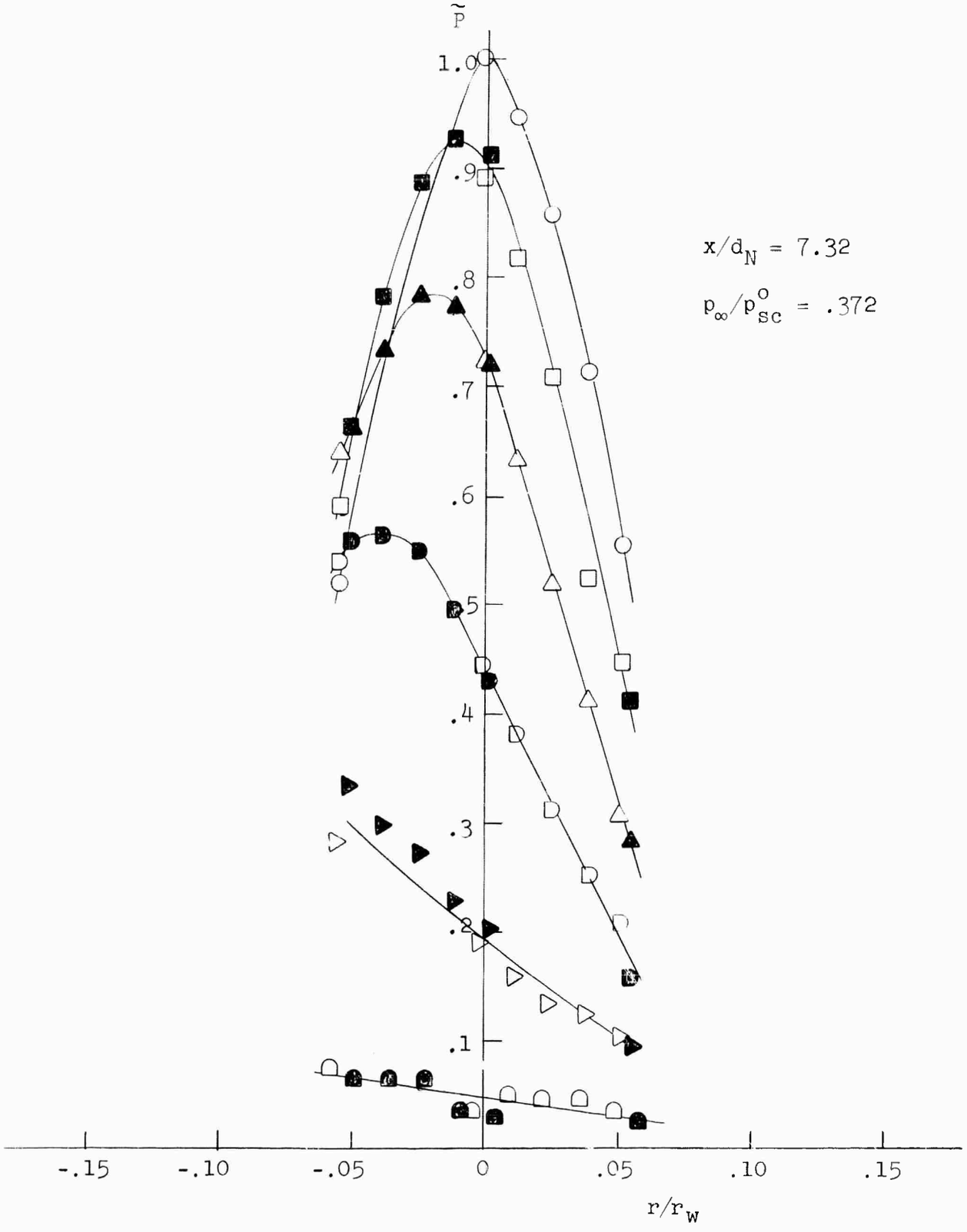

Figure 11. Pressure distribution on flat plate near the point of impingement.

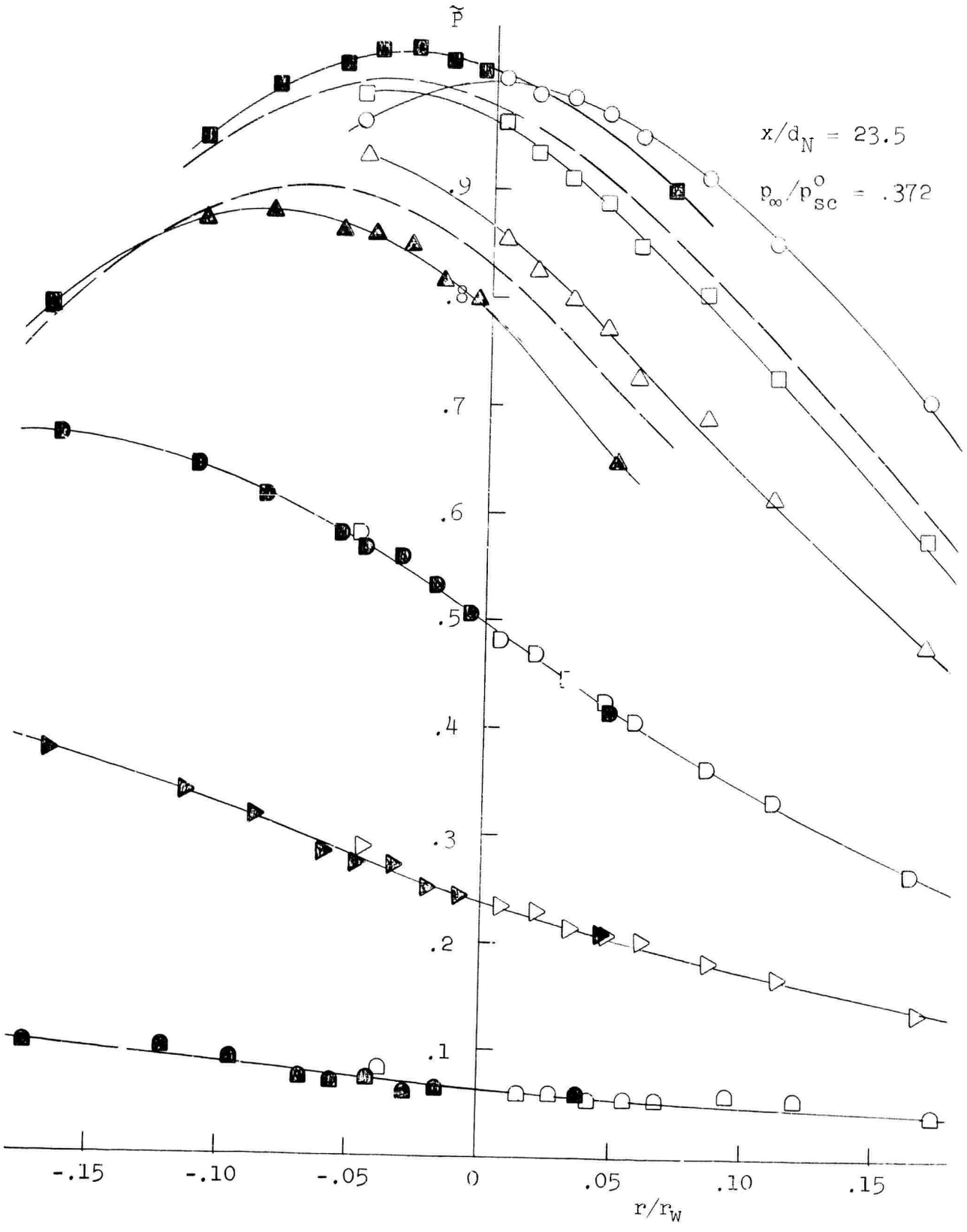

Figure 12. Pressure distribution on flat plate near the point of impingement.

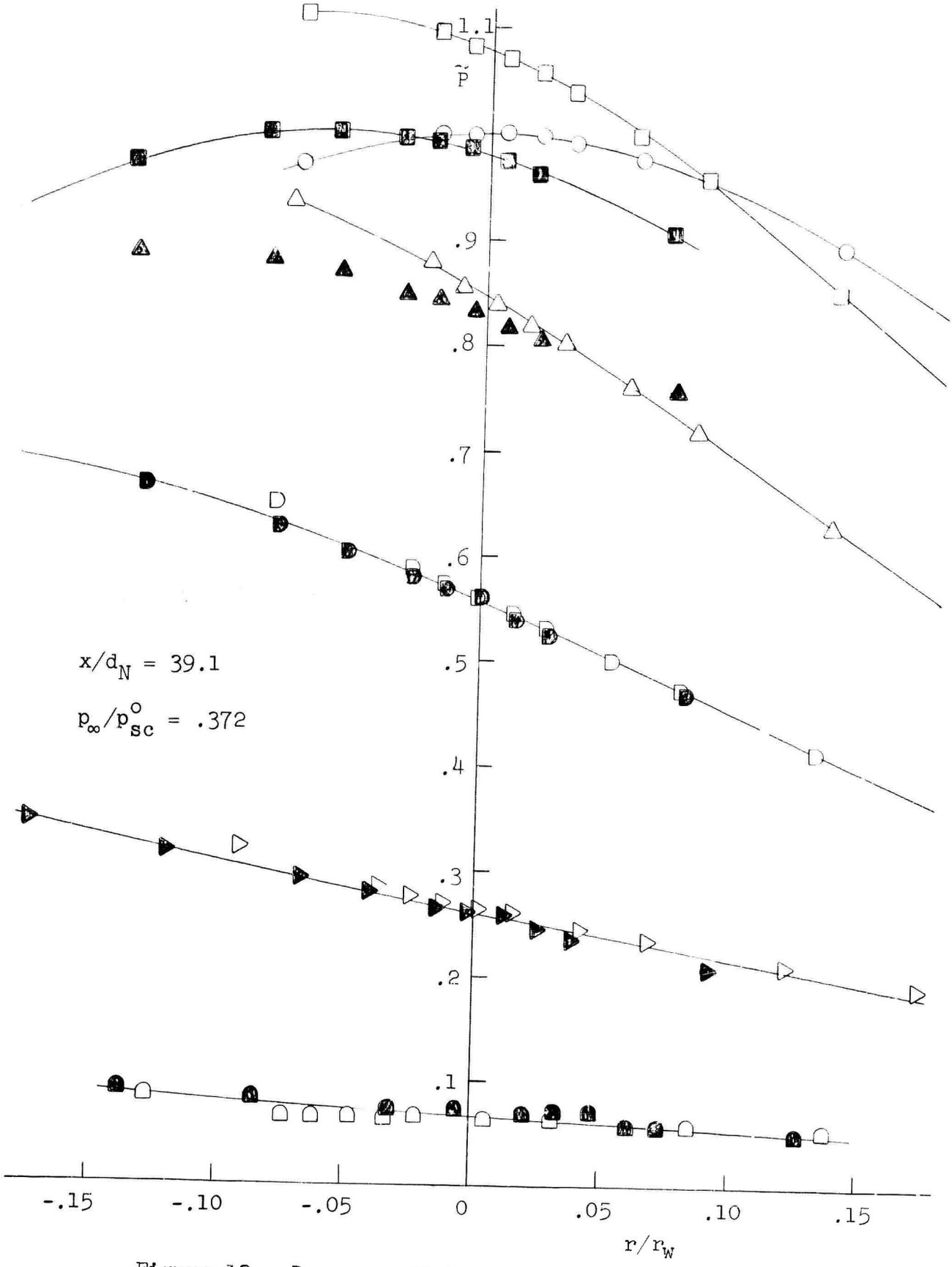

Figure 13. Pressure distribution on flat plate near the point of impingement.

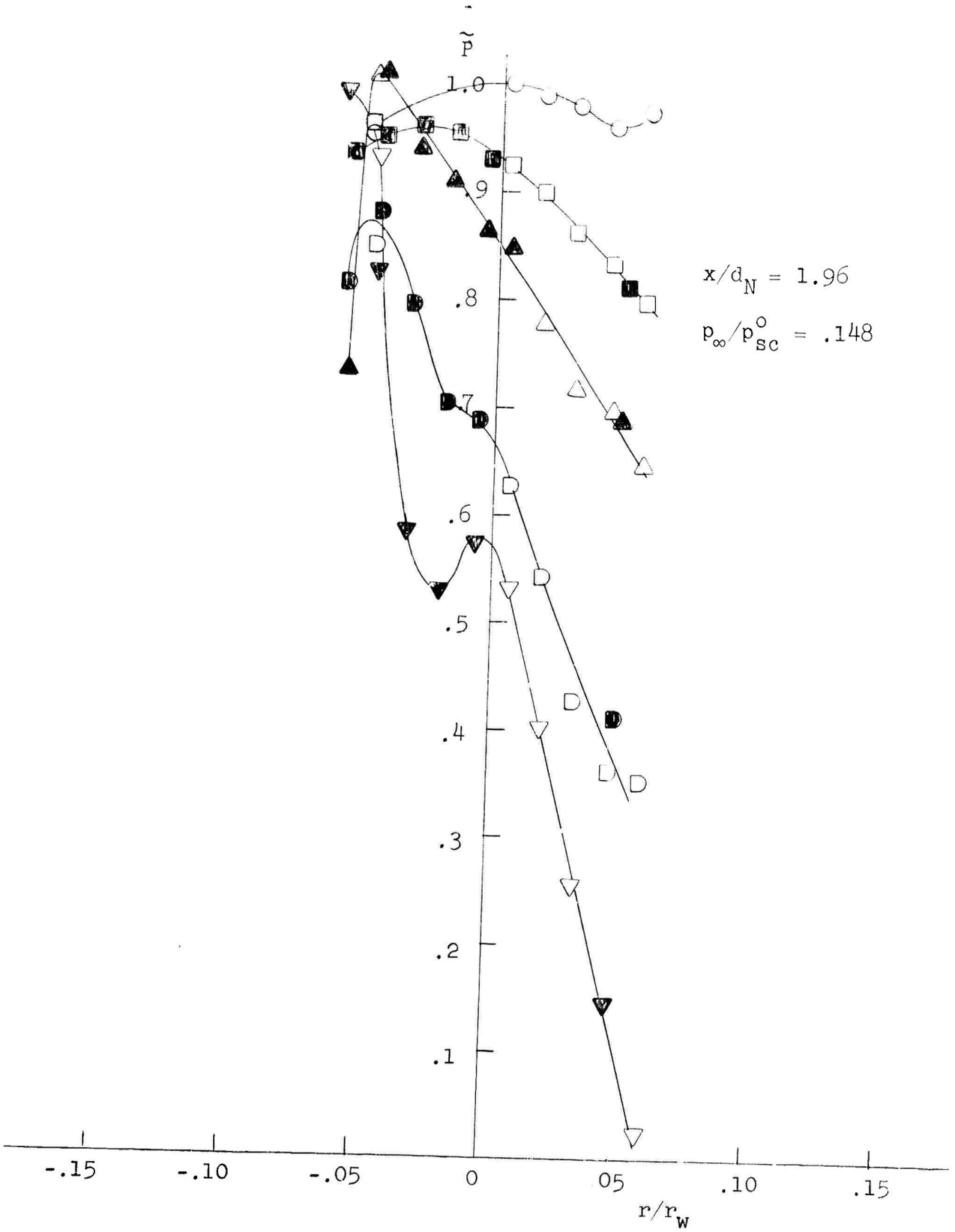

Figure 14. Pressure distribution on flat plate near the point of impingement.

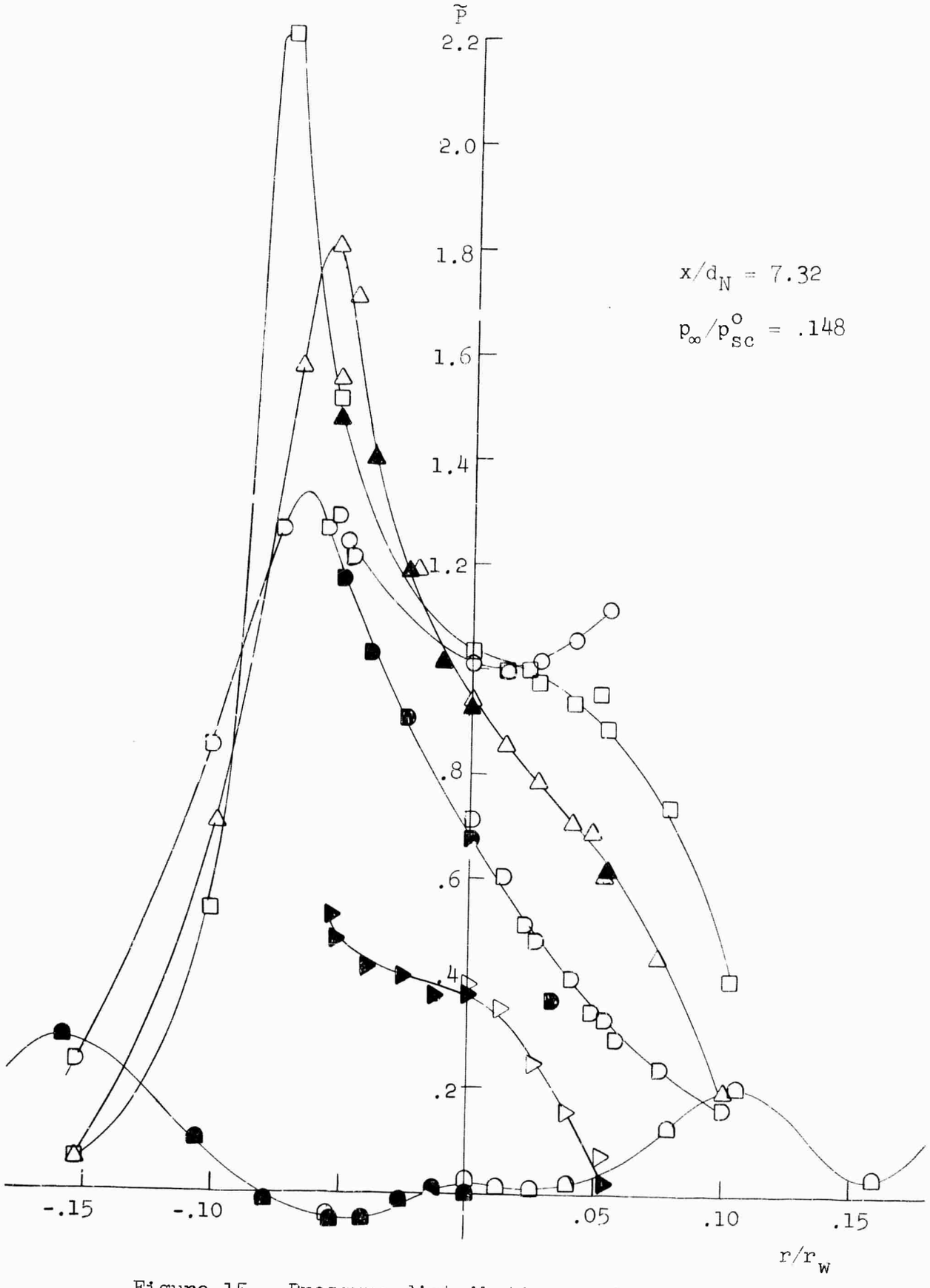

Figure 15. Pressure distribution on flat plate near the point of impingement.

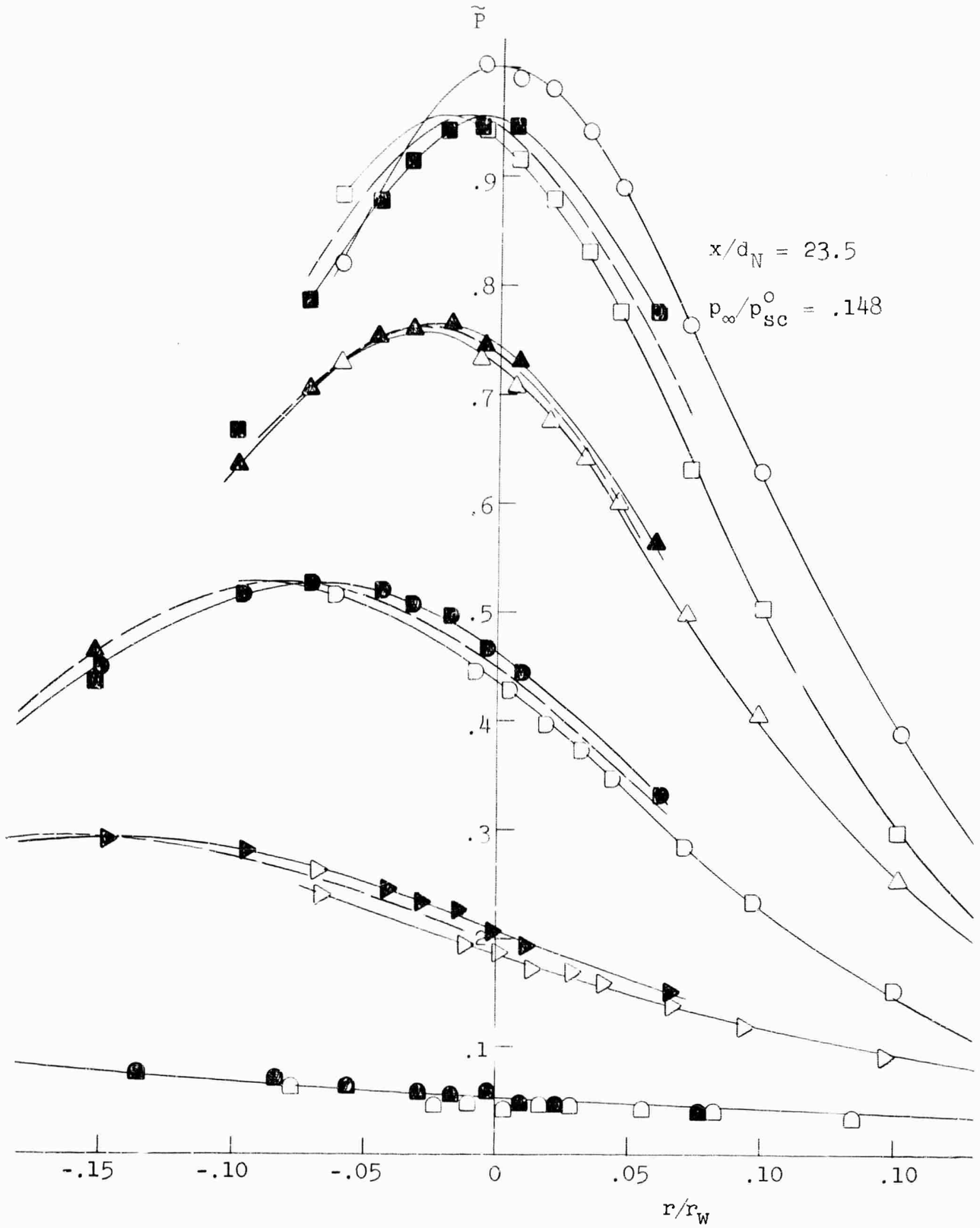

Figure 16. Pressure distribution on flat plate near the point of impingement.

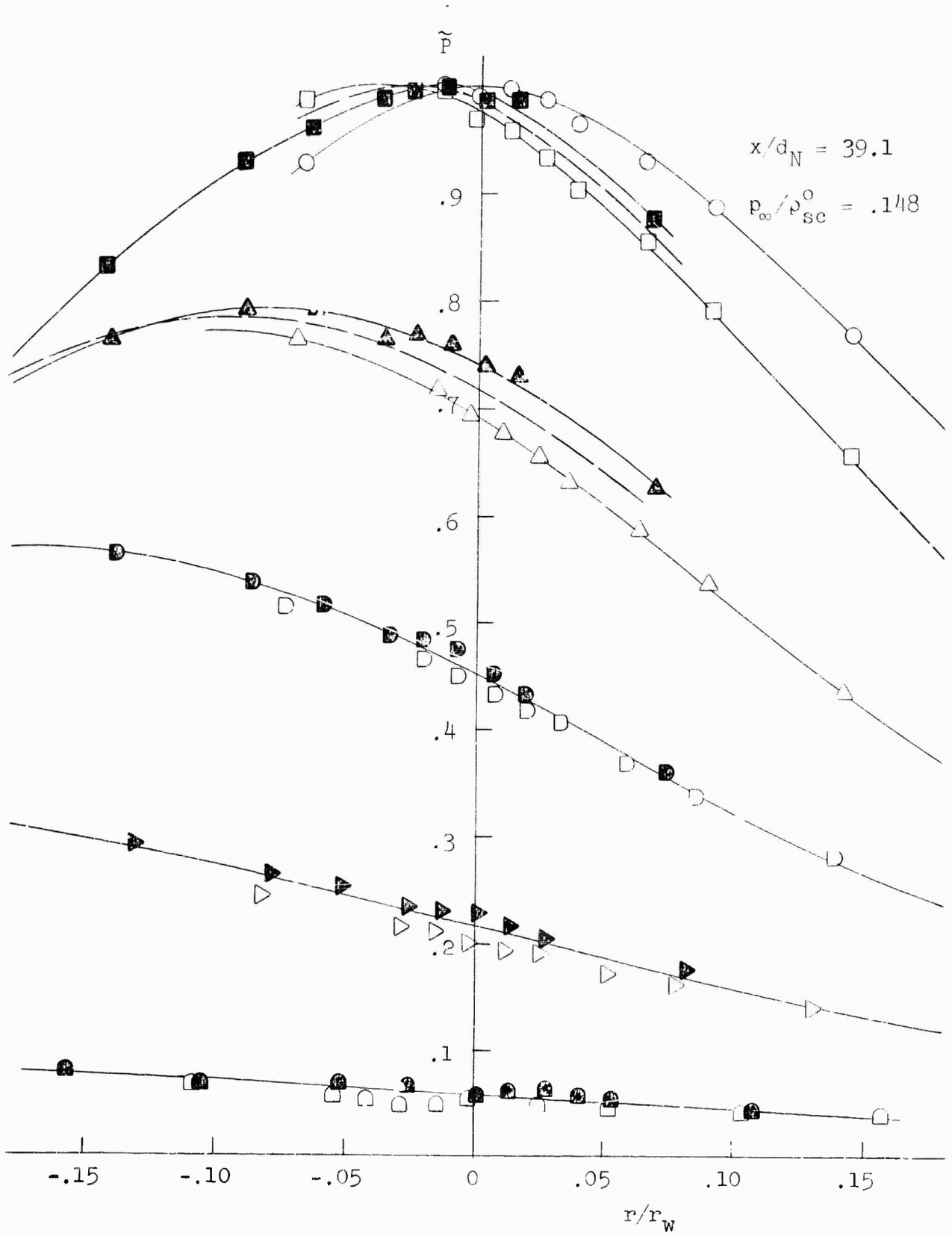

Figure 17. Pressure distribution on flat plate near the point of impingement.

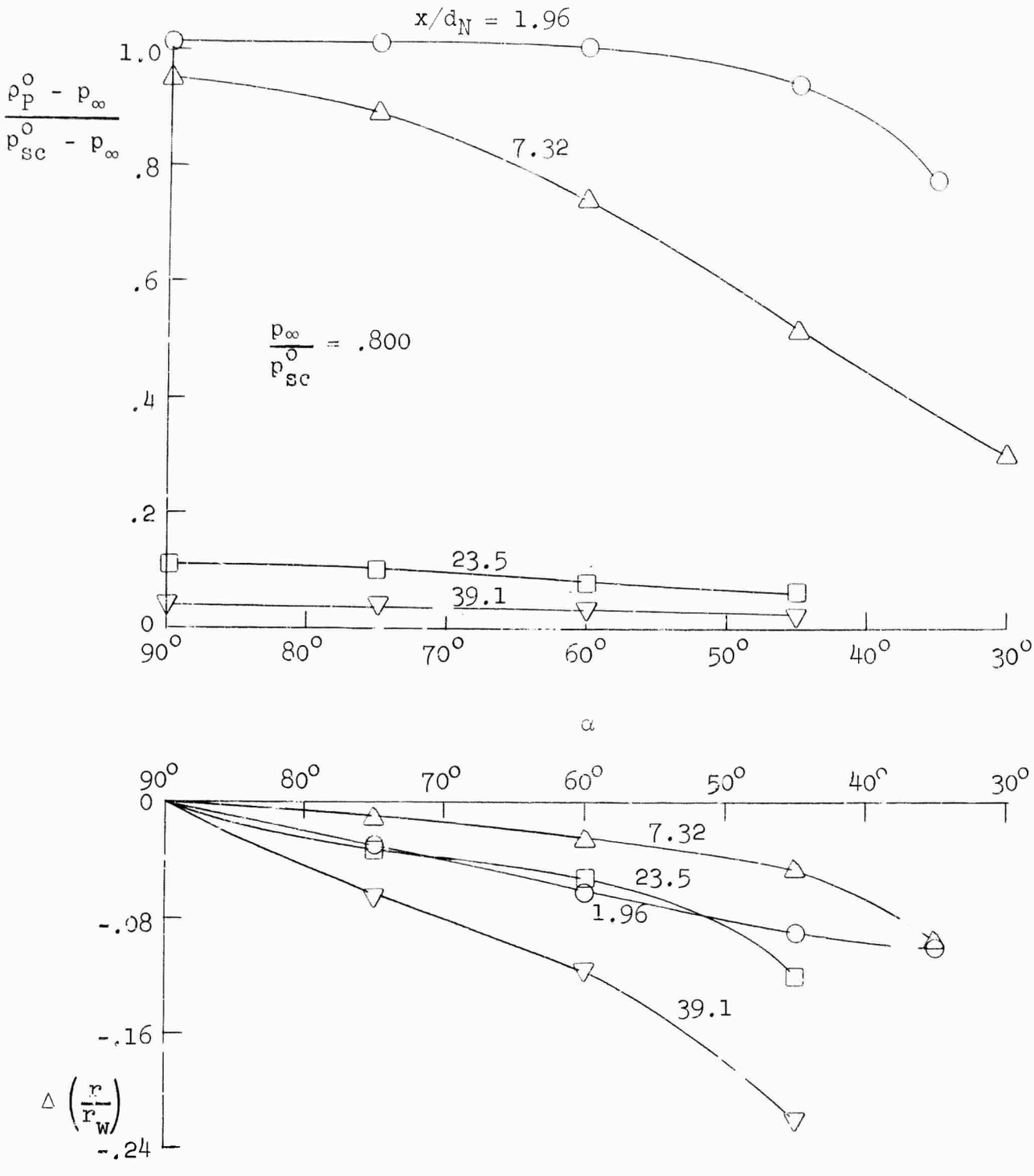

Figure 18. Dependence of stagnation point pressure level and location on angle of impingement.

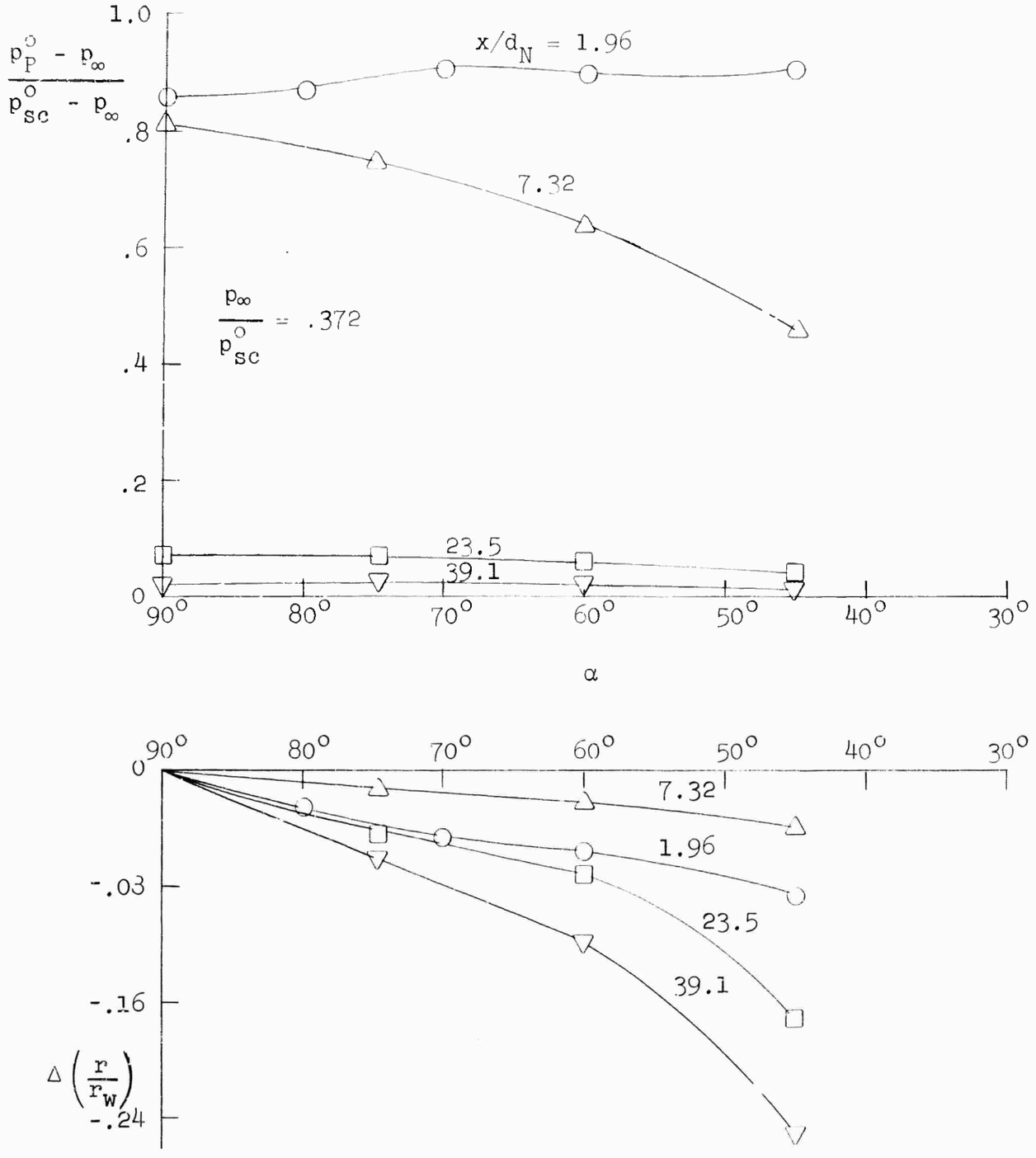

Figure 19. Dependence of stagnation point pressure level and location on angle of impingement.

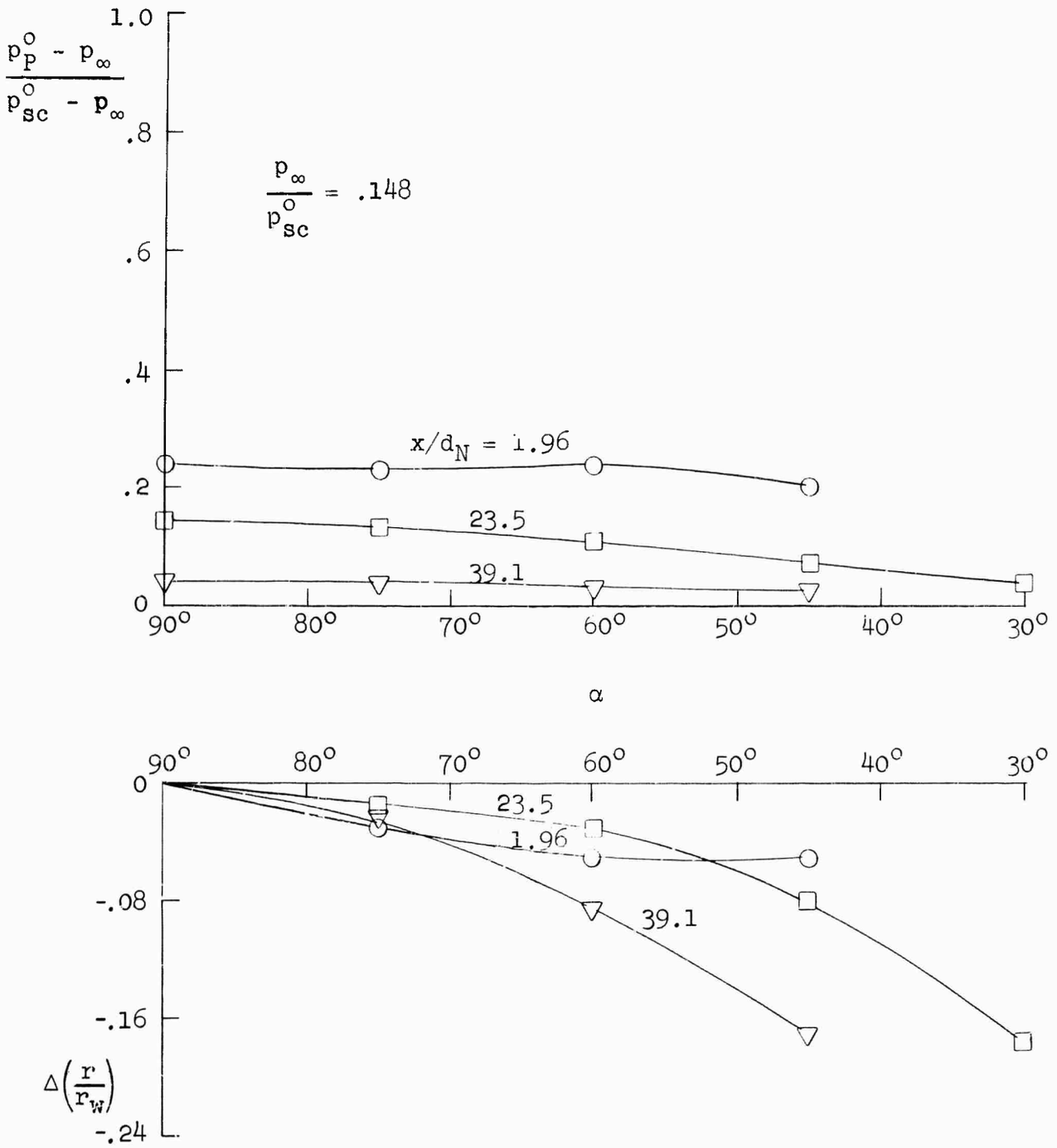

Figure 20. Dependence of stagnation point pressure level and location on angle of impingement.

pressure change is slight for a fairly wide range of angles. Some of the observed variations, of course, are to be expected for the different jet strengths because of their varied core structures.

A more general picture of the dependence on obliqueness is obtained by referring the data to properties determined for a condition of normal impingement. In Figures 21, 22, and 23, the stagnation point gauge pressure is shown as a fraction of its value for $\alpha = 90^{\circ}$. It is seen that there is a definite similarity of behavior for all cases except those for $x/d_N = 1.96$. The near independence of axial location exhibited for the three downstream cases suggests that the behavior is related to the free jet velocity profiles which are known to approach self-similarity in that region. It also appears that the insensitivity to α shown for $x/d_N = 1.96$ may be associated with the relatively flat jet velocity profiles found in the core. The exact interaction, however, in terms of streamlines and local pressure gradients is not revealed sufficiently by the results to permit a full analysis of these effects. An interesting comparison that can be made is one based on momentum considerations. Neglecting viscous effects, the force normal to the plate surface is that due to the normal component of impinging jet momentum flux, which for a given case is merely proportional to the integral over the surface of the square of the normal components of the impinging velocity profile. For a known profile shape, the force is thus proportional to $V^2\sin^2\alpha$ which, in turn, is a measure of the normal component of impinging dynamic pressure. Since the quantity $p_p^o - p_\infty$ is also a measure of this dynamic pressure, a curve of the function $\sin^2\alpha$ might be expected to show a close similarity with the measured values of $p_p^o - p_\infty$ (Figures 21, 22, and 23).

For the purpose of determining actual stagnation point pressure levels based on the data of Figures 21, 22, and 23,

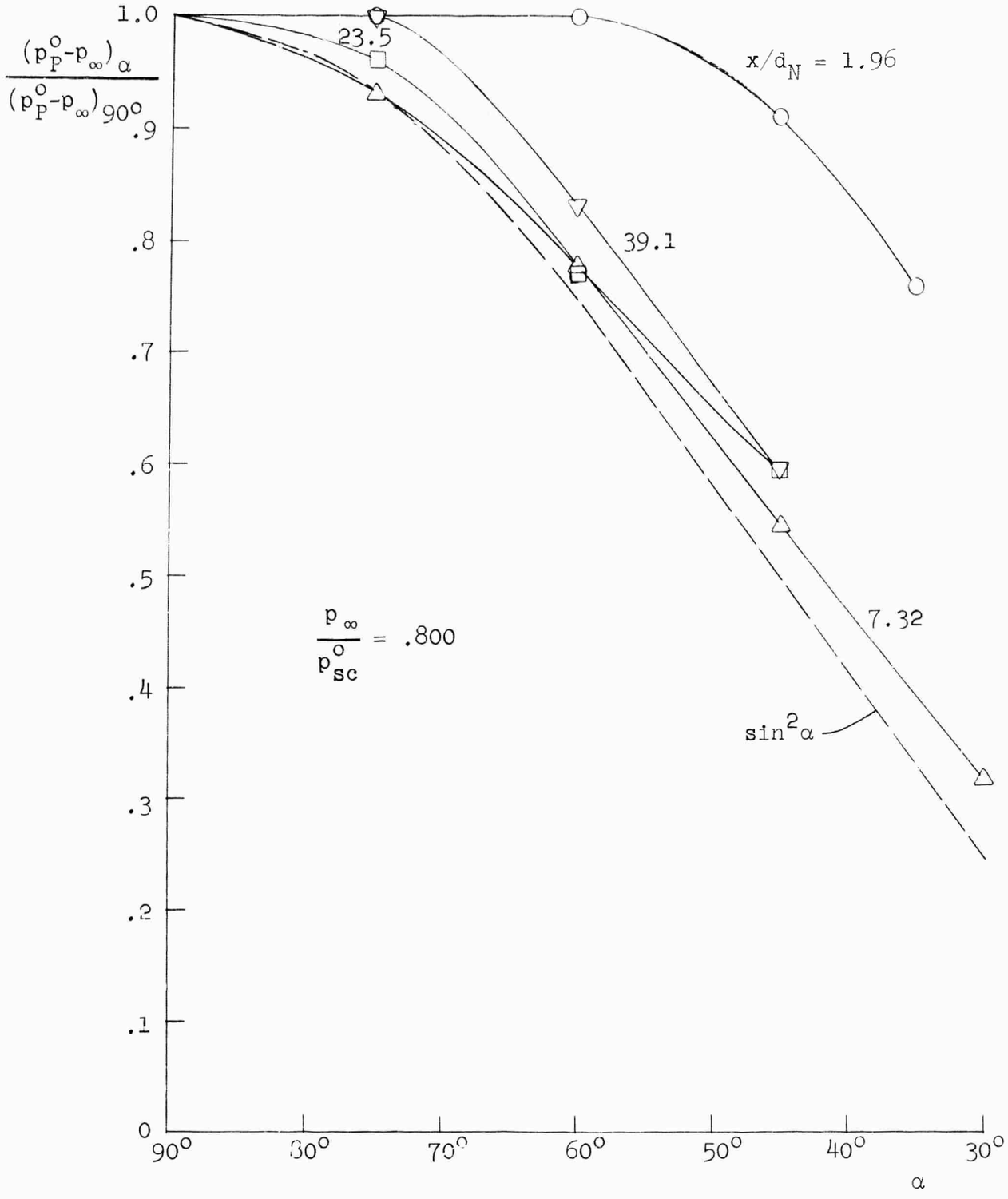

Figure 21. Dependence of nondimensional stagnation point pressure on angle of impingement.

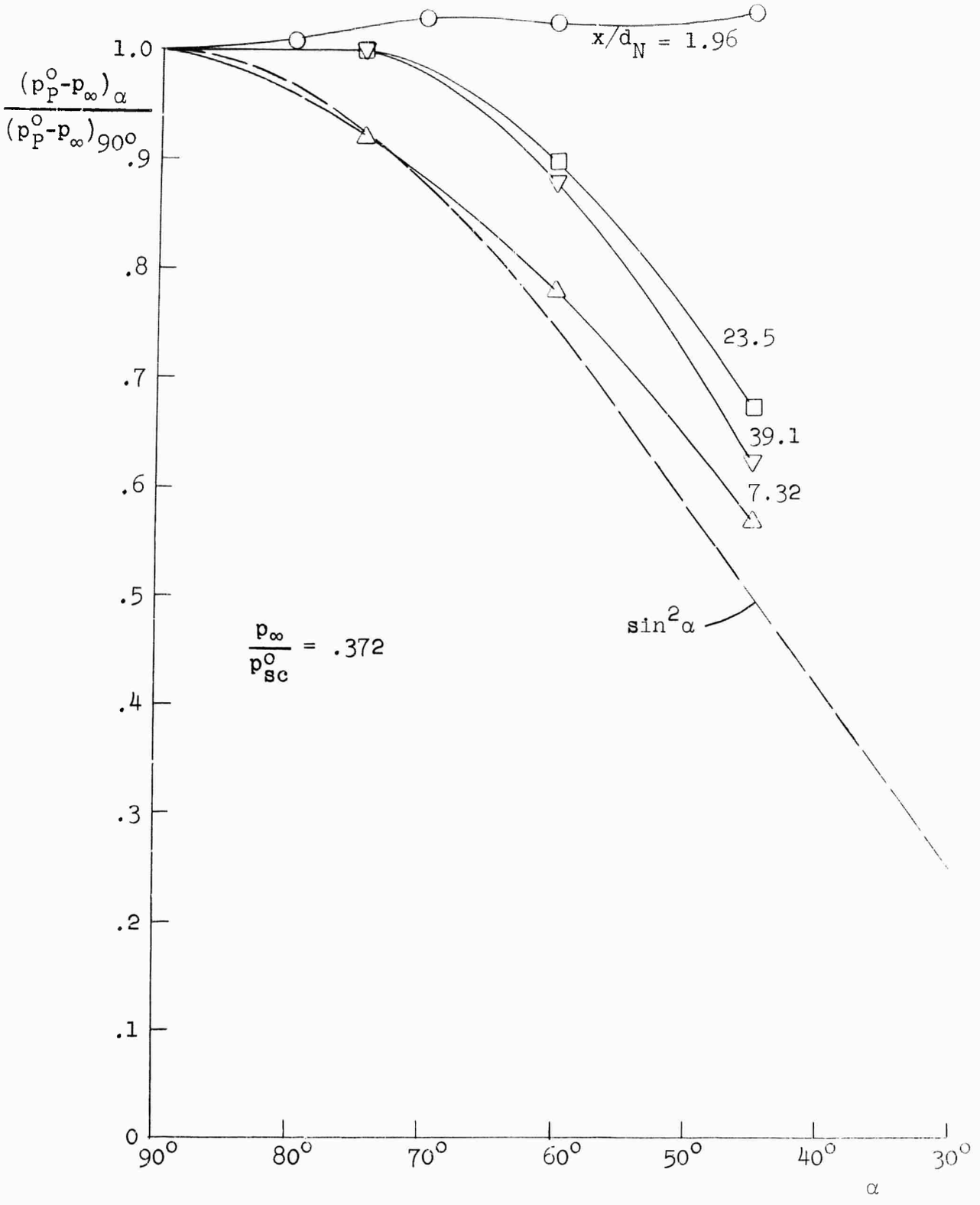

Figure 22. Dependence of nondimensional stagnation point pressure on angle of impingement.

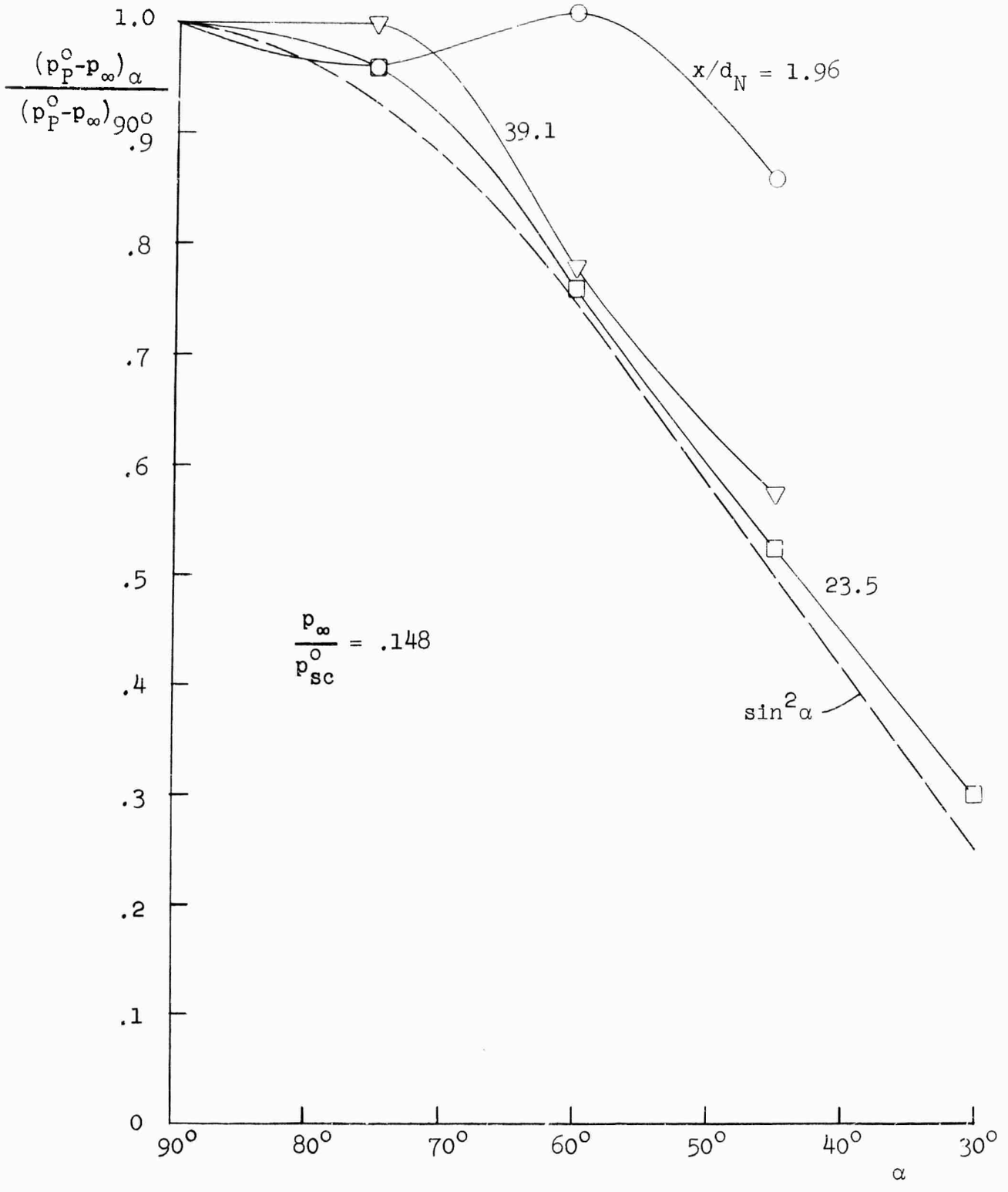

Figure 23. Dependence of nondimensional stagnation point pressure on angle of impingement.

the measured axial decay behavior for normal impingement is presented in Figure 24. The details of the decay curves shown were obtained in a fine-scale axial traverse of the flat plate with an incremental distance of .1 inch between runs. The numerous data points are omitted. The points that are shown are those resulting from the repeat measurement for $\alpha = 90^{\circ}$ made during the oblique impingement runs. The repeatability of such measurements is thought to be quite satisfactory.

The displacement Δr of the stagnation point can also be referred to a normalizing parameter, in this case, the measured free jet half-velocity radius $r_{.5}$ at the same axial station. Plots of $\Delta r/r_{.5}$ vs. α are given in Figures 25, 26, and 27. It is seen that except for the close impingement case $(x/d_N = 1.96)$ there is a tendency for this nondimensional displacement to be independent of axial distance. Once again, a relationship between the observed behavior and the local character of the free jet velocity profile is suggested, with the distance-independent cases confined to regions where the profiles are of similar shape. In contrast to the relative insensitivity to α shown by the stagnation pressure for $x/d_N = 1.96$, the displacement Δr for this case shows the most sensitivity of all to α.

2.3.2. Photographic studies. A series of schlieren photographs was taken using a spark light source of ~1μsec duration and a standard off-axis parallel beam optical system. Several of these pictures of the underexpanded jets are shown in Figures 28 and 29 for $x/d_N = 1.96$ and 7.32, respectively. In Figure 28, which shows

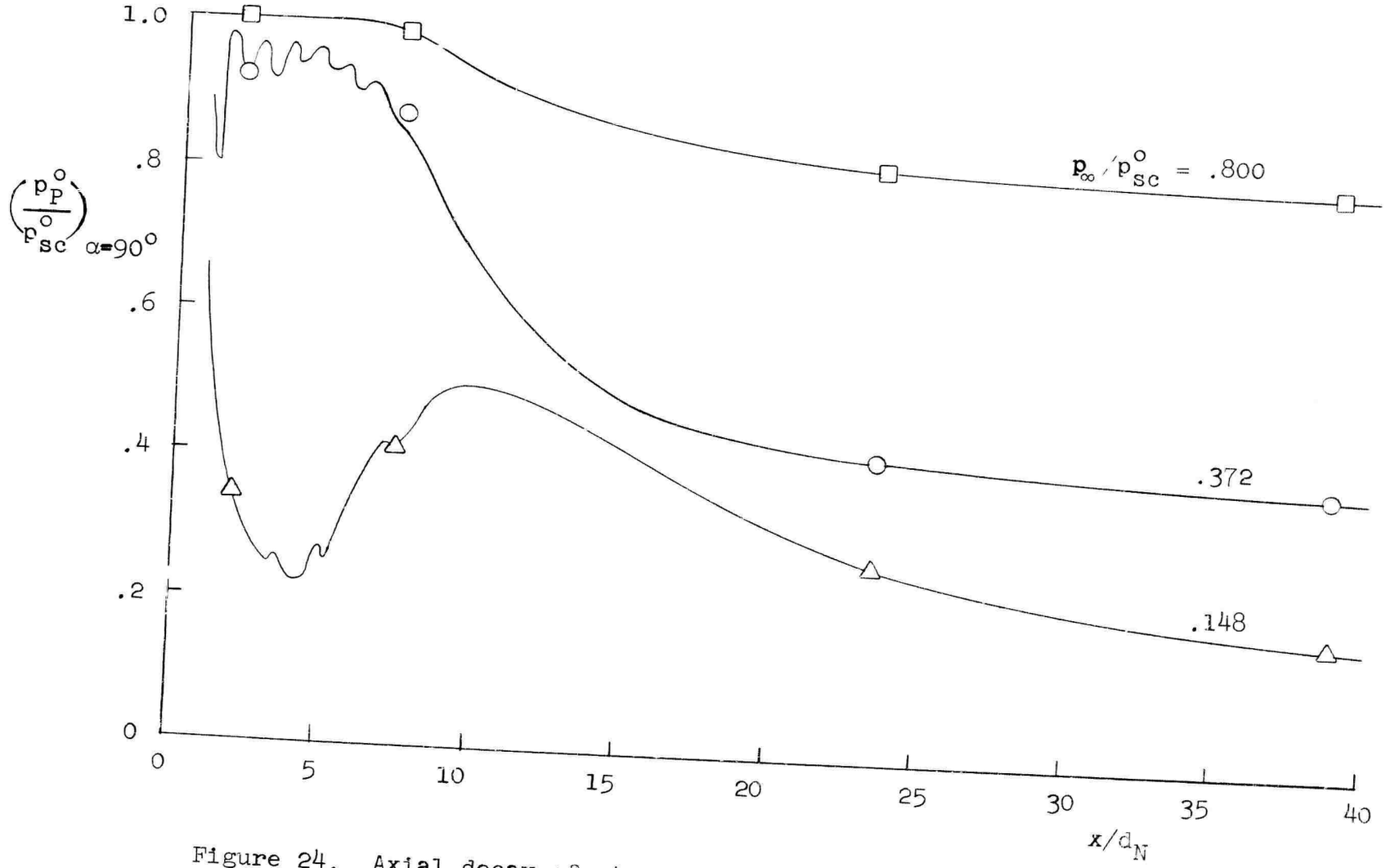

Figure 24. Axial decay of stagnation point pressure for normal impingement.

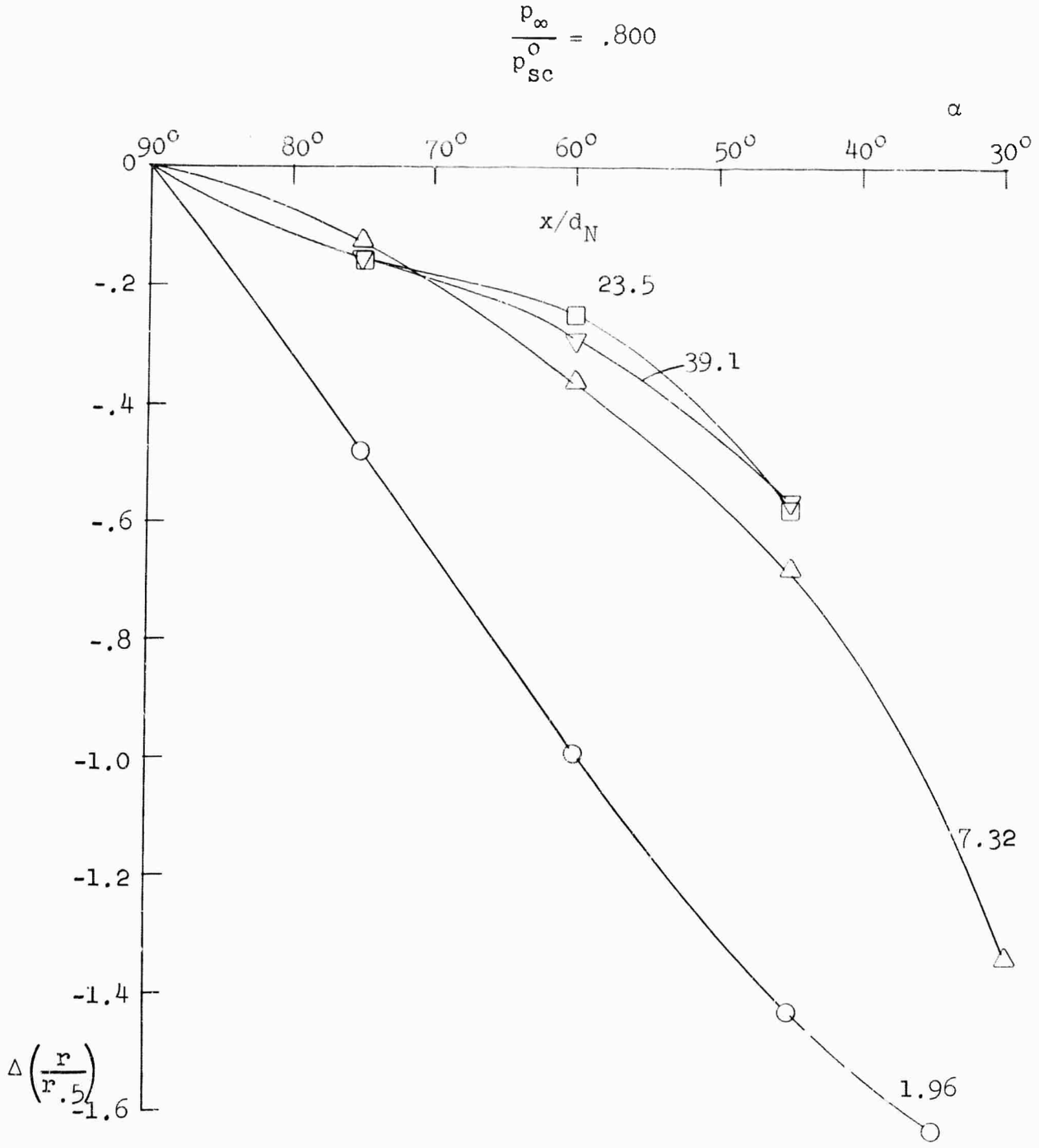

Figure 25. Dependence of nondimensional displacement of stagnation point on angle of impingement.

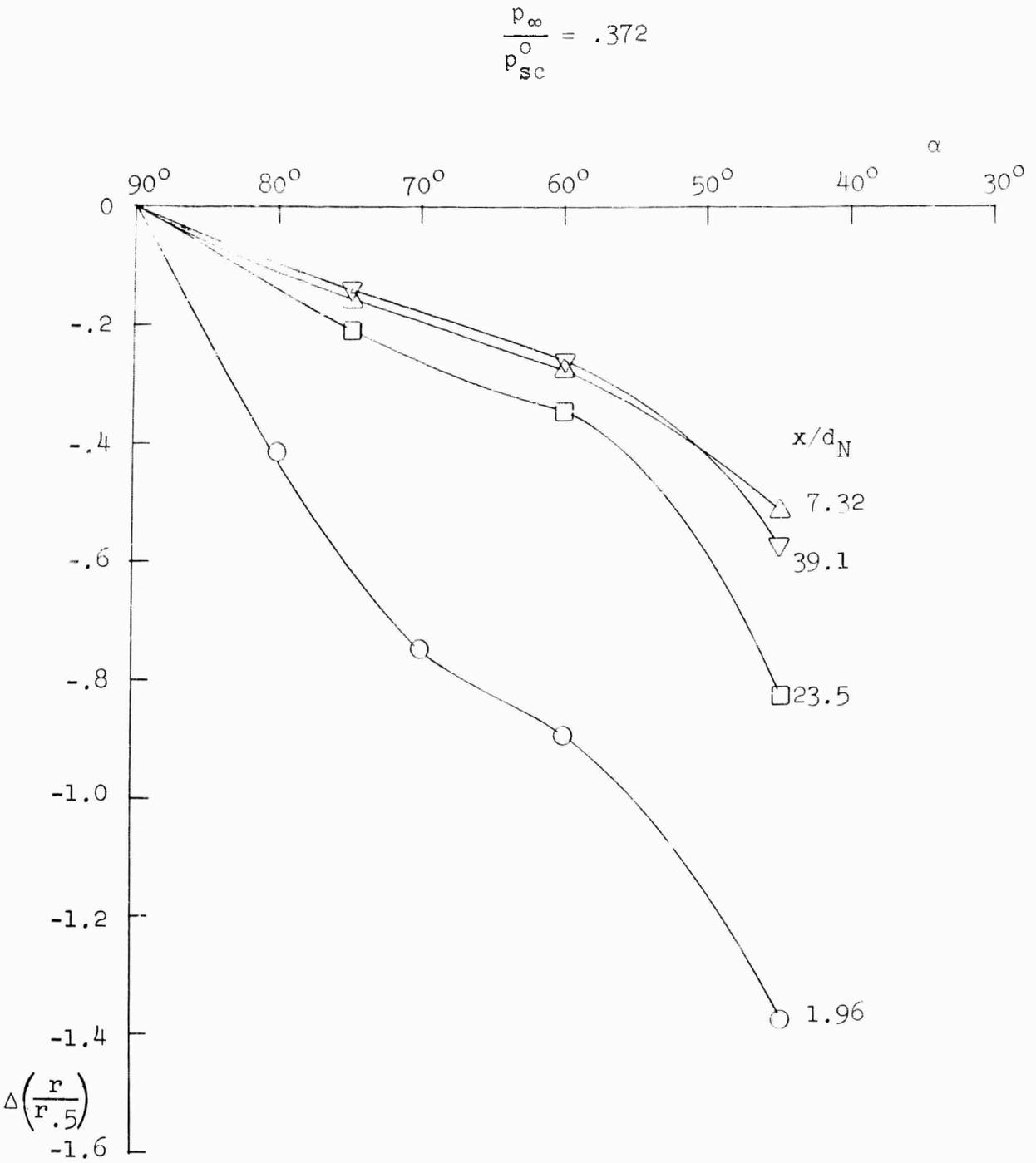

Figure 26. Dependence of nondimensional displacement of stagnation point on angle of impingement.

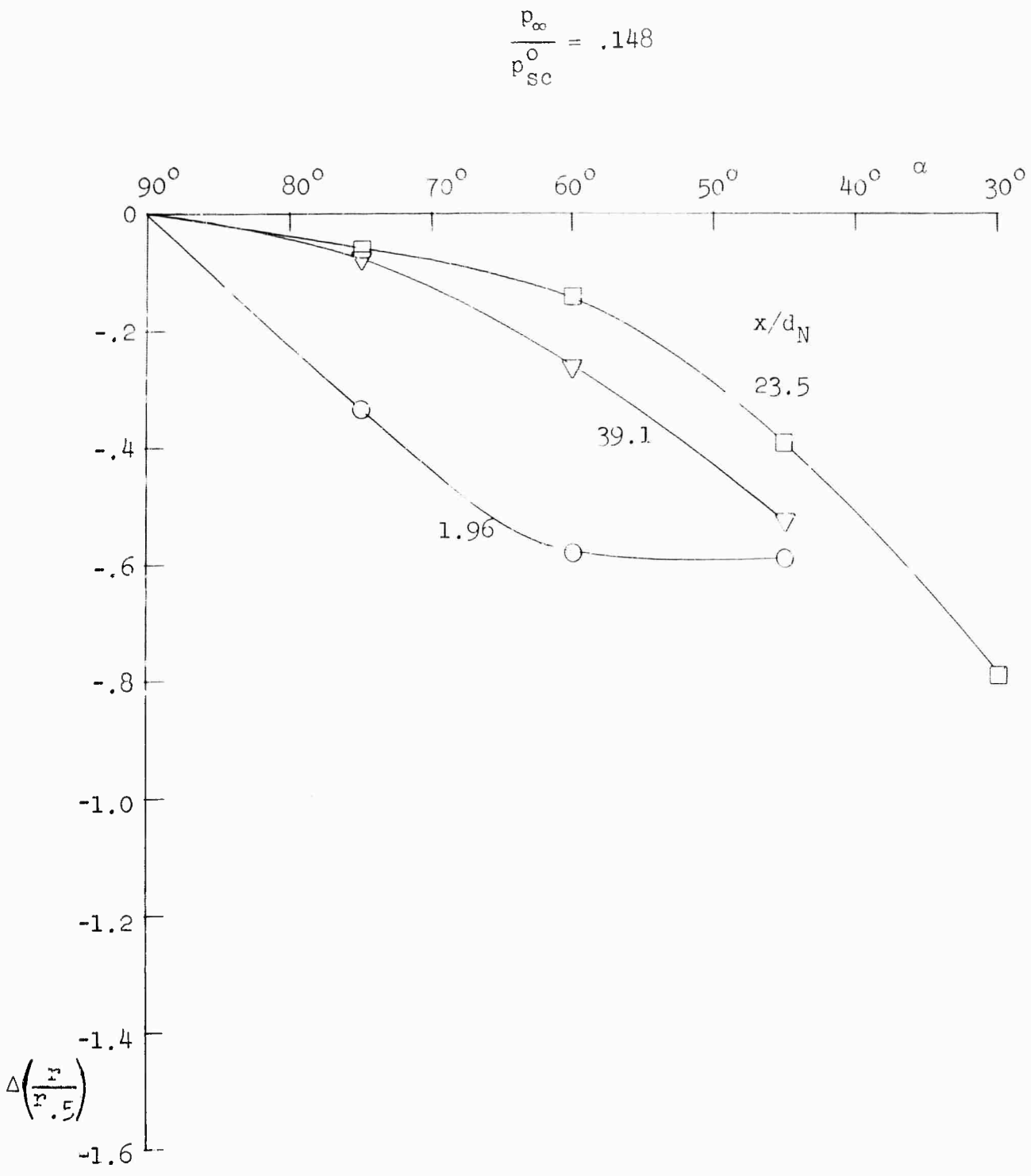

Figure 27. Dependence of nondimensional displacement of stagnation point on angle of impingement.

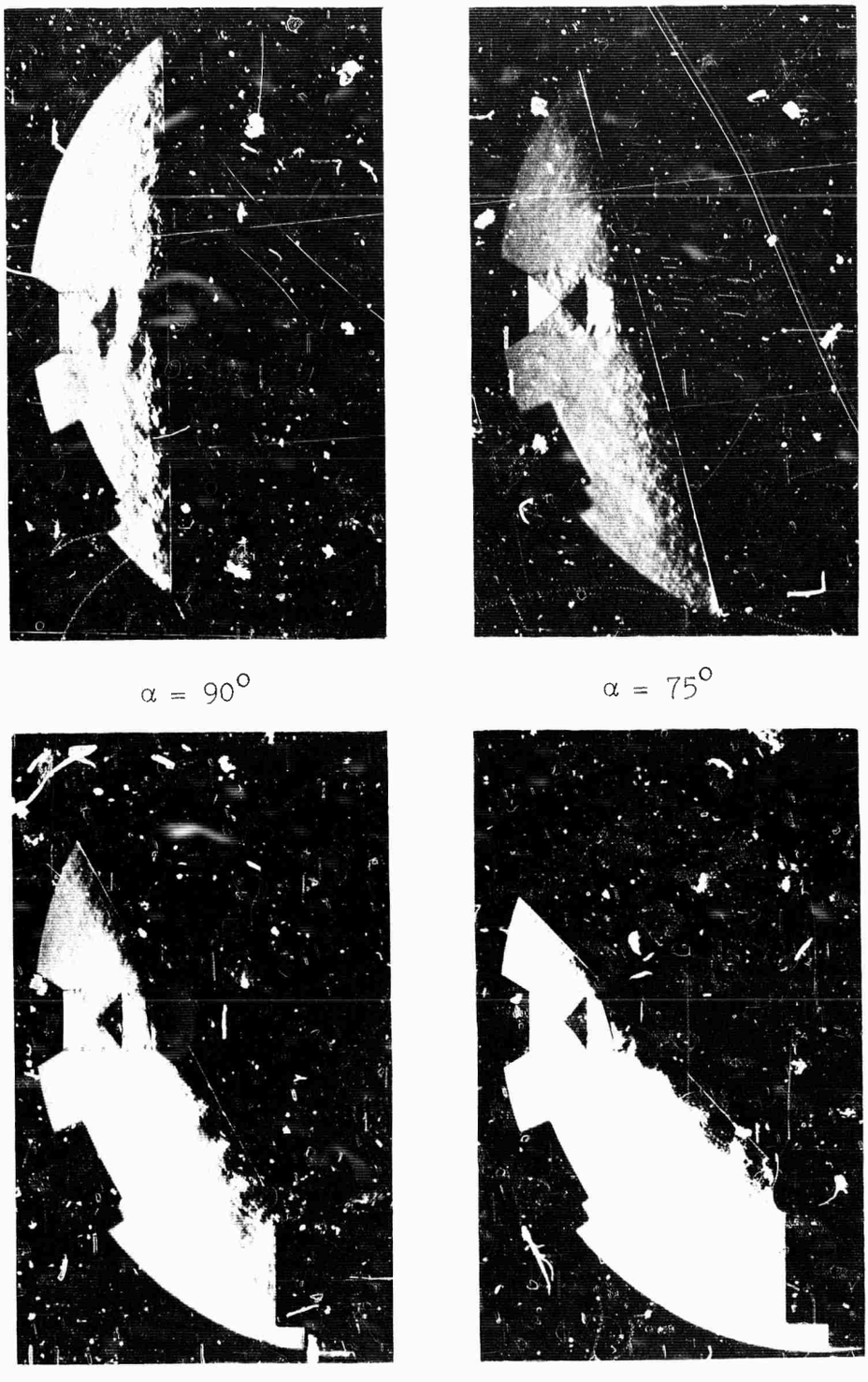

$\alpha = 90^{\circ}$ $\alpha = 75^{\circ}$

$\alpha = 60^{\circ}$ $\alpha = 45^{\circ}$

Figure 28. Schlieren photographs of underexpanded jet impinging on flat plate. $p_{\infty}/p^{\circ}_{sc} = .372$, $x/d_N = 1.96$.

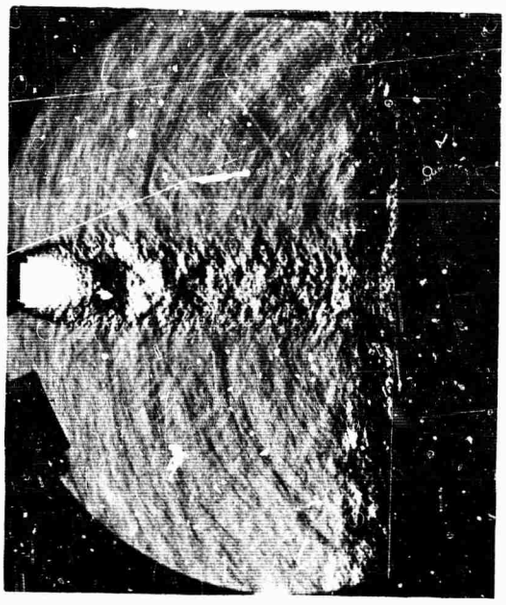

$\alpha = 90^{\circ}$

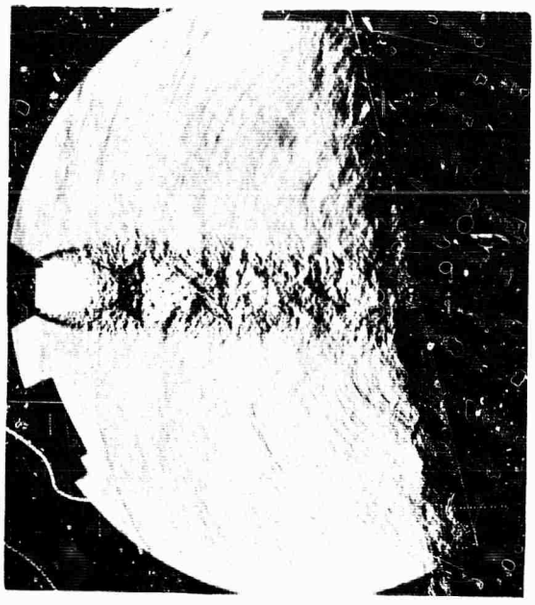

$\alpha = 75^{\circ}$

$\alpha = 60^{\circ}$

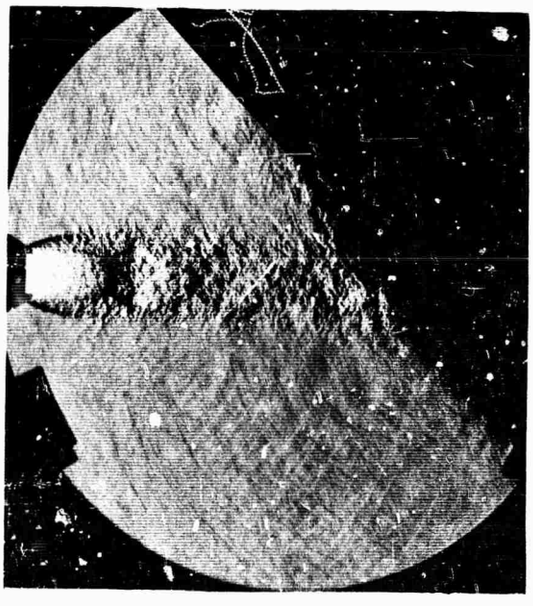

$\alpha = 45^{\circ}$

Figure 29. Schlieren photographs of underexpanded jet impinging on flat plate. $p_{\infty}/p^{0}_{sc} = .148$, $x/d_{N} = 7.32$.

the close impingement of the moderately underexpanded jet, it is of interest to note that at least a portion of the wall jet flow appears to contain a shock structure for $\alpha = 60^{\circ}$ and 45°. The impingement of the highly underexpanded jet is shown in Figure 29.

2.4. Evaluation of the Velocity Gradient $[(du_e/dr)_{r=0}]_1$.

The stagnation region pressure distributions were used to compute the value of the radial velocity gradient $[(du_e/dr)_{r=0}]_1$ for each condition. An equation relating this quantity to the curvature of the pressure distribution has already been discussed (Equation 1). In order to apply this equation, the data were first plotted in the form p/p_p^o vs. $(r/r_w)^2$. Actually, because of the relative lack of detail available in these data, the evaluation was performed on the basis of the faired curve drawn as described in 2.3.1. Values of $[(du_e/dr)_{r=0}]_1$ were determined directly from the slope of the p/p_p^o vs. $(r/r_w)^2$ durve at $r = 0$. Figures 30, 31, and 32 show the values so determined for each jet strength and axial location as functions of impingement angle. Also plotted along the $\alpha = 90^{\circ}$ axis are the values found during the more detailed normal impingement experiments for which the data had higher resolution (solid symbols). For consistency, the curves are drawn with respect to the present $\alpha = 90^{\circ}$ data taken as a part of the oblique impingement survey. Certain similarities of behavior for the three jet strengths can be noted. As was observed for the stagnation point location and pressure, there is a substantial difference between impingement of the core and fully developed regions. With $x/d_N = 1.96$, a sharp increase begins near $\alpha = 75^{\circ}$ after relatively little change between

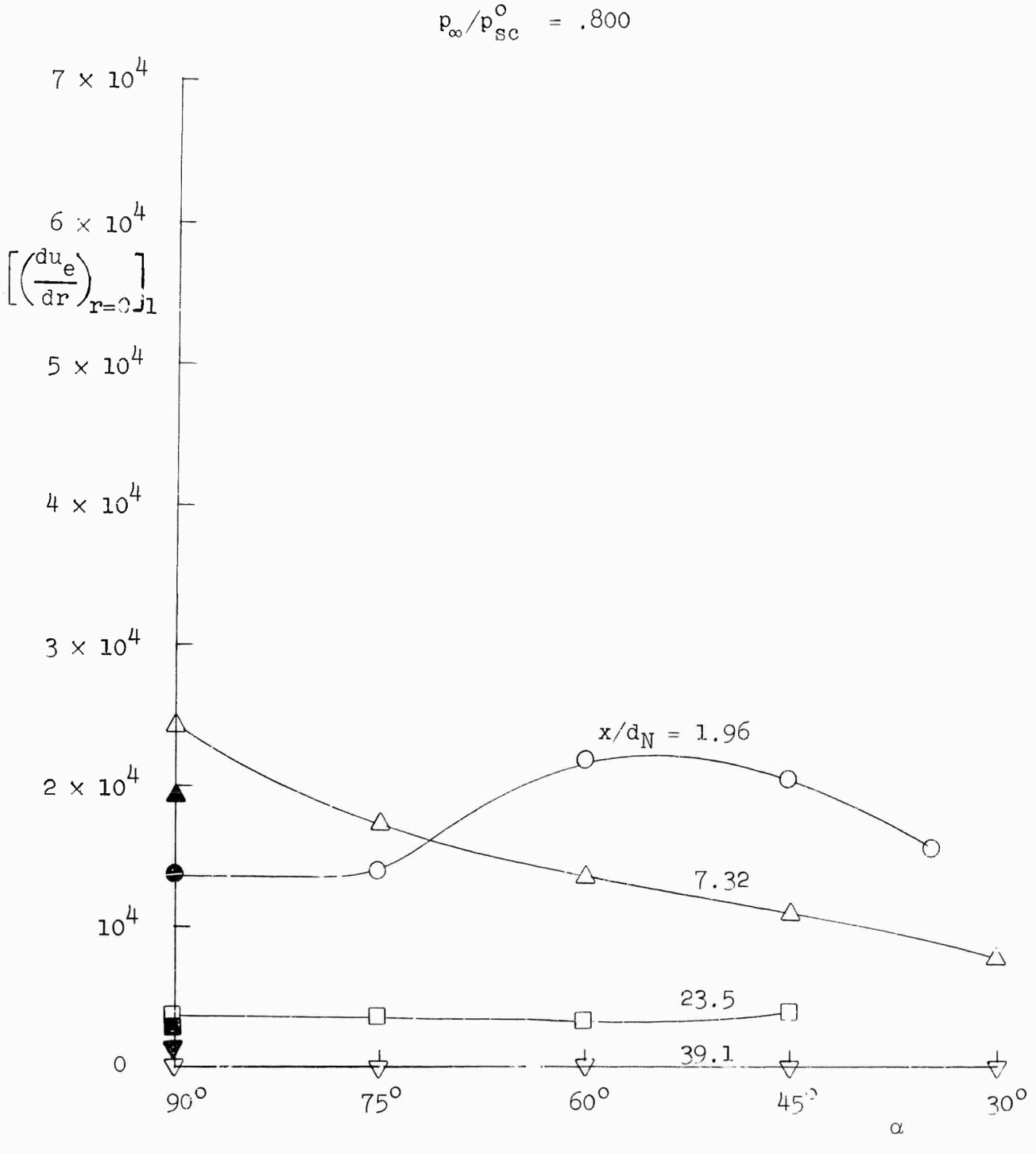

Figure 30. Dependence of radial velocity gradient $[(du_e/dr)_{r=0}]_1$ on angle of impingement.

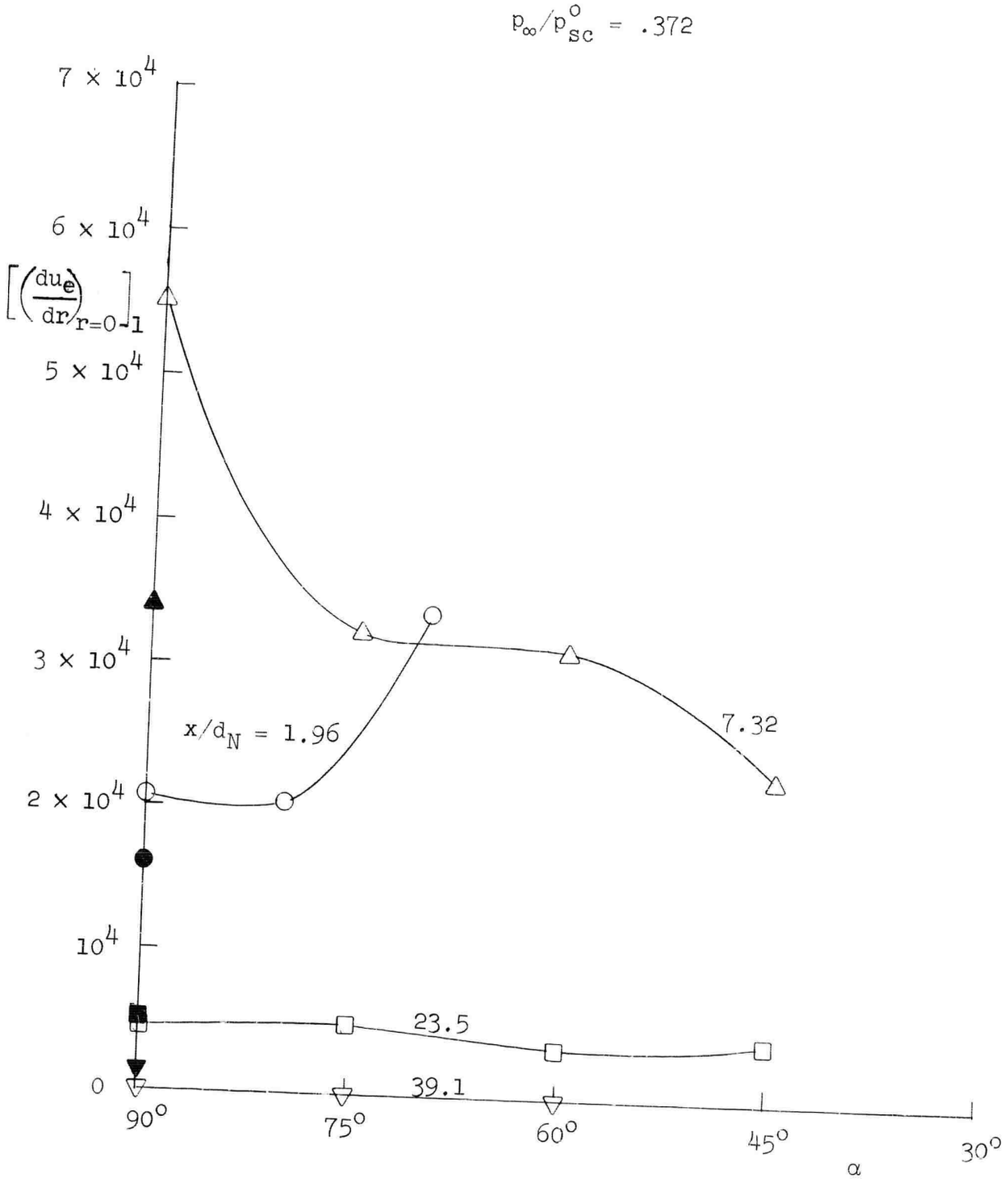

Figure 31. Dependence of radial velocity gradient $[(du_e/dr)_{r=0}]_1$ on angle of impingement.

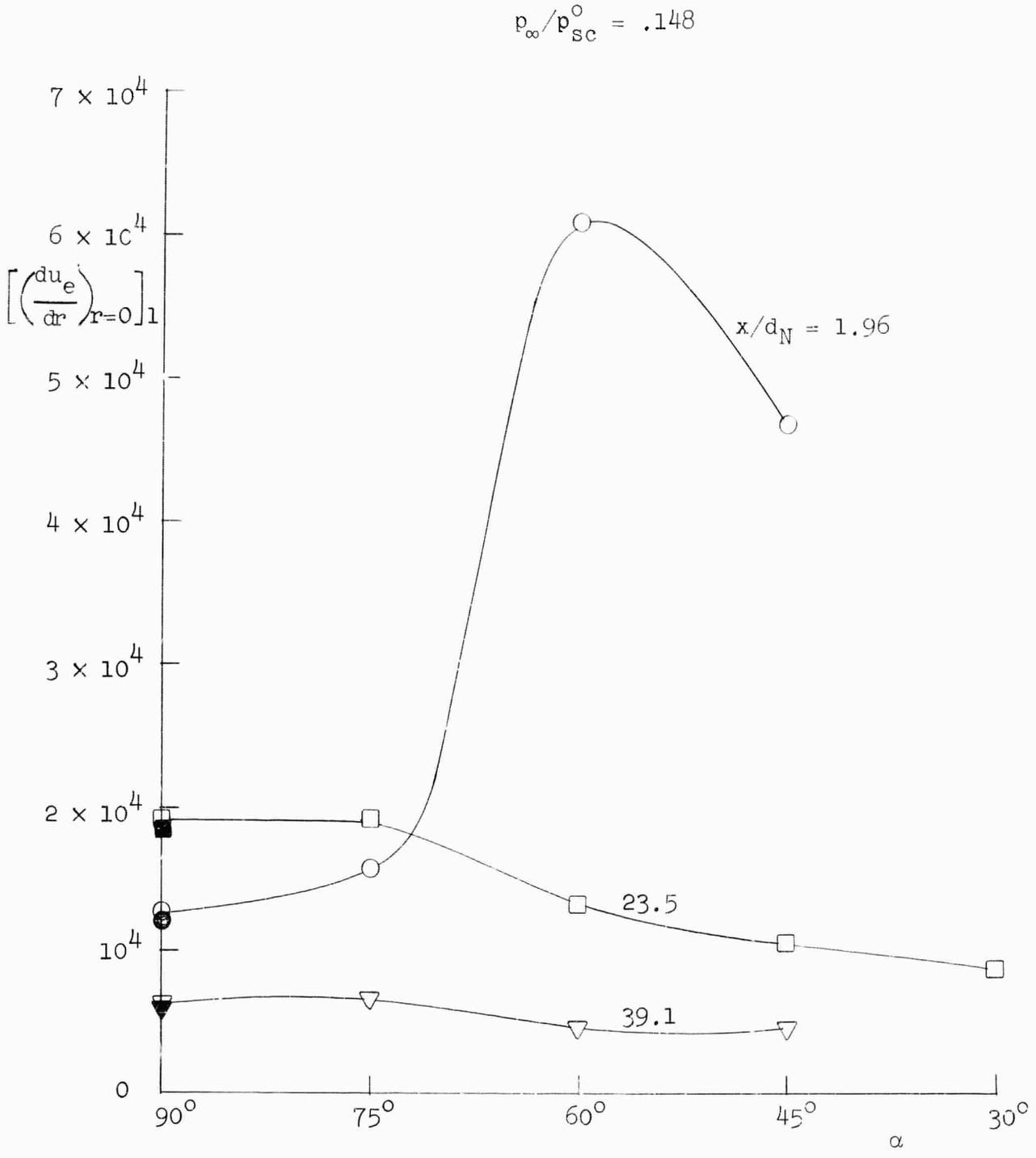

Figure 32. Dependence of radial velocity gradient $[(du_e/dr)_{r=0}]_1$ on angle of impingement.

90° and 75°. The two available cases exhibit a maximum near $\alpha = 60^\circ$ with a decrease thereafter. The two weakest jets show a continuous drop-off from $\alpha = 90^\circ$ at $x/d_N = 7.32$, a point near the end of the core in both cases. It was felt that meaningful values of $[(du_e/dr)_{r=0}]_1$ could not be deduced from the data for $p_\infty/p^\circ_{sc} = .148$ at $x/d_N = 7.32$ (see Figure 15). Farther downstream at axial stations $x/d_N = 23.5$ and 39.1, the available data show relatively little change except for $p_\infty/p^\circ_{sc} = .148$ where a continuous drop-off is noted for $\alpha < 75^\circ$. However, for $x/d_N = 39.1$, the resolution of the data was not sufficient to produce a nonzero value of $[(du_e/dr)_{r=0}]_1$ for the two weakest jets, so the detailed behavior with α could not be determined. The downstream behavior for $p_\infty/p^\circ_{sc} = .148$ may be similar to that farther upstream for the other jets, since the core is thought to extend at least to $x/d_N = 20$ in this case.

Cross plots of the measured values of $[(du_e/dr)_{r=0}]_1$ with x/d_N as the abscissa are given in Figures 33, 34, and 35. The relative dependence of the parameter on axial location for each impingement angle is shown. The dashed curves for $\alpha = 90^\circ$ are taken from the earlier high resolution measurements of the normal impingement study. It is clear that the values of $[(du_e/dr)_{r=0}]_1$ for the two weakest jets at $x/d_N = 7.32$ represent the greatest source of disagreement between the two sets of data. Although this disagreement is sizable for one case -- 60 per cent for $p_\infty/p^\circ_{sc} = .372$ -- most of these points for $\alpha = 90^\circ$ agree well within 25 per cent. In general the variation with distance follows the normal impingement behavior, although the tendency to peak near the end of the core appears to have been overcome for large obliqueness (see $\alpha = 60^\circ$ and 45° for $p_\infty/p^\circ_{sc} = .800$).

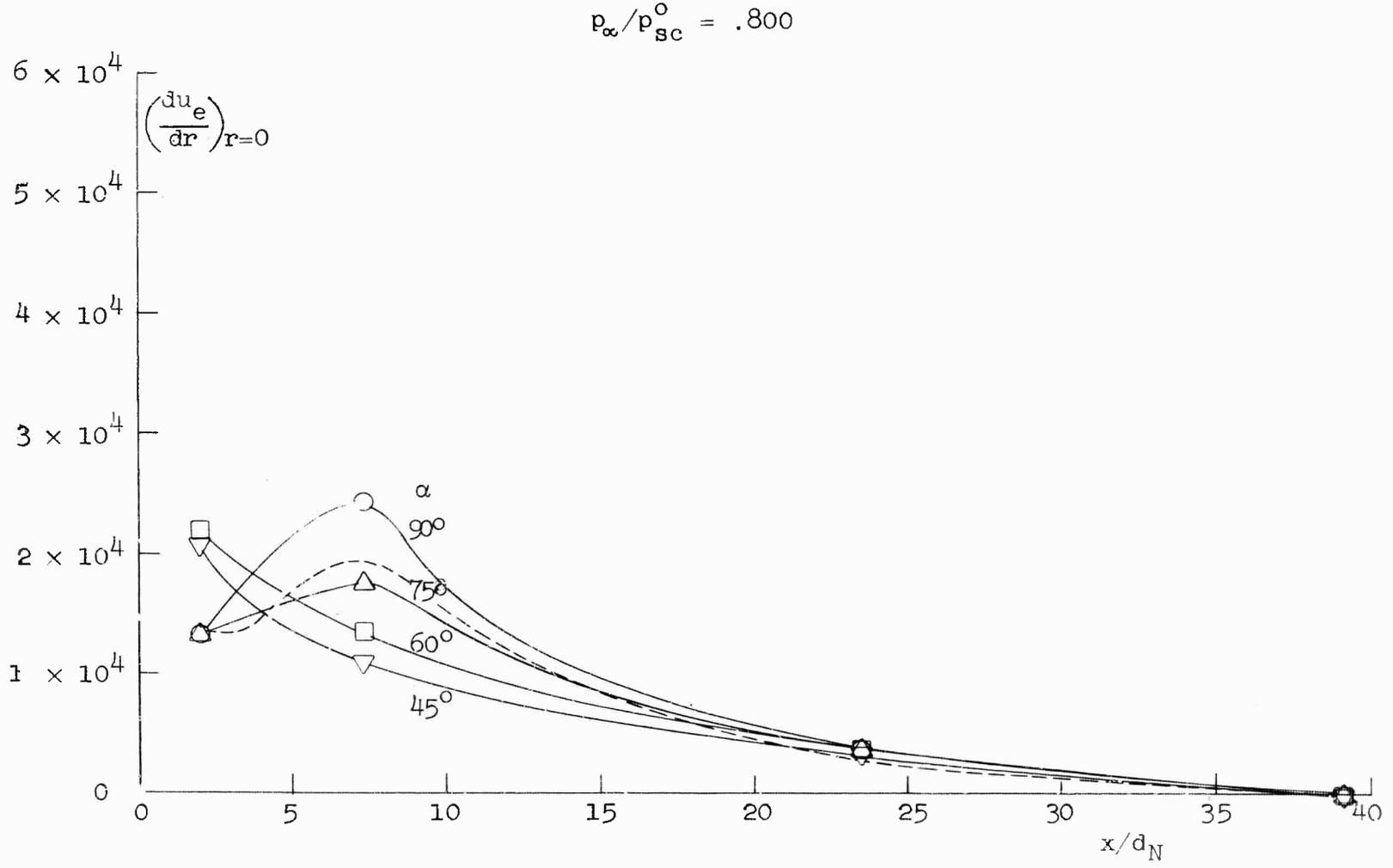

Figure 33. Dependence of radial velocity gradient $[(du_e/dr)_{r=0}]_1$ on axial impingement distance.

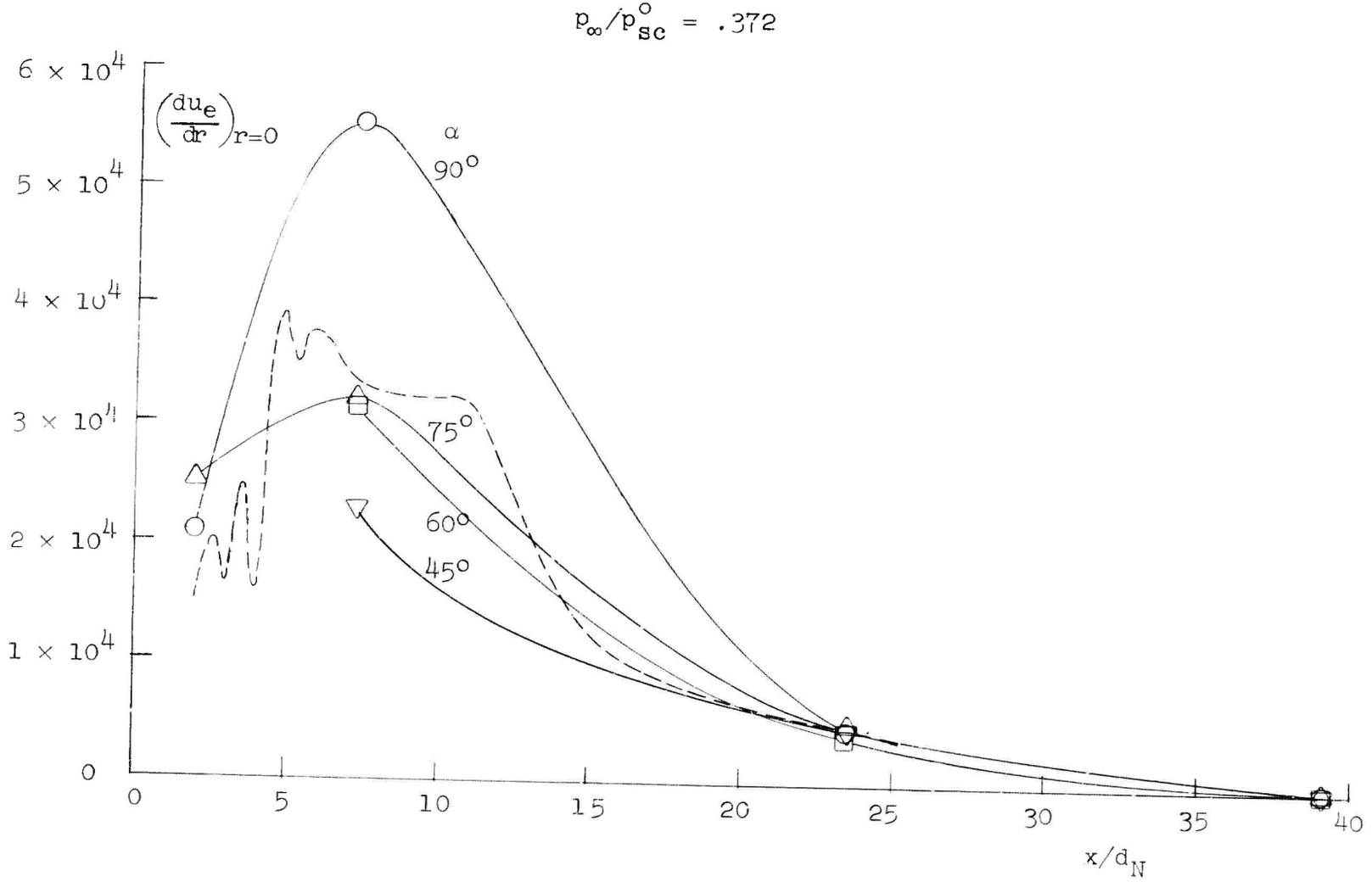

Figure 34. Dependence of radial velocity gradient $[(du_e/dr)_{r=0}]$ on axial impingement distance.

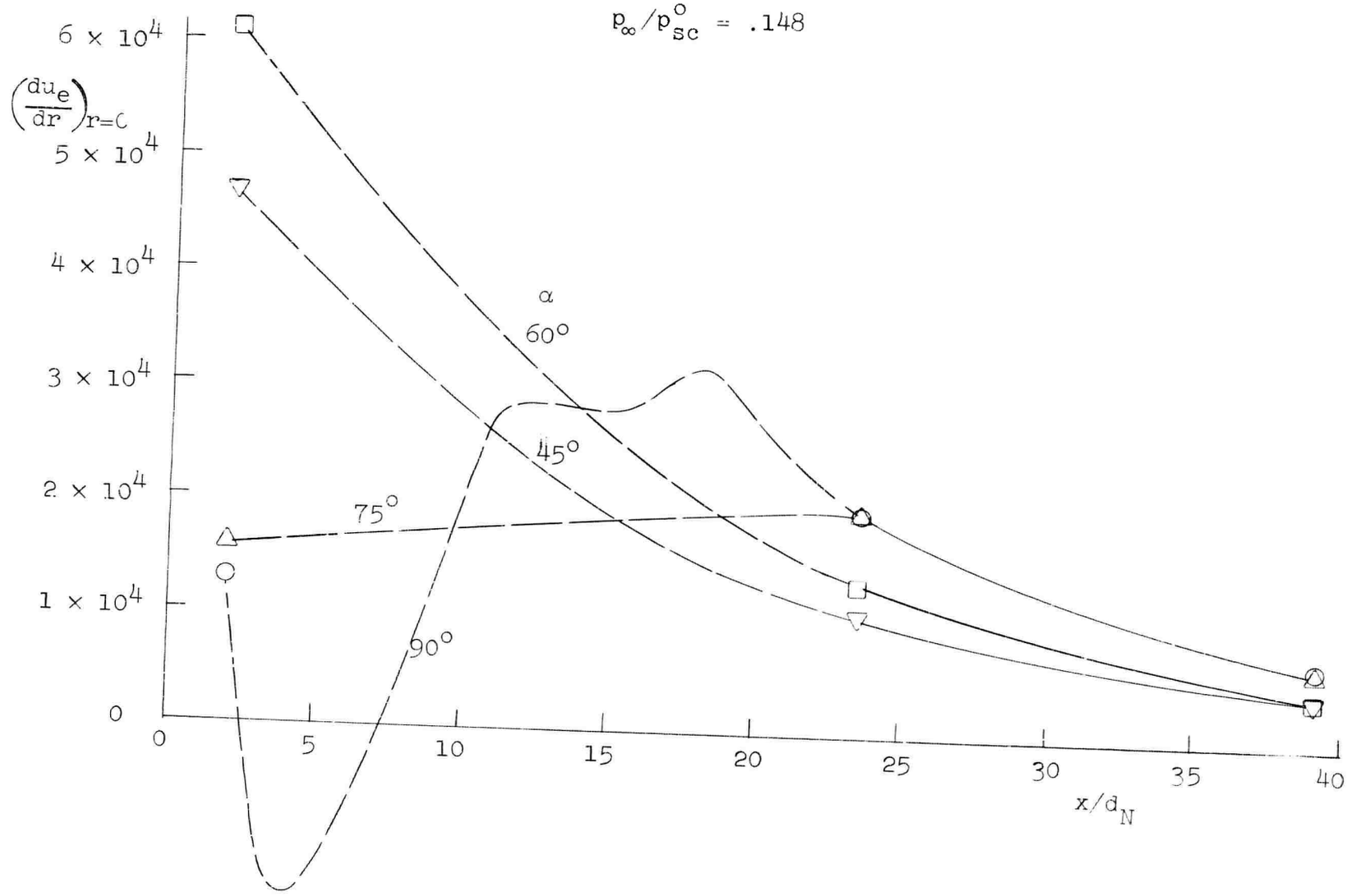

Figure 35. Dependence of radial velocity gradient $[(du_e/dr)_{r=0}]_1$ on axial impingement distance.

The detailed study of normal impingement [1] revealed that a useful correlation exists between $[(du_e/dr)_{r=0}]_1$ and the local properties of the free jet at the impingement location, namely the centerline velocity V_c and the half-velocity radius $r_{.5}$. The nondimensional form

$$\frac{r_{.5}}{V_c}\left(\frac{du_e}{dr}\right)_{r=0}$$

when applied to data from all three jet strengths was found to produce reasonable agreement among the jets for stations downstream of the core. This was so in spite of varying degrees of underexpansion and the accompanying shock structure. Such nondimensional values of $[(du_e/dr)_{r=0}]_1$ have also been computed using the present data for oblique impingement. The free jet data used (V_c and $r_{.5}$) were the same as those used earlier. In Figures 36 and 37, the results are plotted with all three jets compared at each axial station. In Figure 38, the data for all the stations except $x/d_N = 1.96$ have been plotted together. It is difficult to tell from these rather limited data if a meaningful correlation is indicated. The subsonic and moderately underexpanded jets at $x/d_N = 7.32$ do appear to give similar results, whereas there is a sizeable spread between these two jets at $x/d_N = 23.5$. Over all, the values are relatively insensitive to α in the range $90^\circ \geq \alpha \geq 75^\circ$ except when $x/d_N = 7.32$. The combined plot of Figure 38, which presents all cases based on nearly similar jet velocity profiles, i.e. cases other than those of core impingement, is indicative of the general decrease in $(r_{.5}/V_c)[(du_e/dr)_{r=0}]_1$ for increasing obliqueness. It is seen that the data fall within a spread of approximately 50 per cent, an amount which includes not only differences due to jet structure and impingement behavior, but also those due to the limited accuracy of the data.

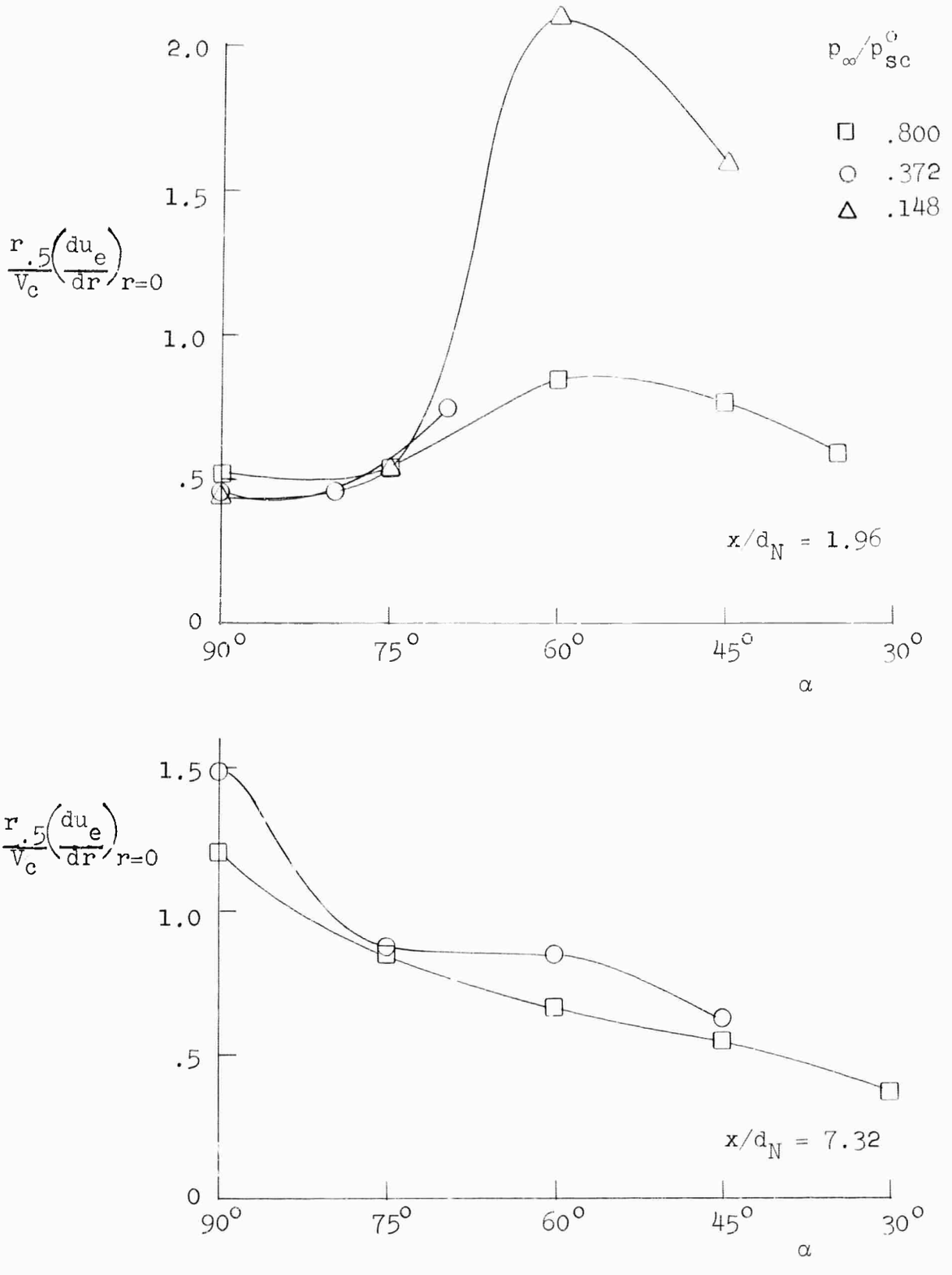

Figure 36. Dependence of nondimensional radial velocity gradient on angle of impingement.

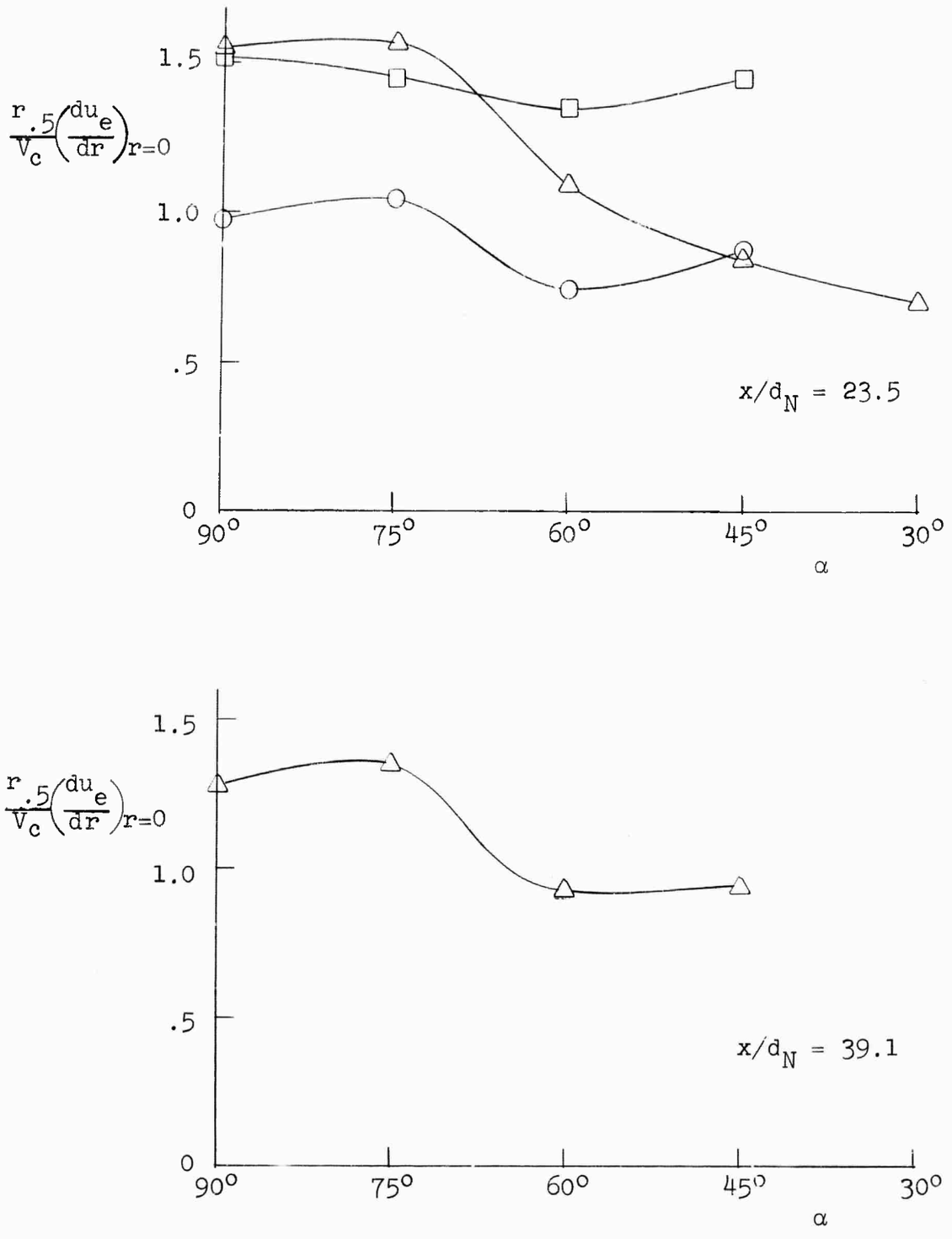

Figure 37. Dependence of nondimensional radial velocity gradient on angle of impingement.

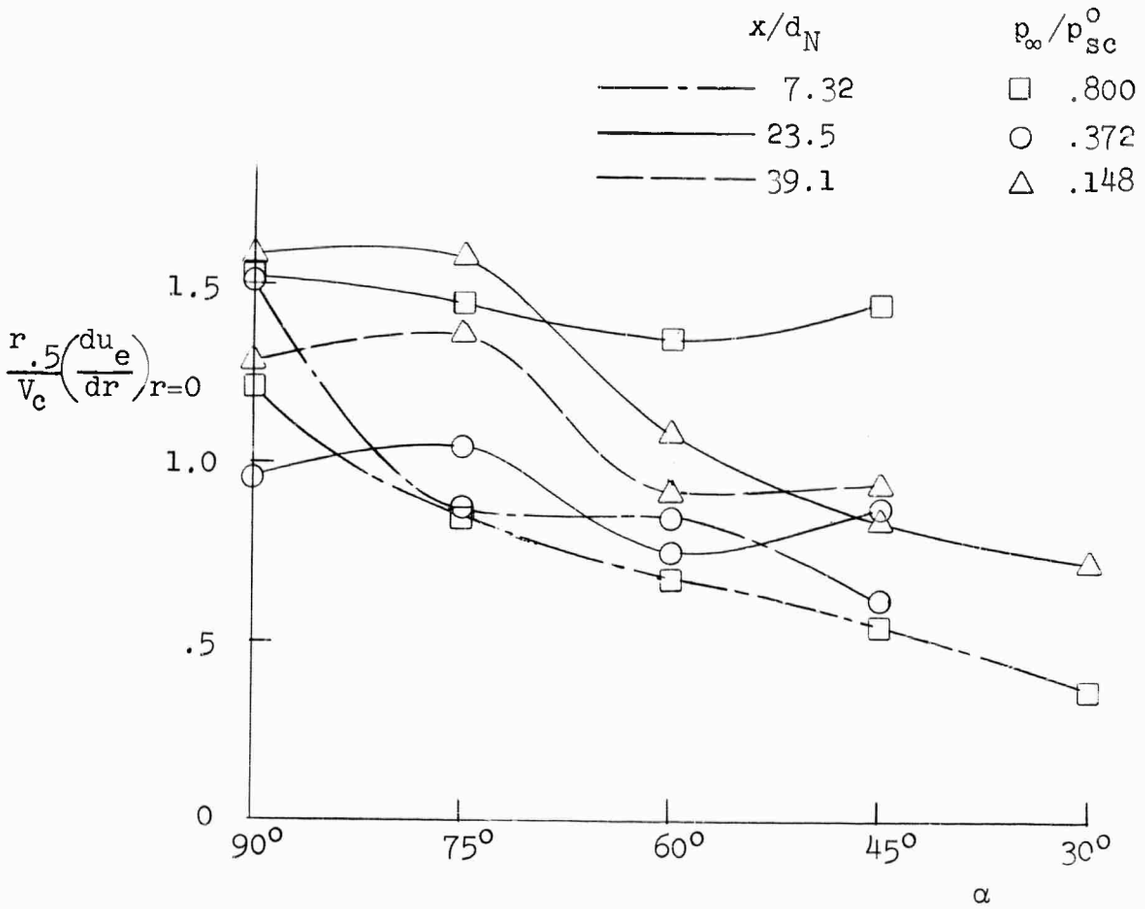

Figure 38. Dependence of nondimensional radial velocity gradient on angle of impingement.

It appears that some general qualitative characteristics of the changes in $[(du_e/dr)_{r=0}]_1$ due to obliqueness can be described on the basis of the data just presented. It has been observed that $[(du_e/dr)_{r=0}]_1$ changes very little in the range $90^\circ \geq \alpha \geq 75^\circ$ for both core impingement $(x/d_N = 1.96)$ and impingement of the fully developed region $(x/d_N = 23.5$ and $39.1)$, whereas the cases of core-end impingement $(x/d_N = 7.32)$ show a fairly high α - sensitivity in the same range. In terms of jet velocity profiles or impingement pressure distributions, the latter case represents the profile with the sharpest central peack while the others have either flat or relatively flat central regions. At $x/d_N = 1.96$ there is a sharp rise between $\alpha = 75^\circ$ and $\alpha = 60^\circ$, followed by a drop-off for angles $\alpha < 60^\circ$. In this case, the flat central portion of the velocity profile falls away sharply at the edge of the core and gradually assumes a fully developed mixing profile. These comparisons indicate that, as might be expected, the local shape of the impinging velocity or total head profile is an important factor in determining the degree of α - sensitivity at each axial station.

2.5. Azimuthal Distribution of the Wall Jet.

2.5.1. Basic wall jet characteristics. The turbulent wall jet regime has been described earlier as that portion of the flow in which the effects of interaction due to impingement are no longer important. As such, it consists of an inner region adjacent to the plate, dominated by the viscous shearing stresses of the boundary layer, with an outer layer of free turbulent mixing. As the jet flows radially outward, each of these layers tends to develop in a way determined by the balance of forces peculiar to each type of flow. Basically, the mixing layer alone tends to spread in a

direction normal to the flow while, at the same time, decaying under the influence of mixing or entrainment of ambient fluid. The development of the boundary layer portion is also characterized by a growth in thickness normal to the flow which is due to a loss of momentum to the wall through the action of laminar shearing forces. Because of the basic differences in the processes governing the growth of the two layers, the wall jet resulting when these two processes are combined cannot establish a characteristic self-similar profile. Glauert [6] has shown that for an incompressible flow this departure from similarity is very slight, there being a tendency for the boundary layer to grow somewhat more rapidly in proportion to the over-all profile growth. It is shown that the decay and spreading parameters which govern the combined growth rate are dependent upon the local Reynolds number of the flow. Typically, for the present flows in which the Reynolds number based on wall jet thickness ranges from 10,000 to 200,000, Glauert's results predict a velocity decay proportional to $r^{-1.1}$ with a thickness increase proportional to $r^{1.01}$. Although the present experiments were devoted primarily to the azimuthal distribution of the wall jet at a single radial station, some additional measurements were made for a typical impingement condition in which a profile was determined for two other radial stations.

One of the important characteristics of a radial wall jet flow is the way in which the azimuthal distribution of the total mass flux is altered when the impingement is made oblique. Since the radial fluxes of momentum and energy per unit azimuth depend upon this distribution, it is particularly important if one is interested, say, in the local heat transfer between such a jet and a surrounding wall or enclosure. Certain characteristics of the flow appear to be obvious, such

as the increasing proportion of mass flux in the downstream direction as α is made smaller. On the basis of inviscid theory, one might also expect a tendency toward a corresponding increase in thickness. However, the actual roles of such real effects as turbulent mixing, stagnation point displacement, nonradial flow components, and the nature of the impinging jets have to be deduced from the experimental data.

As a useful way of describing a flow that is subject to this variety of influences, a concept based on the division into sectors of the impinging jet is suggested. For normal impingement, each sector of wall jet flow would be the result of the impingement of a corresponding sector of the given free jet flow. The wall jet sectors would each maintain their original radial momentum flux, neglecting the slight loss in the boundary layer, and would spread and decay identically. Applying this idea to oblique impingement, it is imagined that each sector again retains its original radial momentum and spreads and decays as before. Here, however, since each sector may have a different momentum level, it is thought of as resulting from the impingement of a corresponding sector of a hypothetical free jet having just the required momentum. Physical considerations, of course, would also require that the shear between adjacent sectors of such a flow be negligible compared to that at the solid and free boundaries. The measurements made at two additional radii for a typical impingement condition can be used to estimate the validity of this hypothesis.

2.5.2. Experimental results. The experimental program consisted of the measurement of Pitot pressure profiles at several locations along the perimeter of the circular impingement plate (see Figure 4) for a number of jet

strength, axial location, and impingement angle combinations. Velocities were computed from the Pitot pressure by assuming a constant static pressure equal to ambient. Because of the very large number of cases to be treated, the original matrix of four axial locations and three jet strengths was changed somewhat. The cases actually used included one jet strength (moderately underexpanded $p_\infty/p^\circ_{sc} = .372$ at each of five axial locations and five jet strengths at a single axial location. The nine cases are tabulated as follows:

x/d_N	p_∞/p°_{sc}
1.96	.372
7.32	.800, .552, .458, .372, .148
11.7	.372
23.5	.372
39.1	.372

For each of these combinations, the profile was determined at five azimuthal positions ϕ along the perimeter of the plate with the impingement angle α varying from 90° to 45°. In order to obtain profiles for one entire half-circumference of the plate, i.e. $0 \geq \phi \geq 180$, with the Pitot tube rake limited to positions in one quadrant, the plate was positioned at α and $180 - \alpha$ for each ϕ. The values of ϕ and α used are tabulated below.

ϕ \ α	90	75	105	60	180	45	135
0	✓	✓	✓	✓	✓	✓	✓
22.5	✓	✓	✓	✓	✓	✓	✓
45	✓	✓	✓	✓	✓	✓	✓
67.5	✓	✓	✓	✓	✓	✓	✓
90	✓	✓	✓	✓	✓	✓	✓

The total number of profile cases measured thus came to 315. With this quantity of data to obtain, it was felt that a further simplification might be tolerated in the profile measurements themselves with only a small sacrifice in accuracy. First, however, a single combination of jet strength and impingement distance was studied in detail in order to establish basic profile characteristics. For each ϕ and α the profile was determined using the rake in a fine scale traverse of the jet. The case chosen was the one with $p_\infty/p^o_{sc} = .372$ at $x/d_N = 1.96$, The jet was of the moderately underexpanded type which provided easily measurable Pitot pressure levels, while the axial location was close enough to assure a well-developed wall jet at the edge of the plate. The velocity profiles resulting from this detailed study are shown in Figures 39 and 40 plotted in nondimensional form with the maximum velocity u_{max} and the half-velocity thickness normal to the plate $n_{.5}$ as normalizing parameters.* With the exception of a few scattered points, it is seen that all of the profiles are essentially the same. A single curve which represents a good fit for all of these cases is shown in Figure 41 together with a curve based on Glauert's analysis. Glauert shows that the change in growth of such a jet with decreasing Reynolds number is primarily due to the growth of the boundary layer portion, with the shape and thickness of the outer mixing layer remaining practically constant. In order to select a curve for comparison with the data, the boundary layer thickness, i.e. the thickness to $u = u_{max}$, was made to coincide with the experimental result and the outer profile was passed through the point

*It should be noted that $n_{.5}$ as used herein includes the thickness of the boundary layer portion of the flow.

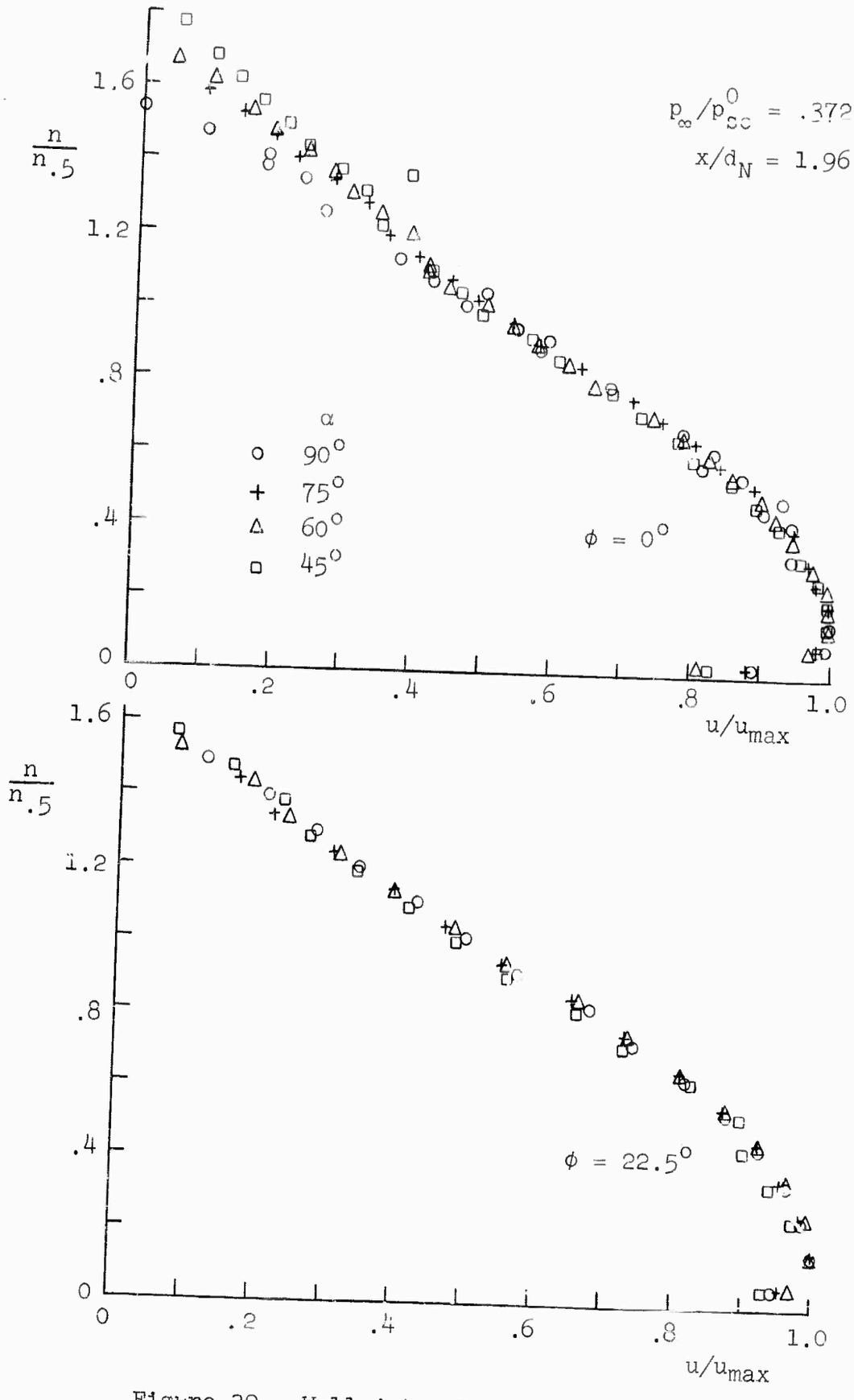

Figure 39. Wall jet velocity profiles.

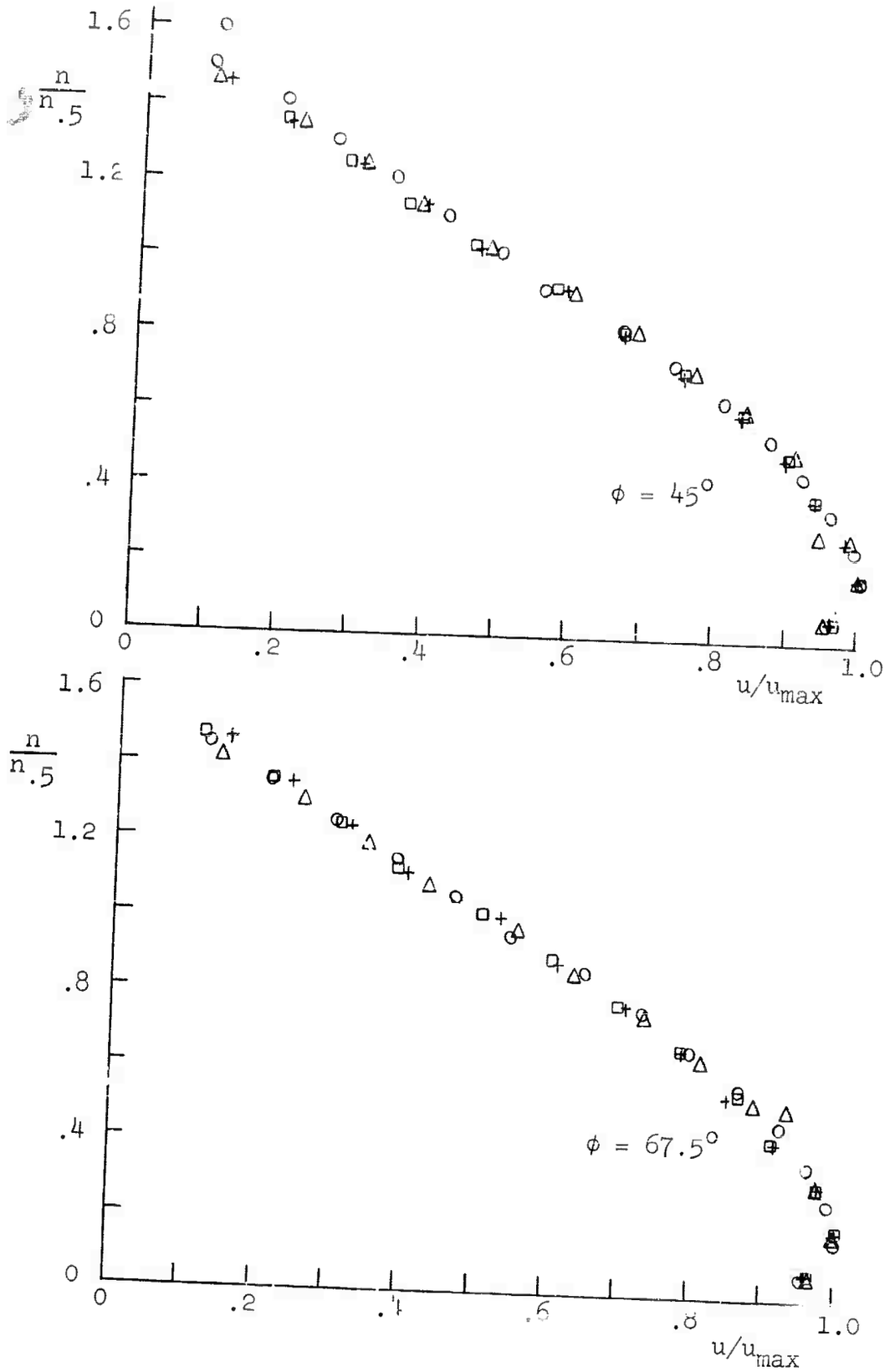

Figure 39. (Continued)

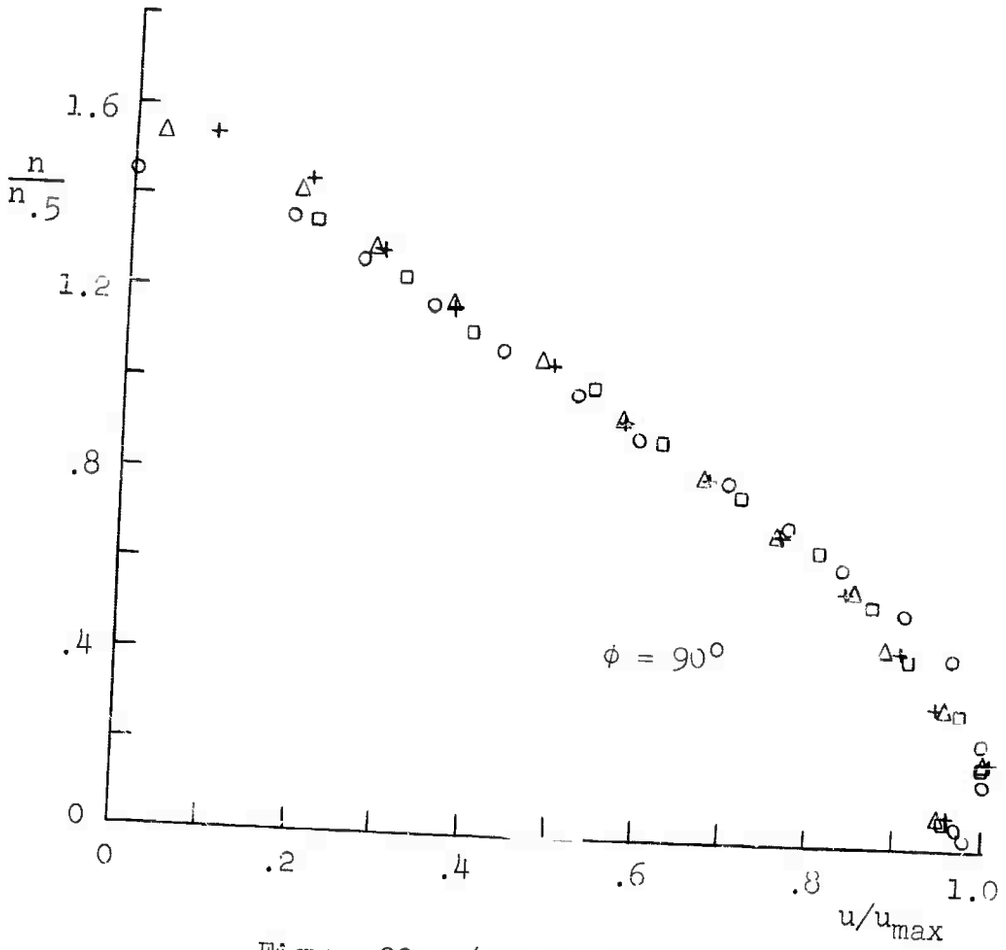

Figure 39. (Concluded)

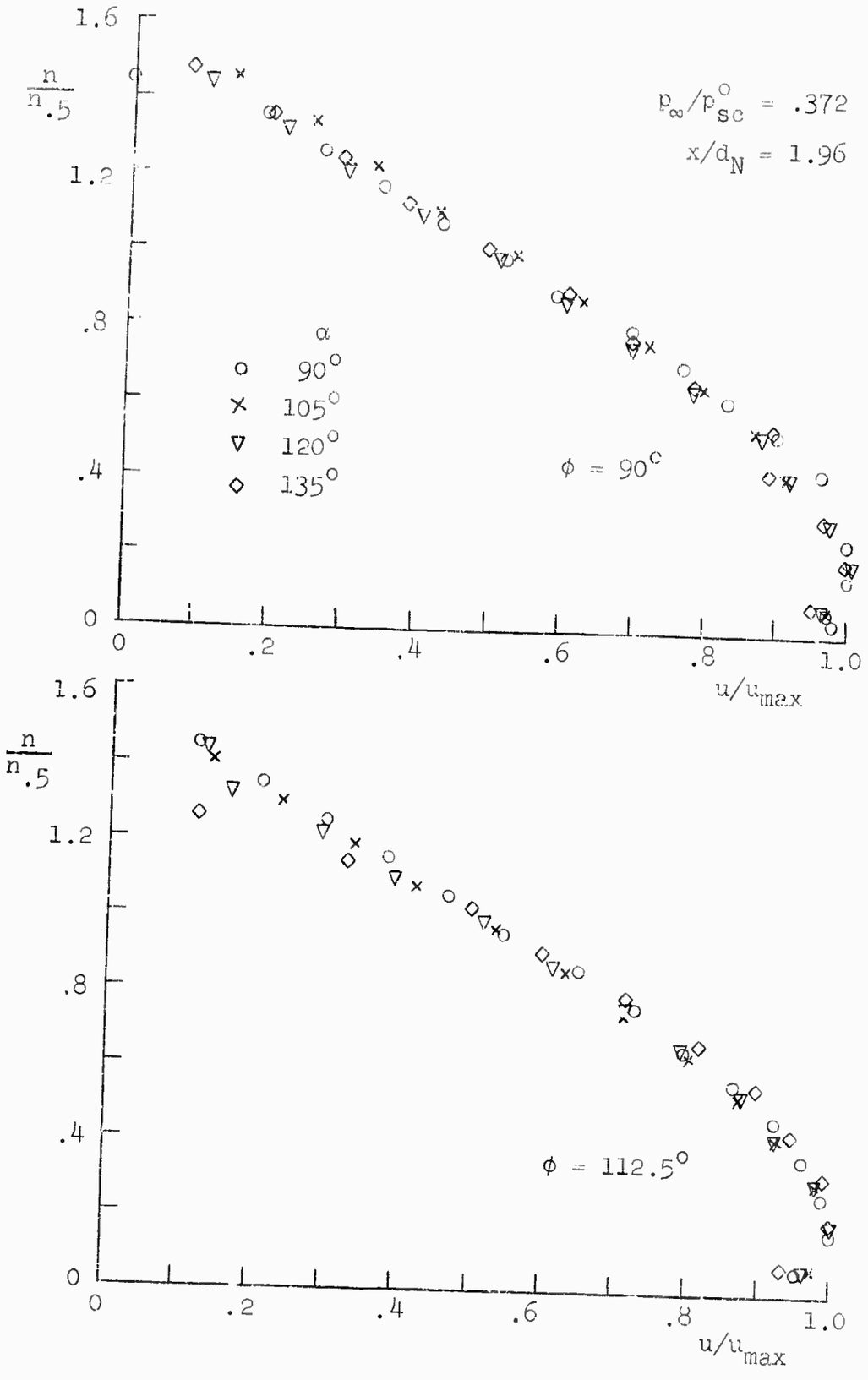

Figure 40. Wall jet velocity profiles.

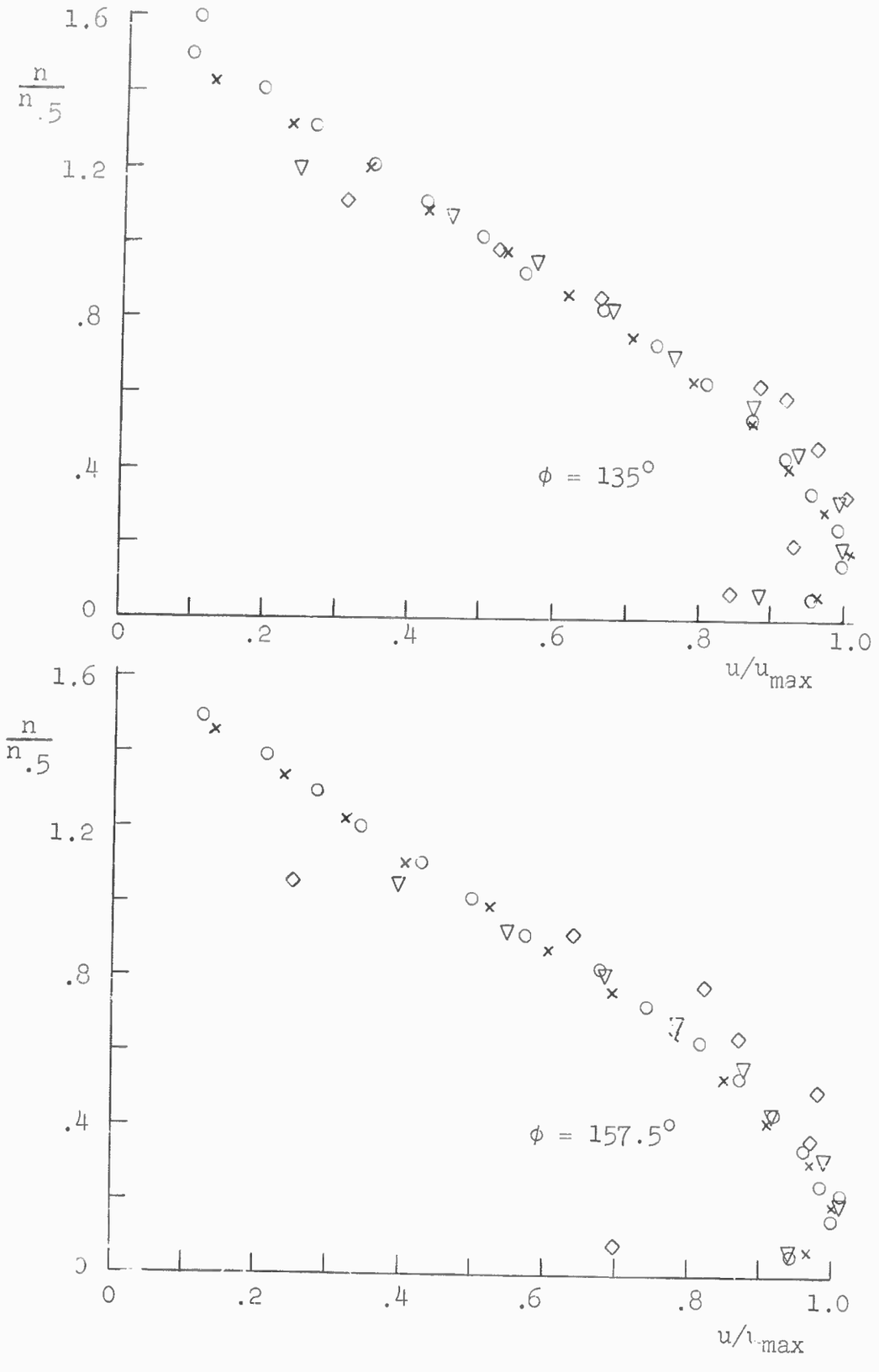

Figure 40. (Continued)

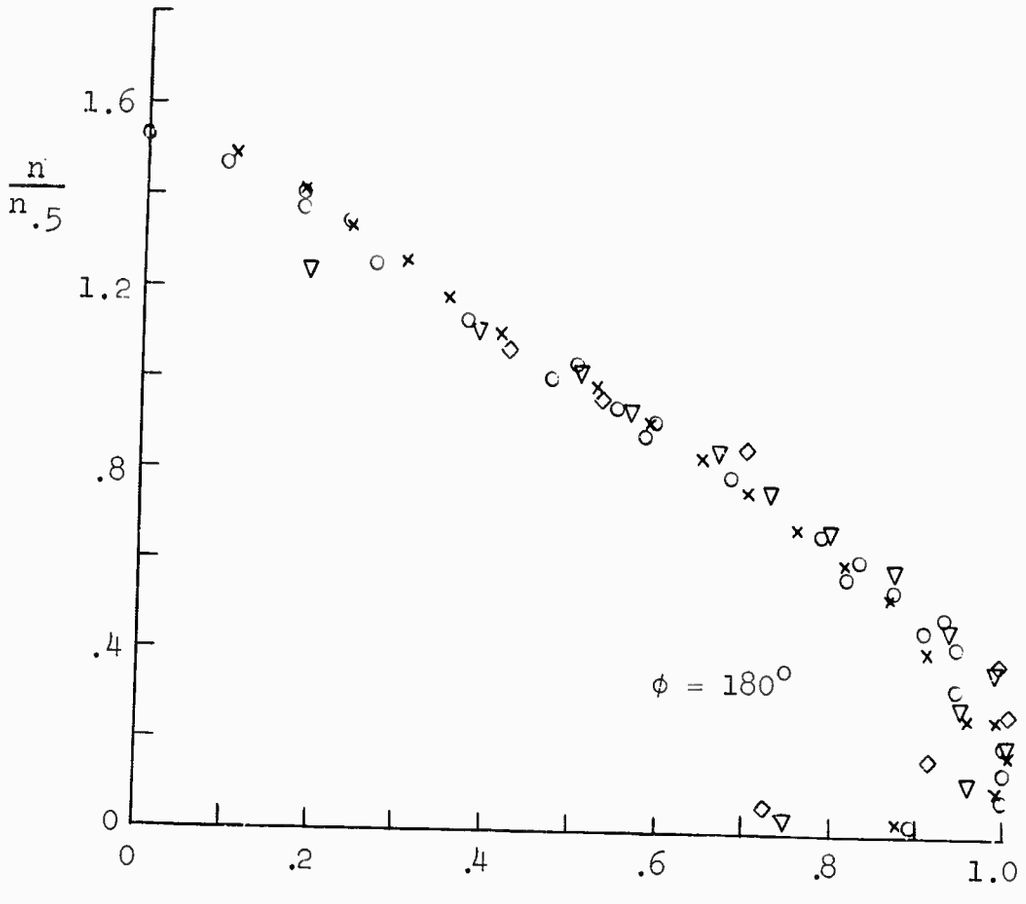

Figure 40. (Concluded)

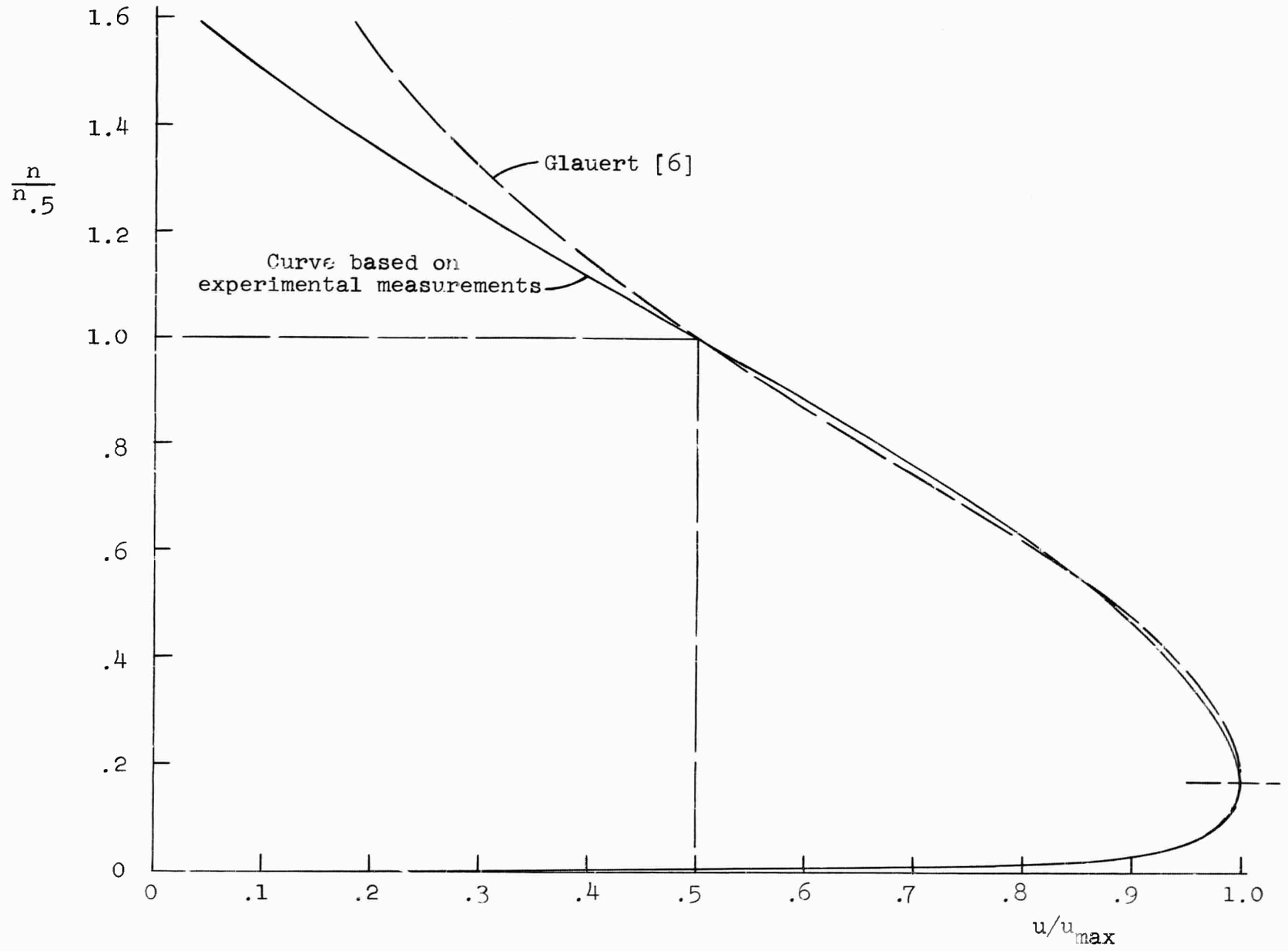

Figure 41. Comparison of experimental curve with that based on Glauert's theory.

$n = n_{.5}$. The resulting curve coincides with a distribution obtained from Glauert's results for a Reynolds number $u_{max}\delta/\nu = 13{,}000$ where δ is the half-velocity thickness of the outer layer only (distance between points for u_{max} and $.5u_{max}$). This Reynolds number is representative of profiles near the low end of the range of Reynolds numbers (10,000 to 200,000) covered by the data. Since a Glauert profile for a Reynolds number of 200,000 has a significantly thinner inner layer than was measured in these tests, it is concluded that the present data show somewhat less Reynolds number dependence than would be predicted by Glauert's analysis.

The simplified measurement of the velocity profiles in the bulk of the cases was based upon the assumption that they would all approximate the basic experimental curve just described. At a given axial station, of course, the effective radial distance to the point of measurement changes slightly because of the α-dependence of the stagnation point location. This problem was felt to be minor. On the other hand, the spread of the impinging jet with increasing impingement distance effectively decreases the radial distance over which the wall jet can develop before reaching the edge of the plate, with the result that some change in the basic profile might be expected due to the slight lack of self-similarity discussed earlier. A check of this problem was made by making several additional detailed profile measurements farther downstream at $x/d_N = 7.32$, again with $p_\infty/p^o_{sc} = .372$ (see Figure 42). For $\phi = 0^o$ with $\alpha = 90^o$ and 60^o , the profile differs only slightly from the assumed shape near the outer edge. Although a somewhat fuller profile is found for the extreme case of $\phi = 180^o$ with $\alpha = 60^o$, the general similarity is felt to be sufficient for the purposes of these measurements. Therefore, the simplified measurement method based on

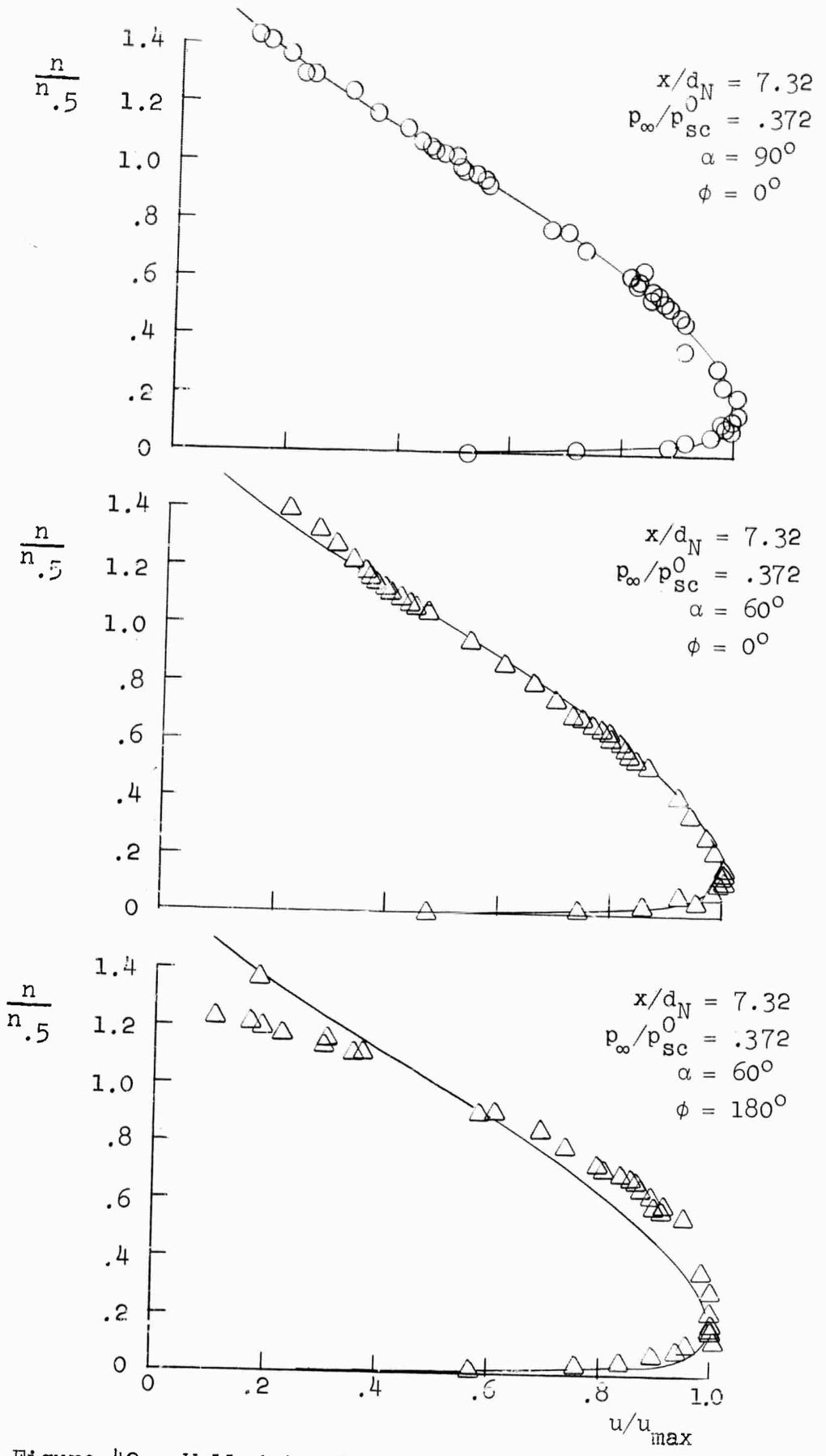

Figure 42. Wall jet velocity profiles for several different impingement conditions. The curve is that shown in Figure 41.

the established curve was applied to the remaining cases. With the jet running, the rake position was adjusted until one tube indicated the maximum Pitot pressure. The readings of all the affected tubes were then taken and the location of the rake was determined relative to the plate surface. Because of the scale of the wall jet thickness compared to the tube spacing, this single run resulted in most cases in a profile containing only three or four points, one of which defined the maximum velocity. The other parameter to be determined was $n_{.5}$, a measure of the thickness. From the basic profile shape, it is seen that the curve is very nearly a straight line at the point where $n = n_{.5}$. Since in almost every case the remaining points measured by the rake spanned this point, it was a simple matter to locate $n = n_{.5}$ using a straight line. It is felt that this procedure was sufficiently accurate to indicate the general behavior.

The results of the measurements just described are presented in Figures 43 through 46. The maximum velocities given in Figure 43 are referred to their values at $\phi = 0$ for each impingement condition.* These latter values of $(u_{max})_{\phi=0}$ are given in Figure 44 in terms of the parameters governing the impingement condition, i.e. the free jet centerline velocity V_c, and half-velocity radius $r_{.5}$ measured at the impingement distance, and the plate radius r_w. Once again, the free jet data used are taken from [1].

The azimuthal variation of $u_{max}/(u_{max})_{\phi=0}$ shown in Figure 43 appears to be relatively independent of impingement condition for the range of cases studied. Because of the large range in velocity magnitudes measured, however,

*In this discussion, the term "impingement condition" includes jet strength p_∞/p^o_{sc}, axial location x/d_N, and impingement angle α.

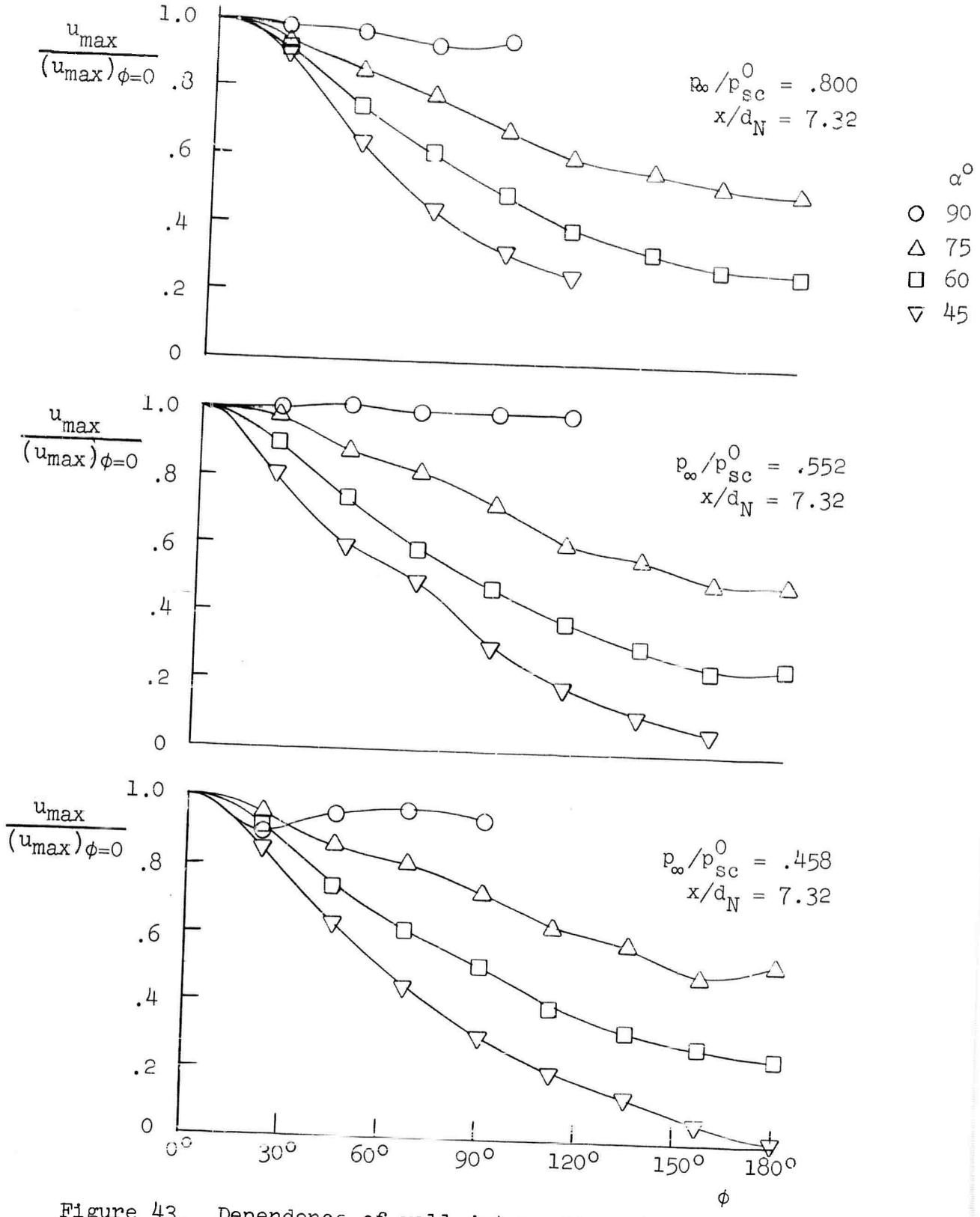

Figure 43. Dependence of wall jet nondimensional maximum velocity on azimuthal position.

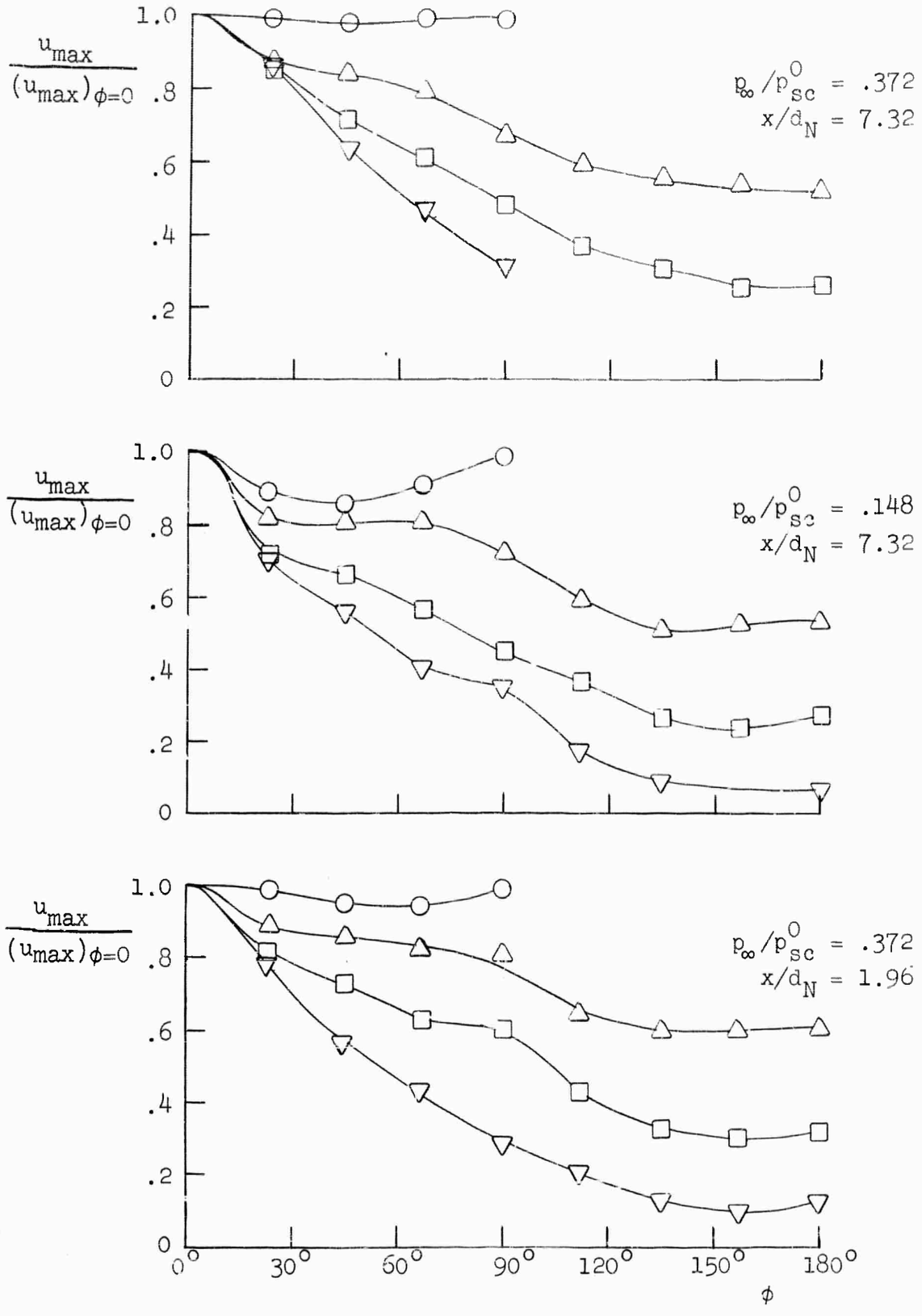

Figure 43. (Continued)

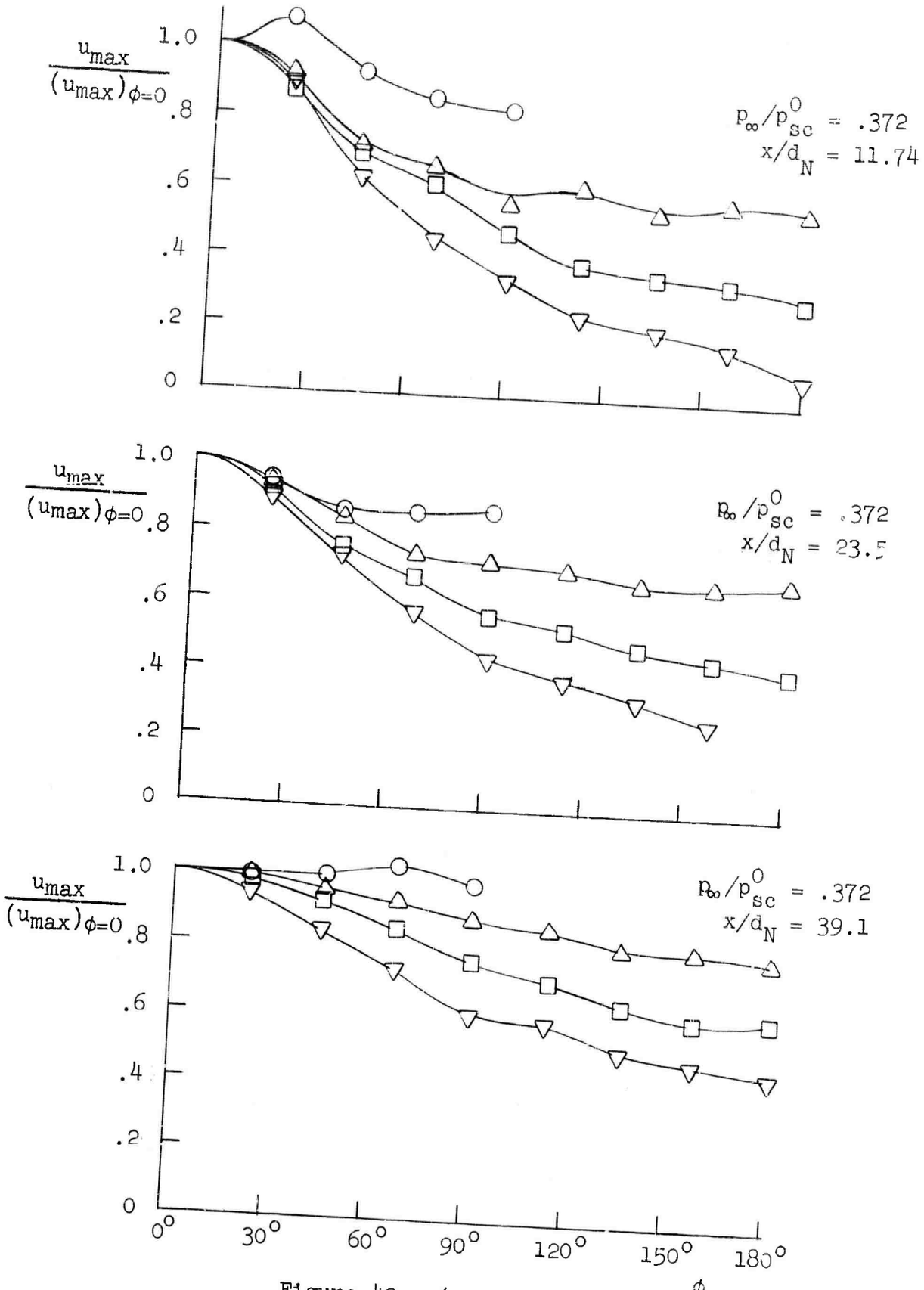

Figure 43. (Concluded)

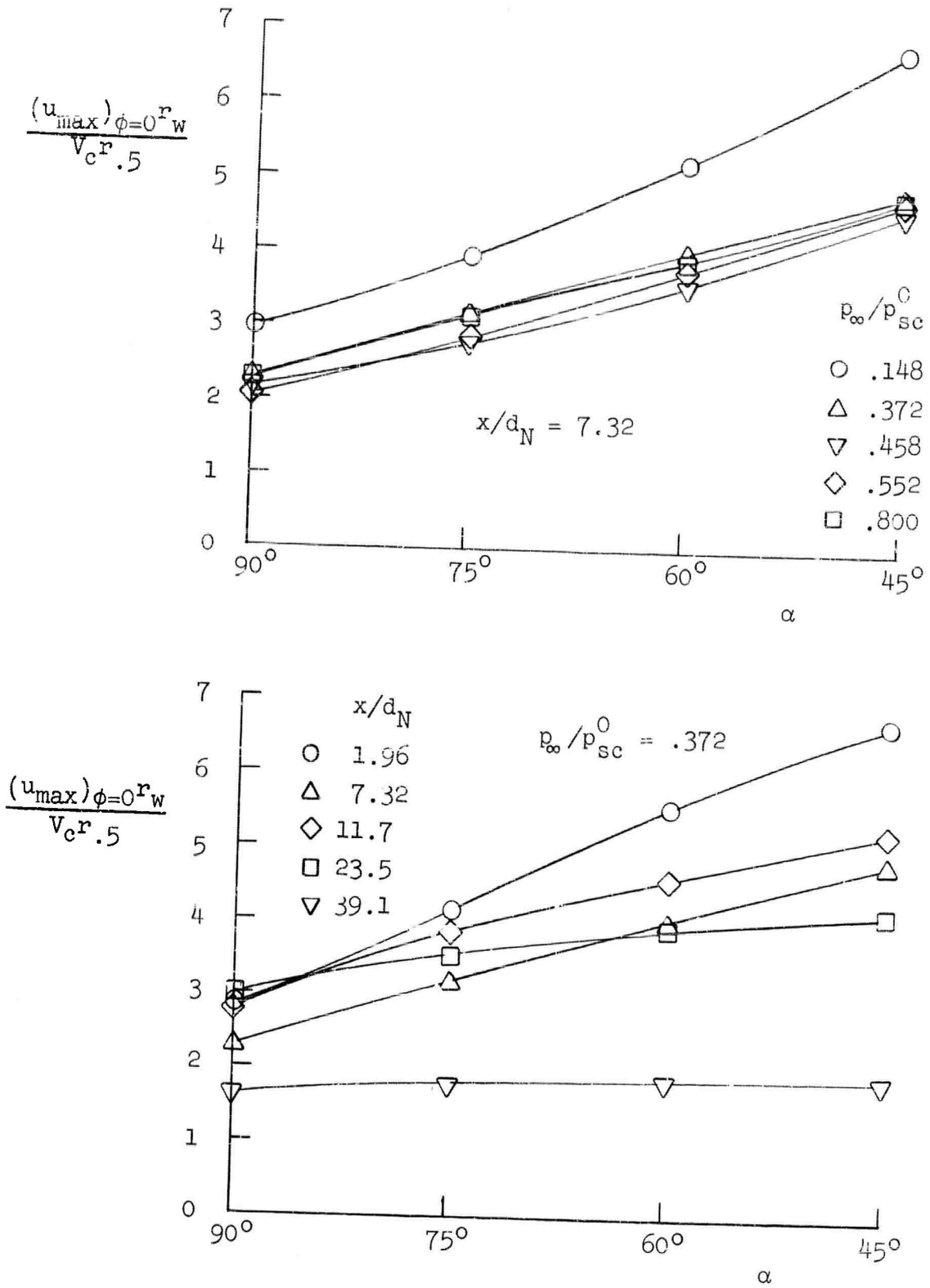

Figure 44. Nondimensional wall jet maximum velocity at $\phi = 0$ as a function of impingement angle.

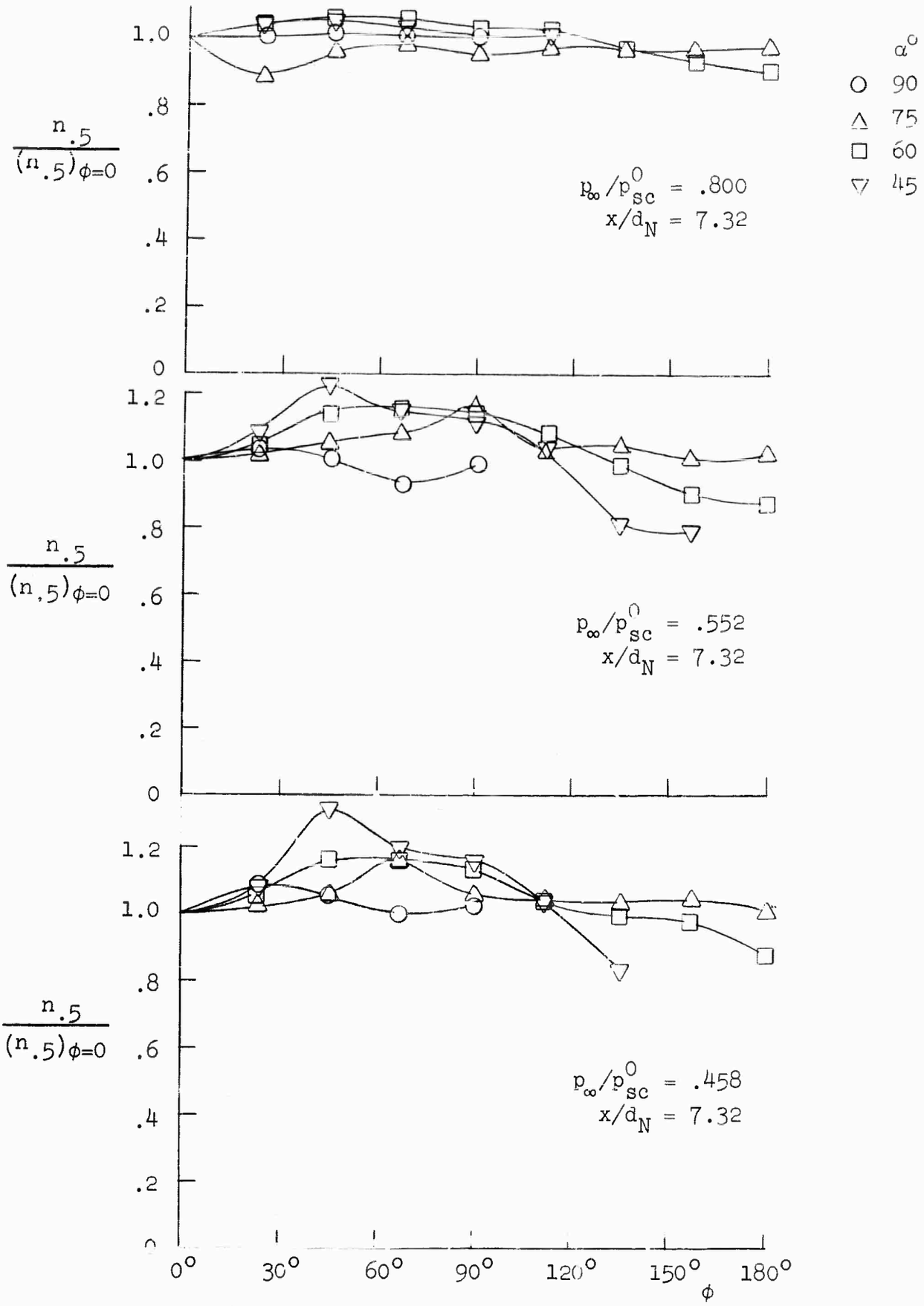

Figure 45. Dependence of wall jet nondimensional thickness on azimuthal position.

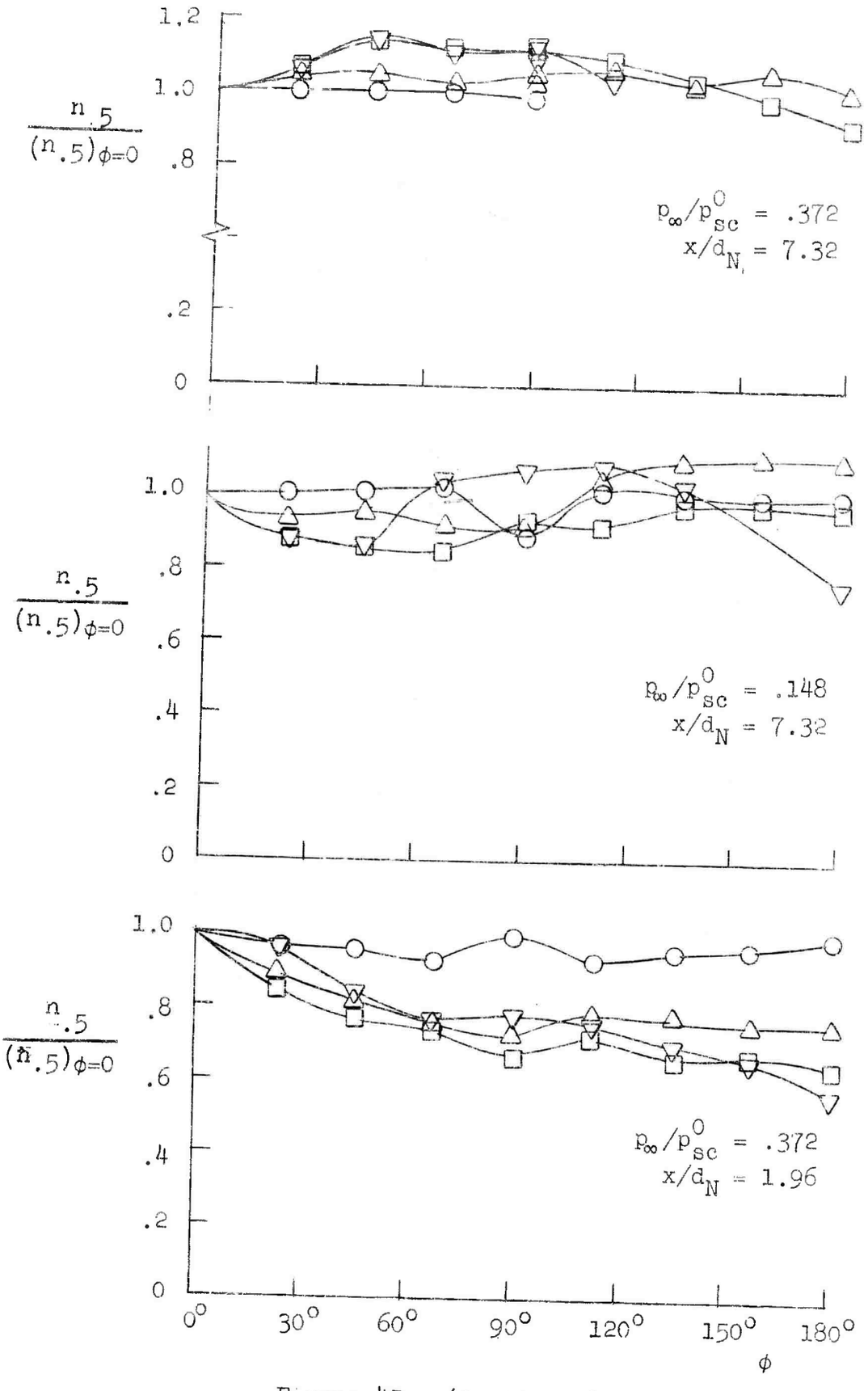

Figure 45 (Continued)

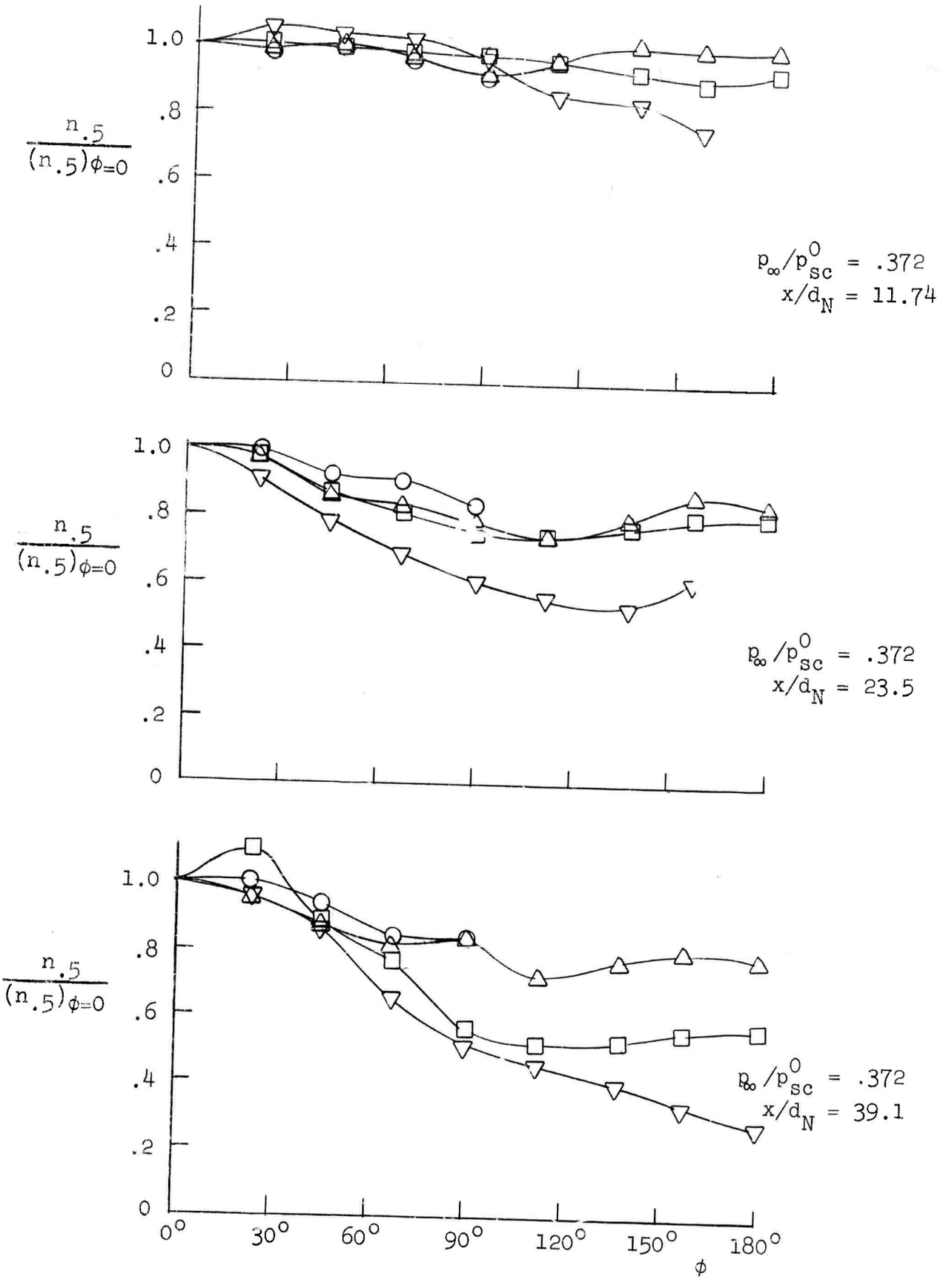

Figure 45. (Concluded)

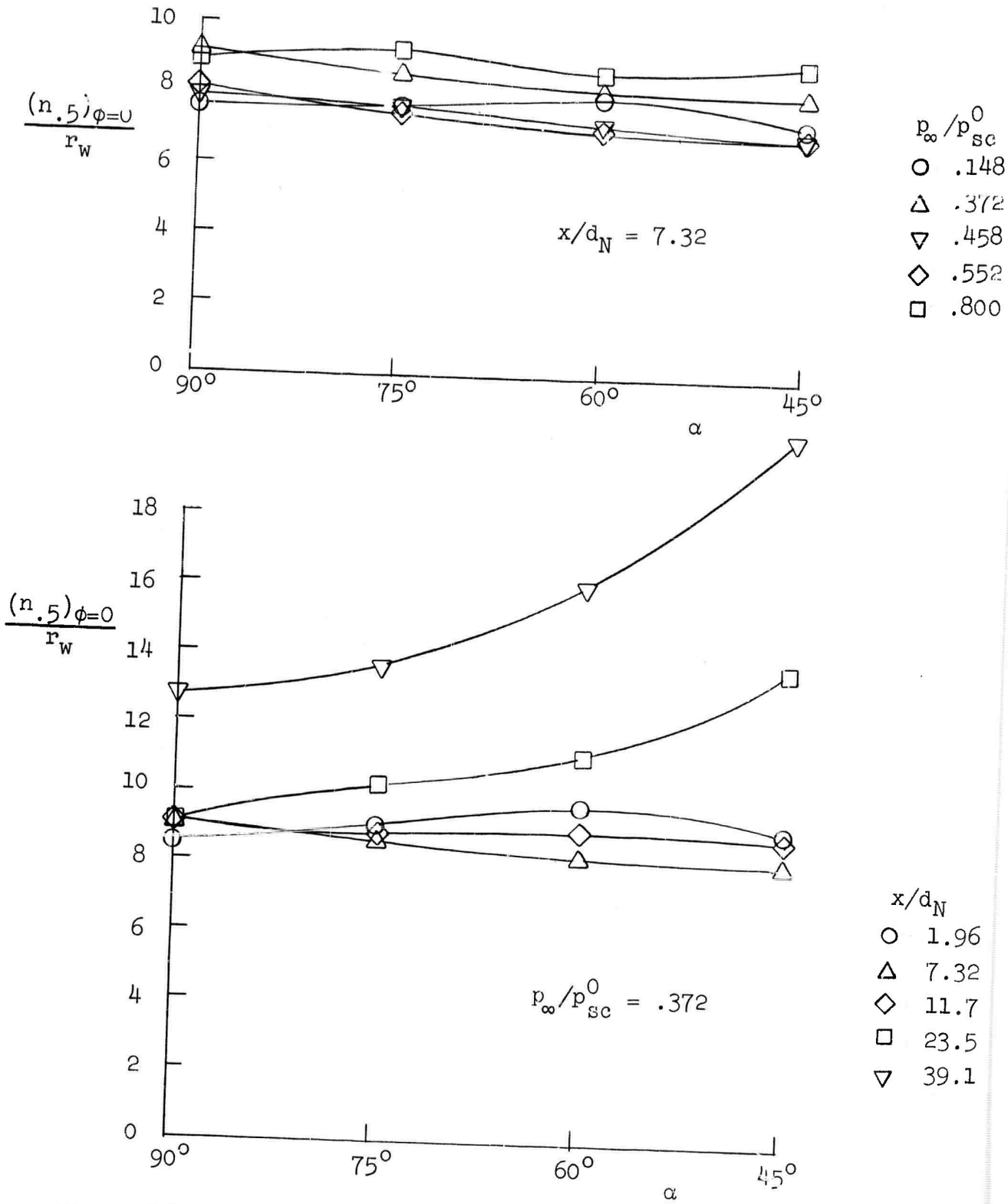

Figure 46. Nondimensional wall jet thickness at $\phi = 0$ as a function of impingement angle.

the margin of experimental error for each curve is variable, with larger errors to be expected for lower velocities. Typical errors based on measurement resolution and estimated effects of unsteadiness appearing at the manometer tubes are judged to fall in the range of 1 to 10 per cent for velocities in the range of 1000 to 100 feet per second. Aside from such errors, it is felt that the only remaining major factor contributing to any observed differences is the lack of a well-formed wall jet for the two axial stations farthest downstream. For $x/d_N = 23.5$ and 39.1 , the values of $r_{.5}$ for the impinging jets are about $.21r_w$ and $.44r_w$, respectively. Allowing for the extent of the full jet profile, it is probable that in these cases the edge of the plate is not sufficiently remote from the impingement interaction regime for a radial flow lacking significant normal components to exist. In this connection, it should be mentioned that a check for nonradial components in the r , ϕ plane was made for several extreme conditions of ϕ and α using the direction-sensitive probe mounted on the rake. It was found that no significant components existed in these cases. Values of the nonradial flow angle β in the r , ϕ plane varied from about 0 or 1 degree at the point of u_{max} to no more than 8 or 9 degrees near $n_{.5}$ in the profile. Thus, no correction for nonradial components of this type was deemed necessary. Because of jet spreading, of course, there is a nonradial component in the n , r plane, but the spreading angle of such a flow is typically so small that this component can also be neglected. The effect on the spreading angle of pressure gradients in the n direction across the edge of the plate was also felt to be of no importance when it was found that surface pressures measured near the edge were essentially equal to ambient pressure. The lack of perfect axial symmetry shown in the data for $\alpha = 90^\circ$ is believed to be

indicative of interference effects caused by the experimental apparatus.

The most striking feature of the behavior of the thickness parameter $n_{.5}$ is its relative invariance with both α and ϕ. In Figure 45, $n_{.5}/(n_{.5})_{\phi=0}$ is plotted vs. ϕ for all the impingement conditions, while the values of $(n_{.5})_{\phi=0}$ are given in Figure 46, in which they are related to the plate radius r_w. The lack of any significant azimuth dependence is indicative of the dominant role of turbulent mixing in governing these flows. It is apparent that, regardless of the initial momentum level of an azimuthal wall jet sector, the spreading rate as determined by mixing is very nearly the same for all sectors. As in the case of other flows with turbulent mixing, of course, a weak dependence upon Mach number might be expected. It is possible that the slight tendency toward increased thickness with increasing ϕ may be due to such an effect, although the scatter in the data makes it difficult to verify this possibility. For cases representing extreme obliqueness ($\alpha = 45^\circ$), even for close range impingement, there is a definite drop-off in thickness as $\phi \rightarrow 180^\circ$. This behavior appears to override any Mach number or Reynolds number effect, each of which would tend to increase the thickness still further. The drop-off is thought to be the result of the decreased effective radial station due to stagnation point shift coupled with the decreased resolution of the velocity profile measurements. It is interesting to note the contrast between an oblique wall jet with turbulent mixing and an inviscid one. In the latter case, in which only inertial and pressure forces act, it is found that the thickness must vary with ϕ in order to produce the required distribution of radial momentum. Thus the downstream portions of such a jet are thicker than the upstream portions by an amount that depends upon the

degree of obliqueness. When turbulent viscous stresses are added, however, the resultant mixing produces a thickness which does not depend on ϕ since the local spreading rate is essentially independent of the local momentum level. Therefore, the required momentum distribution must be produced by changes in the local velocity level.

Azimuthal distributions of radial momentum flux were determined from the measured velocity profiles by graphical integration of the curve in Figure 41. The results are shown in Figures 47 and 48 in which the ratio of momentum flux per radian to its average value for $\alpha = 90^{\circ}$ is plotted as a function of ϕ. As expected, the general behavior is similar in all cases, with a tendency toward less variation with ϕ for increasing impingement distance (Figure 47). For a fixed impingement distance (Figure 48), little effect of jet strength is noted except in the case of the highly underexpanded jet which shows a higher concentration of momentum flux near $\phi = 0$. The average values of the momentum flux per radian for normal impingement are plotted in Figure 49 where they are given in terms of the free jet properties measured at the impingement station.

In order to estimate the validity of the hypothesis that each azimuthal sector of a wall jet is virtually independent of its neighboring sectors so that in the absence of wall friction its radial momentum flux would be conserved, additional velocity profiles were measured for a typical impingement condition with plates having radii equal to 1.5 and 2.0 times the basic plate radius of 4.71 inches. The profile shape at each radius was first checked in detail at $\phi = 0^{\circ}$ for $\alpha = 45^{\circ}$ and 90°. For the typical case $x/d_N = 1.96$ and $p_{\infty}/p^{\circ}_{sc} = .372$, these profiles all appeared to be similar, both to each

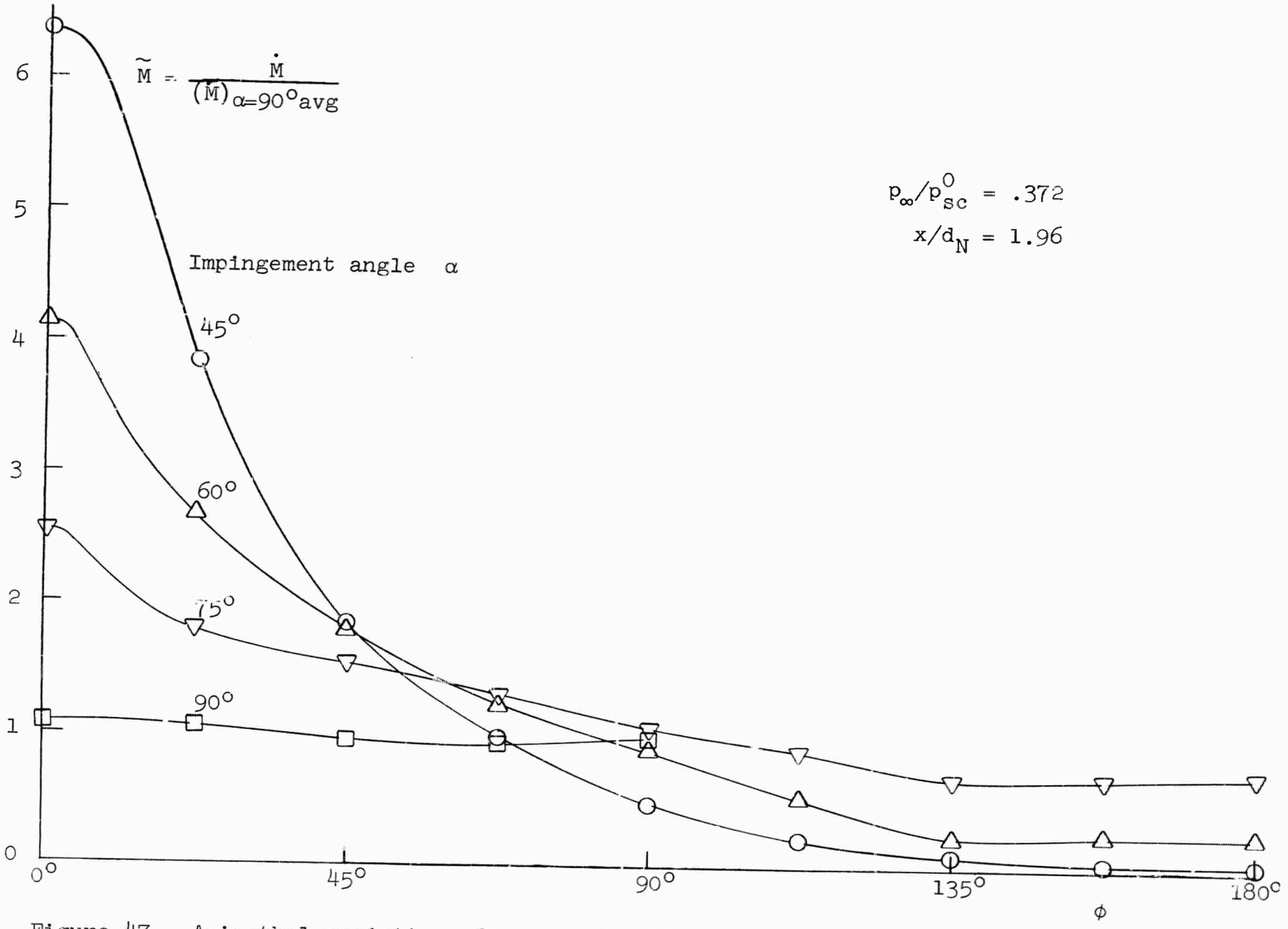

Figure 47. Azimuthal variation of measured wall jet momentum flux.

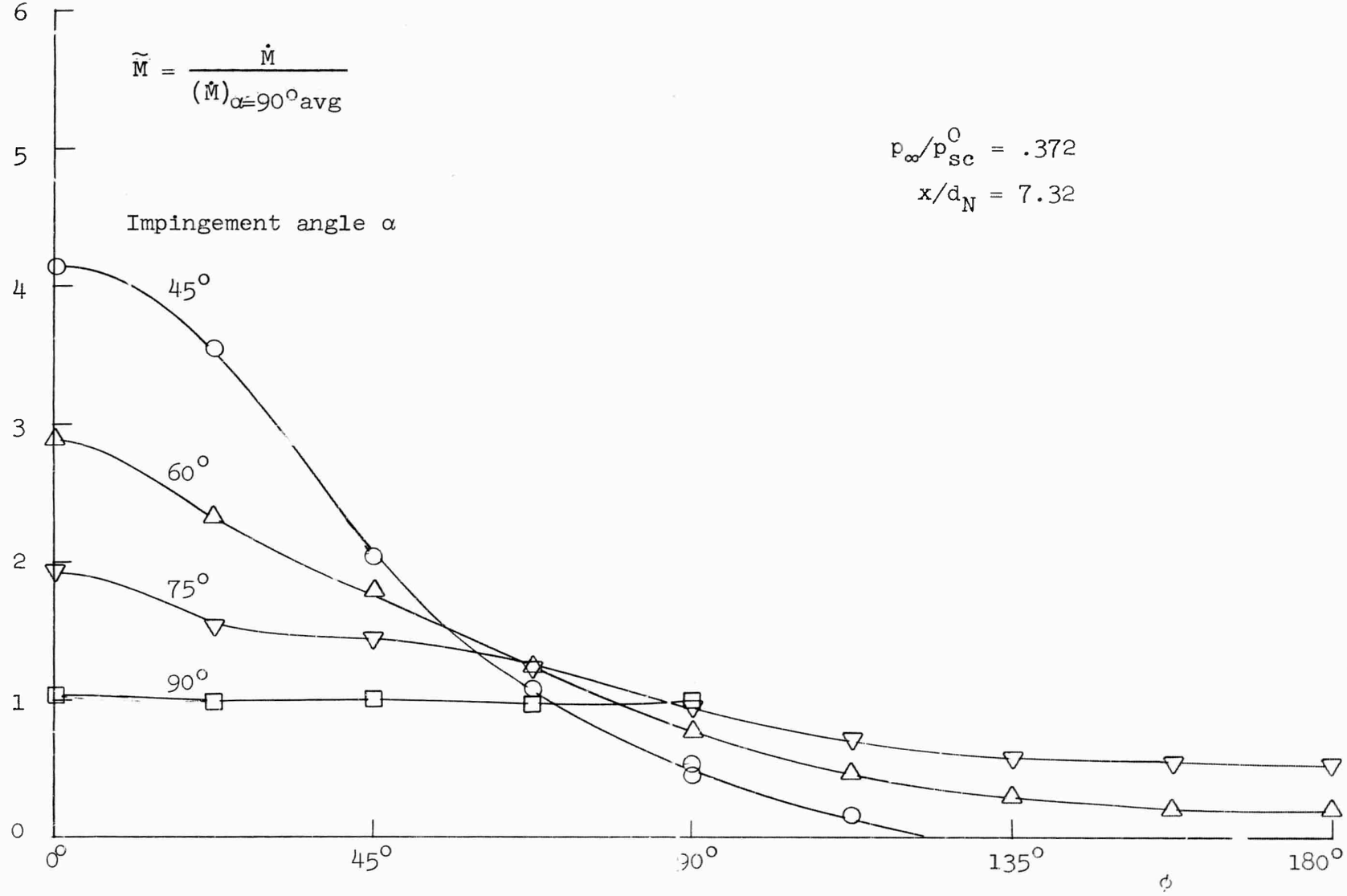

Figure 47. (Continued)

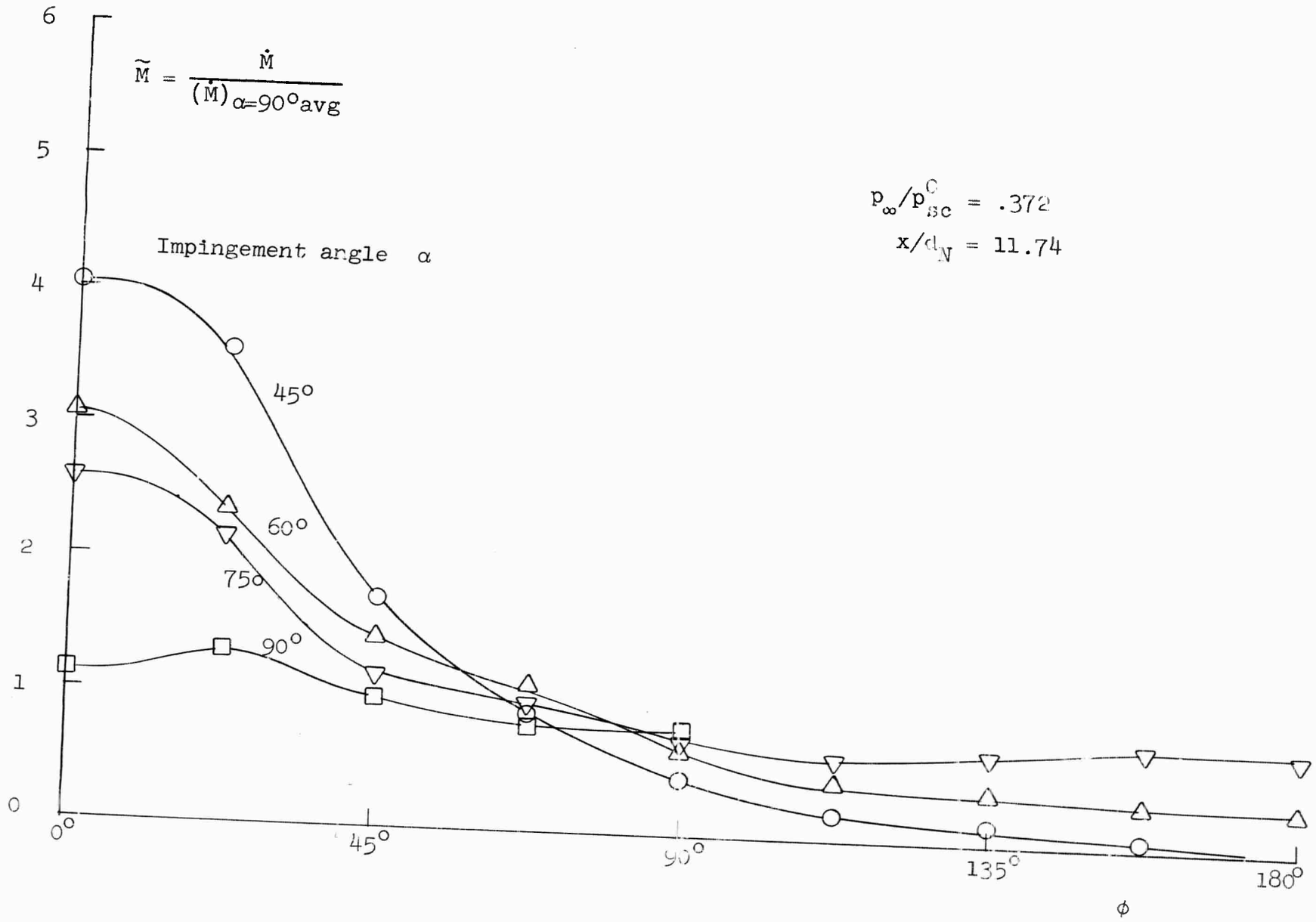

Figure 47. (Continued)

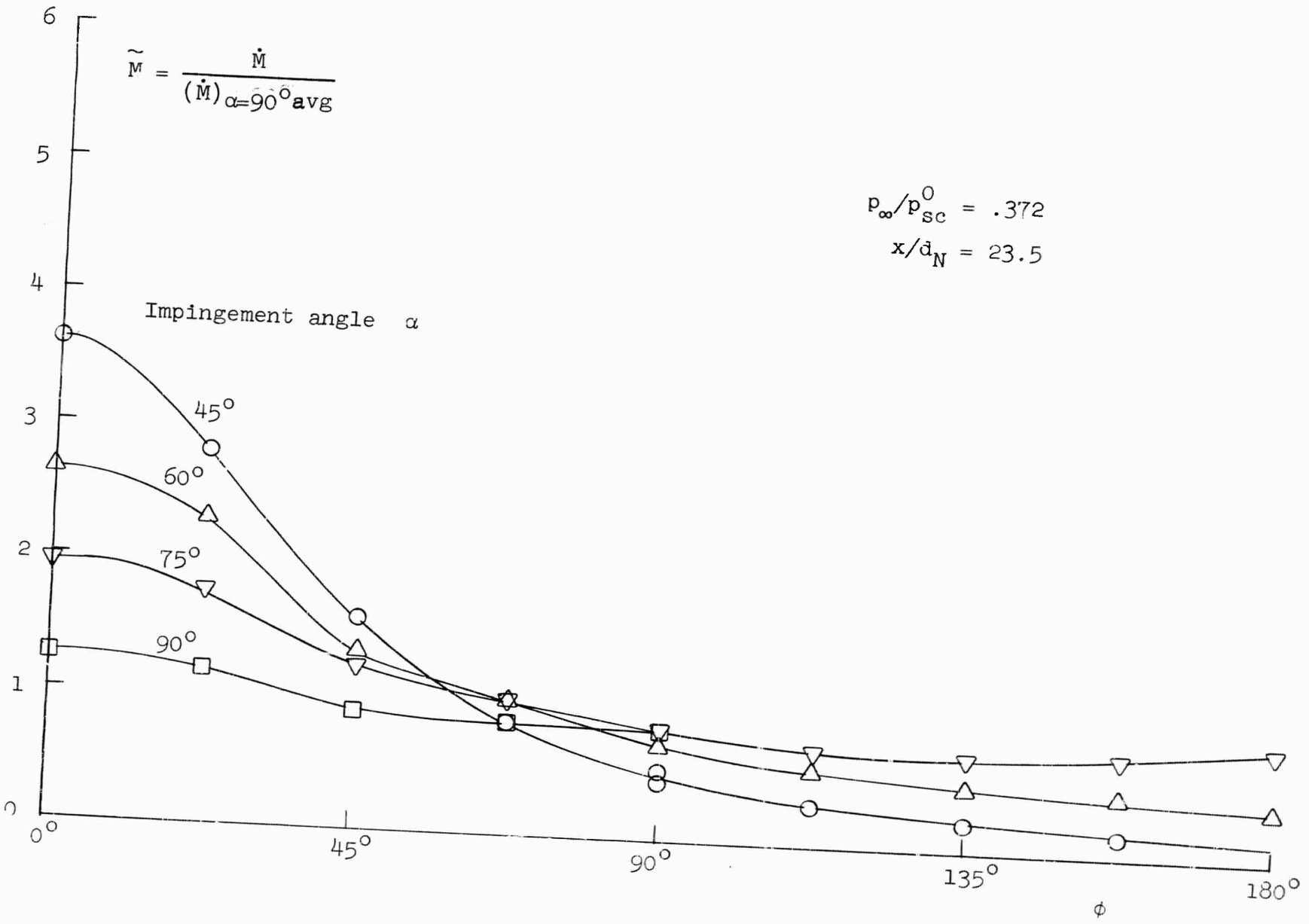

Figure 47. (Continued)

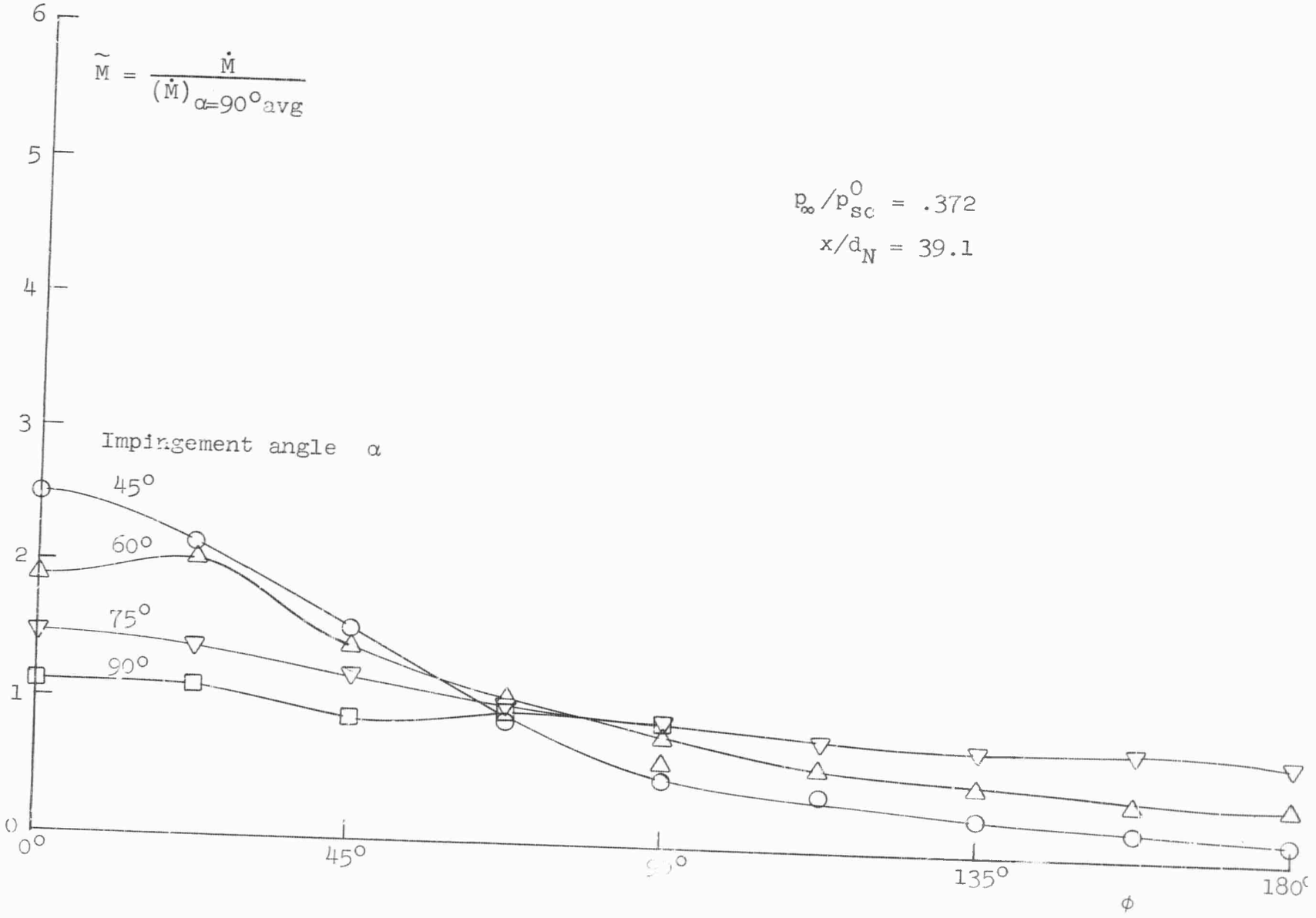

Figure 47. (Concluded)

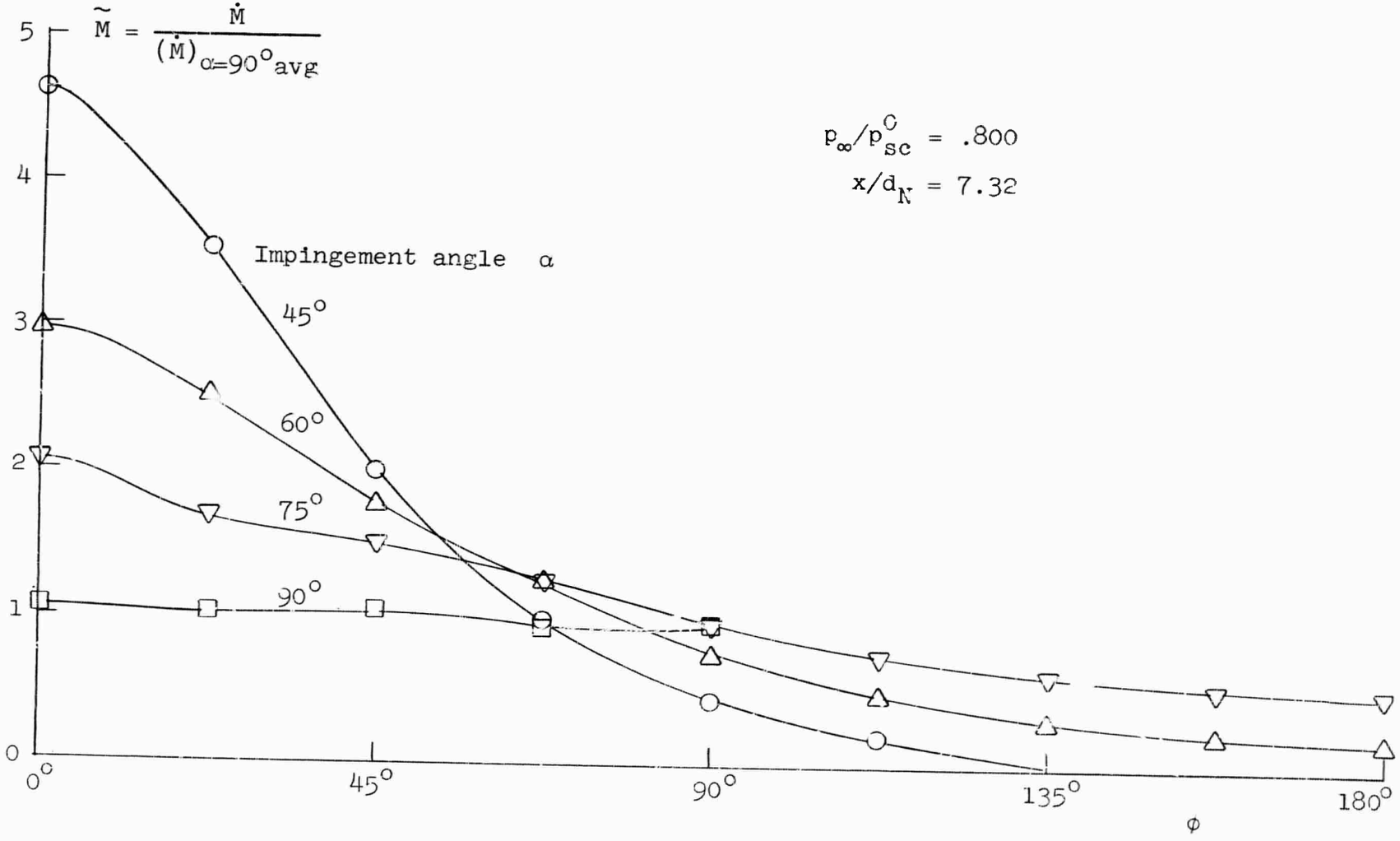

Figure 48. Azimuthal variation of measured wall jet momentum flux.

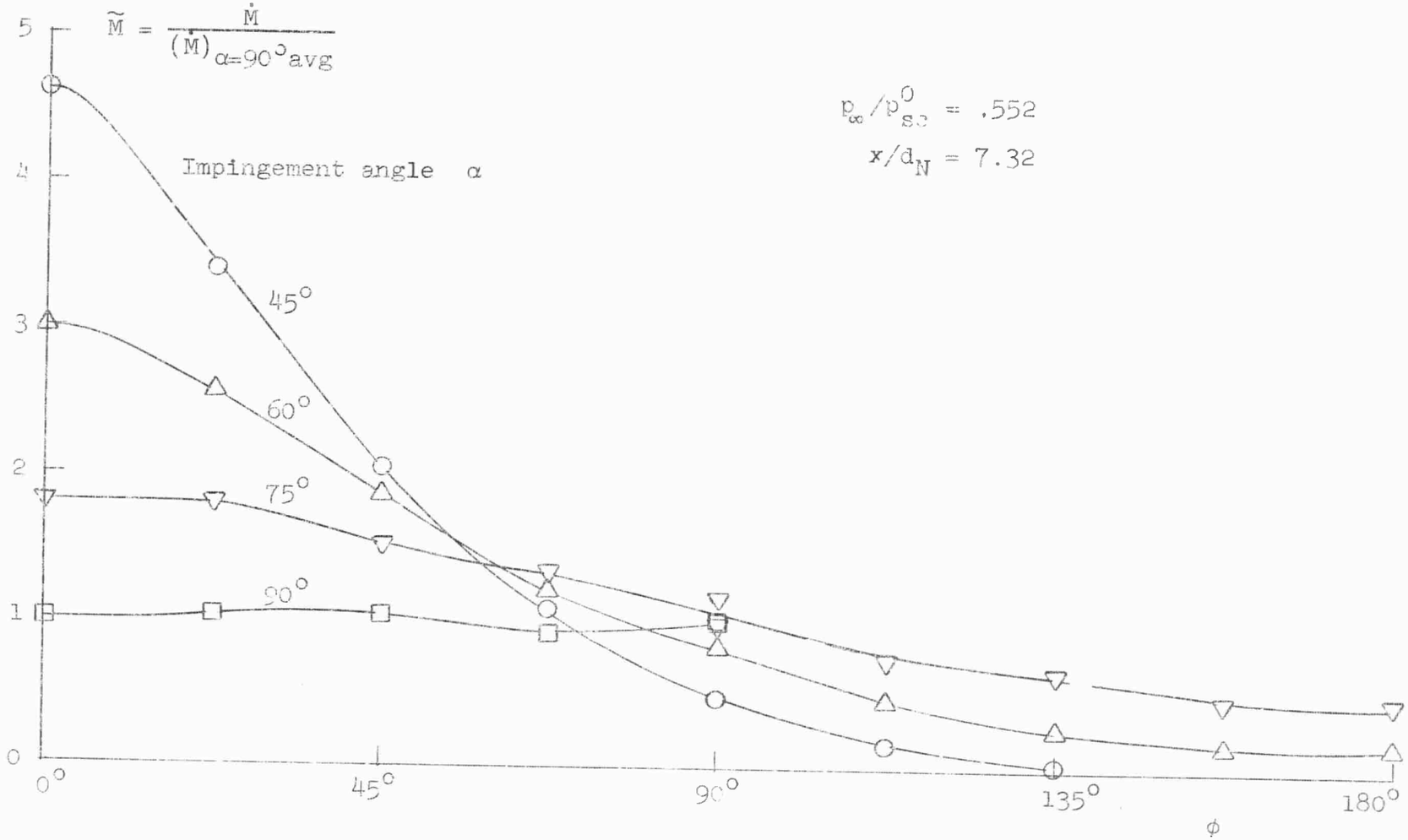

Figure 48. (Continued)

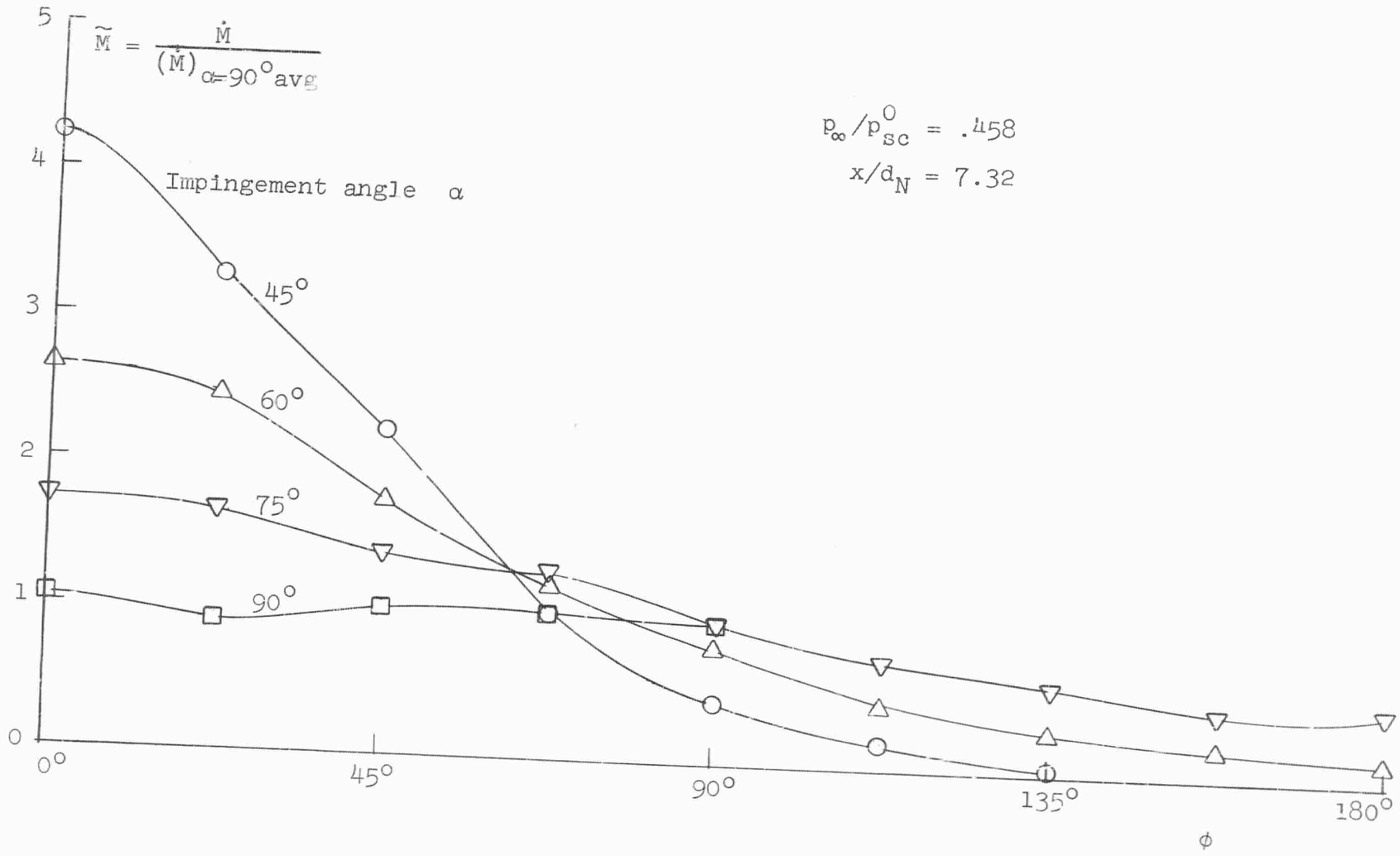

Figure 48. (Continued)

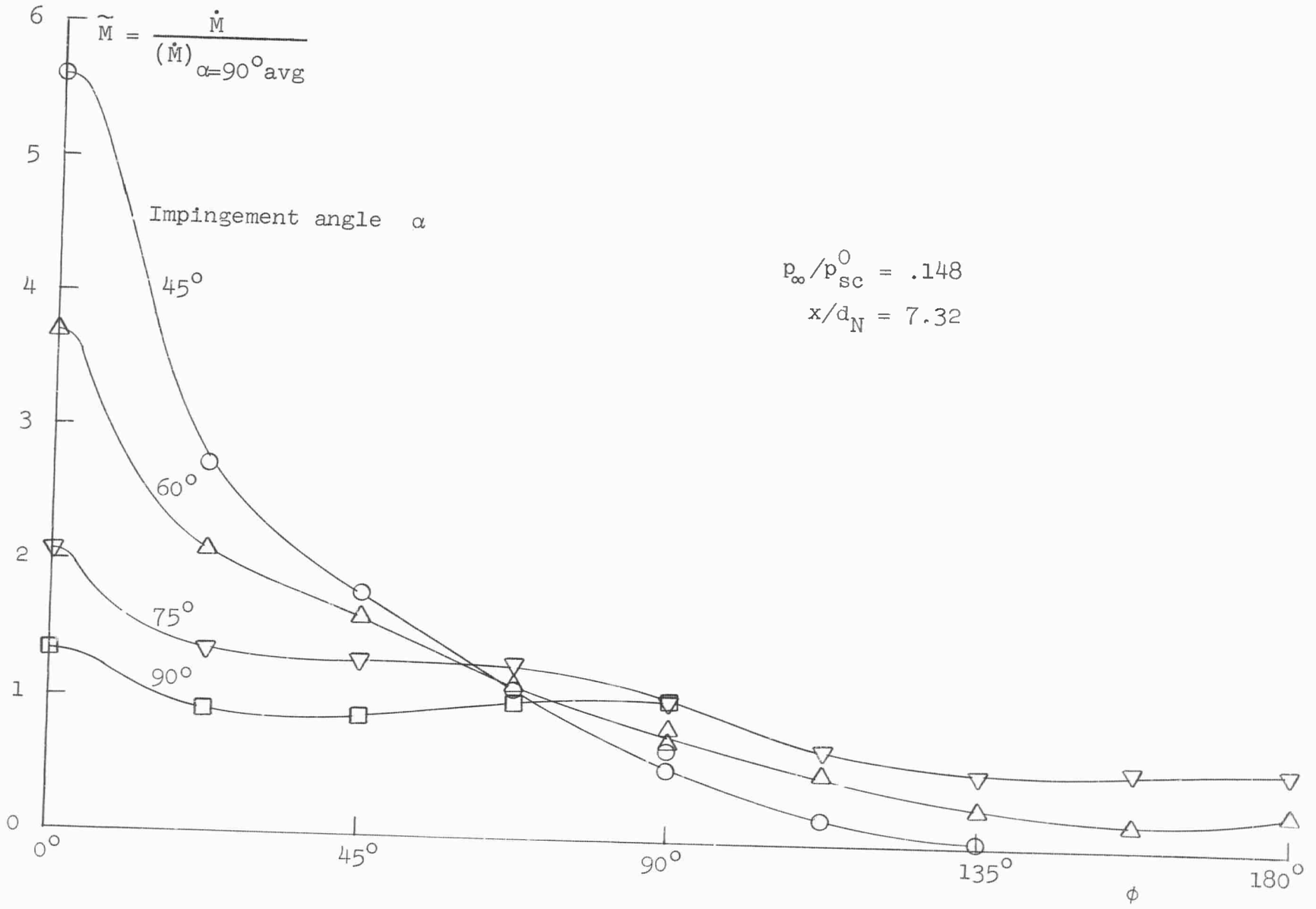

Figure 48. (Concluded)

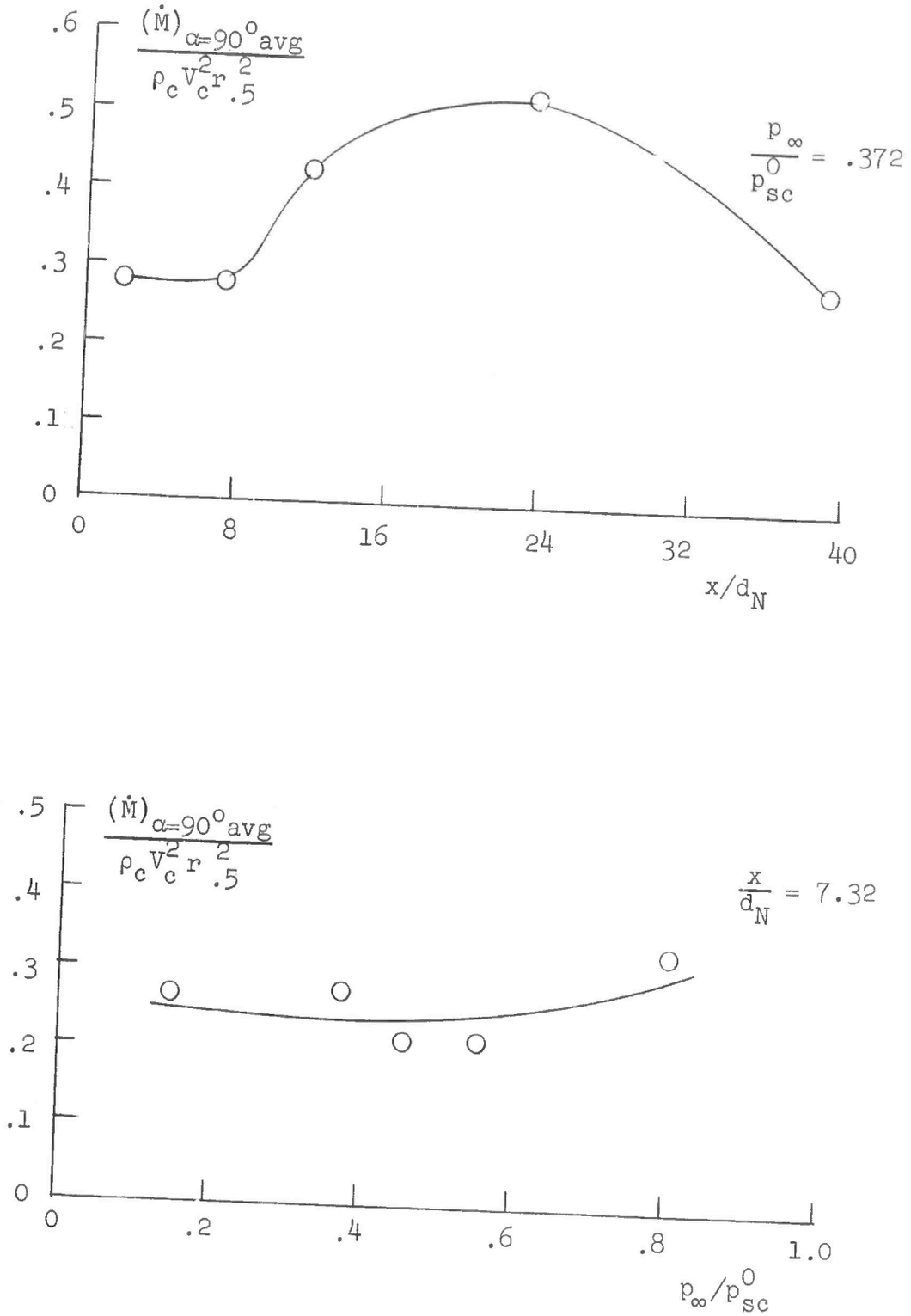

Figure 49. Nondimensional average values of wall jet momentum flux for normal impingement.

other and to the profile already established from the more detailed study with the smallest plate (Figure 50). Although Glauert's analysis shows that the ratio of thicknesses of the inner and outer layers changes slightly as r_w increases, no such changes are apparent in the data. Therefore, for the present comparison, the same basic nondimensional velocity profile was assumed to apply for all three plate sizes. In addition, the wall jet was assumed to be incompressible for the two larger plates. Under these conditions, the integral expression for the radial momentum flux per radian around the plate can be written as

$$\dot{M}(\phi) = \rho u_{max}^2 r_w n_{.5} \int_0^\infty \left(\frac{u}{u_{max}}\right)^2 d\left(\frac{n}{n_{.5}}\right)$$

$$= \rho u_{max}^2 r_w n_{.5} I_{wj}$$

where I_{wj} is evaluated uniquely from the basic wall jet profile. If the momentum loss in the boundary layer is neglected, it can then be shown that wall jet momentum is conserved if the product $u_{max}^2 r_w n_{.5}$ is invarient with r_w.

Values of $n_{.5}$ and u_{max} were measured for a range of the impingement angle at $\phi = 0^\circ$ and 180° for the given impingement condition. These values are plotted against r_w/r_{w_1} in Figure 51 in which $n_{.5}$ is given in the nondimensional form $n_{.5}/r_w$ and u_{max} is made nondimensional by means of the local impinging jet parameters $V_c r_{.5}$; the quantity r_{w_1} is the radius of the smallest plate.

When the momentum coefficient $u_{max}^2 r_w n_{.5}$ is computed from the measured data, it is found to be very nearly independent of r_w. These values are plotted at the bottom of Figure 51. On the basis of these results, it

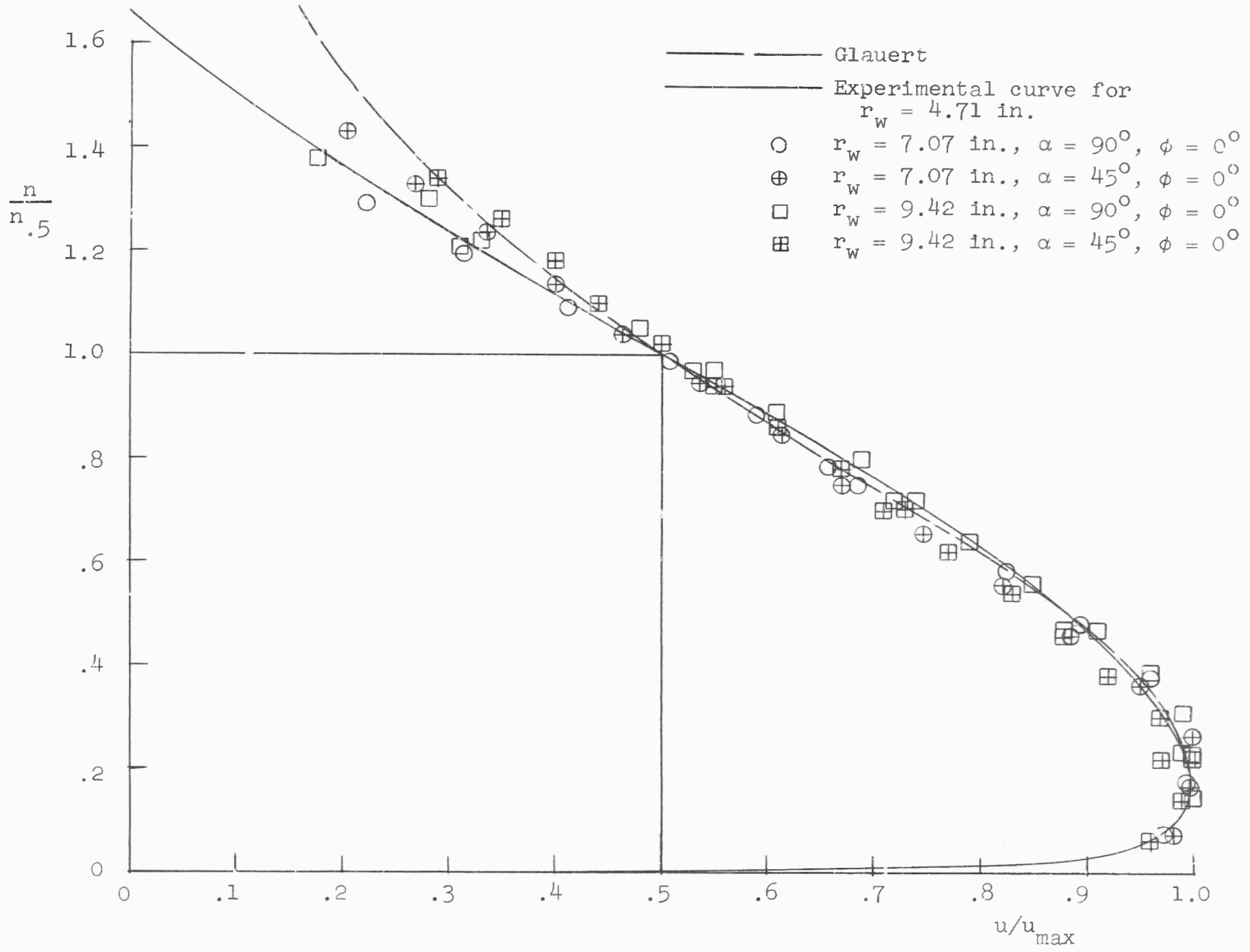

Figure 50. Nondimensional wall jet velocity profile for several different plate radii.

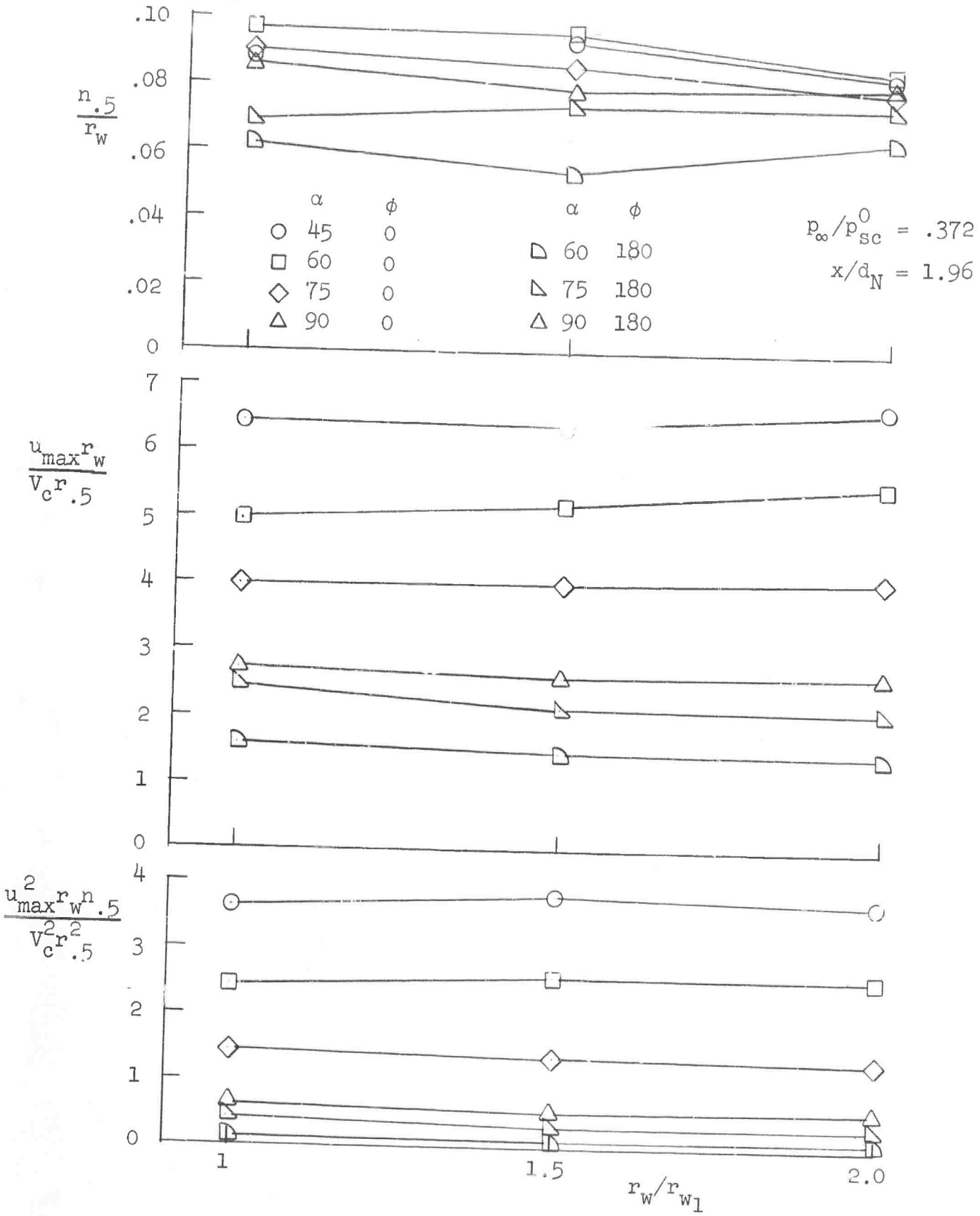

Figure 51. Dependence of wall jet characteristics on radial location.

appears that the two wall jet sectors in question ($\phi = 0^\circ$ and 180°) were in no way coupled to their neighboring sectors. In addition, this conclusion holds true regardless of changes in momentum level produced by variation of the impingement angles.

In view of the observed momentum conservation for two wall jet sectors, a similar condition may be inferred for the remaining sectors if it is assumed that for a given α the azimuthal distribution of momentum flux per radian established earlier for the smallest plate (Figures 47 and 48) remains the same at larger radii. If changes in the distribution of shearing stresses within the wall jet are neglected, the primary cause for any apparent change in this distribution of $\dot{M}(\phi)$ would be the failure to allow for nonradial velocity components in the measured profiles. Since such components were found to be negligible for the smallest radius, it is felt that the assumption of sector independence is physically reasonable.

2.6. Mass, Momentum, and Energy Flux Balances.

The data just presented may be used as the basis for a comparison between flux values measured in the wall jet at the edge of the plate and those at the nozzle exit. A comparison of this kind is useful in understanding the over-all flow behavior and also provides a check on the validity of the measurements. A sketch of a typical impinging jet flow system is shown in Figure 52 for $\alpha = 90^\circ$ (axially symmetric case). It is clear that the mass flux entering the cylindrical control volume includes that issuing from the nozzle as well as that entrained across surfaces AB and S. The mass flux leaving is contained in the wall jet which consists of

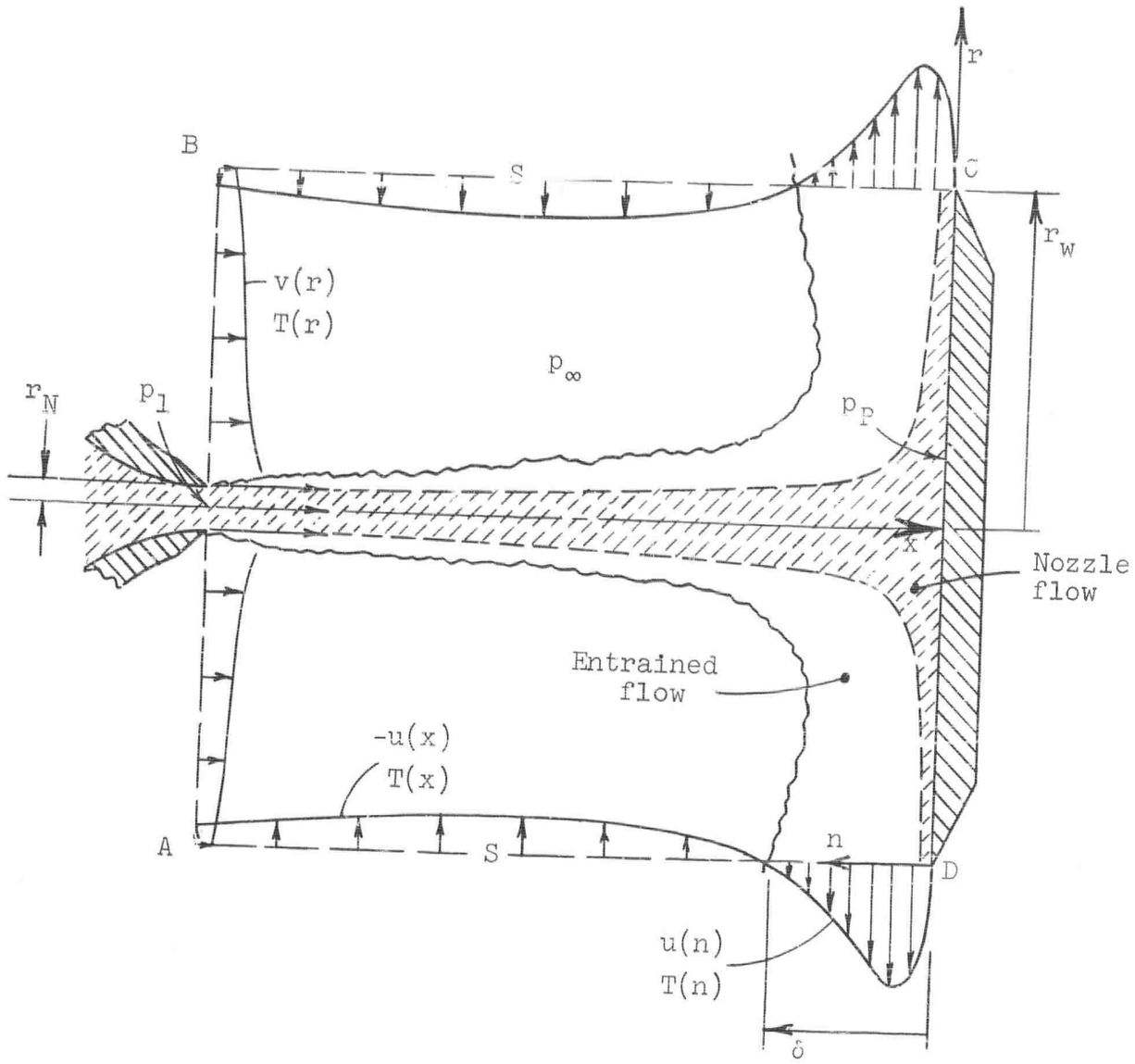

Figure 52. Sketch of impinging jet flow system.

both nozzle flow and entrained flow. Expressed in terms of velocity integrals, the mass flux balance is given by

$$2\pi\int_0^{r_N} \rho(r)v(r)rdr + 2\pi\int_{r_N}^{r_w} \rho(r)v(r)rdr - 2\pi r_w\int_0^{x-\delta} \rho(x)u(x)dx = 2\pi r_w\int_0^{\varepsilon} \rho(n)u(n)dn \qquad (2)$$

where the coordinate n normal to the plate has been retained for the wall jet portion.

The momentum flux balance in the axial direction may be closely approximated by neglecting viscous and pressure forces at the free boundaries, except for the pressure difference across the nozzle exit. The axial components of momentum entering the volume across surfaces AB and S plus any nozzle pressure differences are thus balanced by the pressure force normal to the plate plus any reversed axial component at S due to spreading of the wall jet. Neglecting this latter component, the momentum flux balance may be expressed as

$$2\pi\int_0^{r_N} [\rho(r)v^2(r) + (p_1(r)-p_\infty)]rdr + 2\pi\int_{r_N}^{r_w} \rho(r)v^2(r)rdr - 2\pi r_w\int_0^{x-\delta} \rho(x)u(x)v(x)dx = 2\pi\int_0^{r_w} [p_p(r)-p_\infty]rdr \qquad (3)$$

For the case of normal impingement being considered, the radial flow is axially symmetric, so that no net force can act due to radial momentum flux.

Similar expressions may be deduced for the balance of energy. In this case we consider both kinetic and thermal energy terms and assume the flow to be both adiabatic and free of forces doing work on the boundaries of the control volume. The energy flux balance is thus made between the sum of nozzle and entrained flow energy entering the volume and that leaving via the wall jet. The integral form of this balance is

$$2\pi\int_0^{r_N}\left[\tfrac{1}{2}\rho(r)v^3(r) + c_pT(r)\rho(r)v(r)\right]rdr + 2\pi\int_{r_N}^{r_w}\left[\tfrac{1}{2}\rho(r)v^3(r) + c_pT(r)\rho(r)v(r)\right]rdr - 2\pi r_w\int_0^{x-\delta}\left[\tfrac{1}{2}\rho(x)u^3(x) + c_pT(x)\rho(x)u(x)\right]dx = 2\pi r_w\int_0^{\delta}\left[\tfrac{1}{2}\rho(n)u^3(n) + c_pT(n)\rho(n)u(n)\right]dn \qquad (4)$$

If the impingement is oblique, the above equations are no longer valid because of complications introduced by the lack of axial symmetry.

The data for one of the experimental impingement cases have been used to compute these balances in order to illustrate typical flow relationships. The case chosen was that for $p_\infty/p^o_{sc} = .372$ at $x/d_N = 1.96$. In order to simplify the procedure, perfect axial symmetry was assumed for the wall jet so that a single measured velocity profile could be used to evaluate the necessary integrals. (As can be seen in Figure 43, there was some variation from perfect symmetry for $\alpha = 90^o$.) The mass

fluxes computed for this flow condition were

$$\text{nozzle mass flux} = .582 \times 10^{-2} \text{ slug/sec}$$

$$\text{wall jet mass flux} = 3.583 \times 10^{-2} \text{ slug/sec}$$

The entrained flow thus constitutes about 84 per cent of the wall jet. It is found for just this particular case that the original nozzle flow occupies a layer approximately equal in thickness to the viscous boundary layer portion of the u profile.

A balance of axial momentum flux against plate pressure force was made for this case in [1]. It was found that the measured jet momentum flux of 7 lbs. could only account for a little over one-half of the total force (13 lbs.) on the plate, with the rest presumably coming from entrained flow across AB outside of the nozzle, i.e. between r_N and r_w.

The complete energy balance cannot be made on the basis of the velocity profiles alone. It is of interest, however, to evaluate some of the terms of Equation 4 and to note the relative importance of kinetic and thermal energy in the various portions of the flow. At the nozzle exit, the total energy is

$$\dot{H}_N = (\dot{h}_{kin} + \dot{h}_{therm})_N$$

$$= .308 \times 10^4 + 1.54 \times 10^4 = 1.848 \times 10^4 \text{ ft-lb/sec}$$

wherein kinetic energy accounts for about 17 per cent of the total. In the wall jet, however, the proportion of kinetic energy is much smaller. Assuming a constant temperature in the wall jet equal to ambient, the total energy is

$$\dot{H}_{wj} = (\dot{h}_{kin} + \dot{h}_{therm})_{wj}$$

$$= .0437 \times 10^4 + 11.40 \times 10^4 = 11.44 \times 10^4 \text{ft-lb/sec}$$

Kinetic energy is thus only .4 per cent of the total. Further, it is found that the kinetic energy remaining in the mass flow that originated at the nozzle exit constitutes only 22 per cent of the total wall jet kinetic energy. These figures are indicative of the effectiveness with which kinetic energy is dissipated in an impinging turbulent flow of this kind.

The details of oblique impingement flow processes revealed by the measurements have already been discussed for both the impingement and wall jet regimes. Some of the more important features of these results will now be reviewed.

The effects of obliqueness on impingement pressure distribution were found to be generally similar for all three jets at all axial stations except the closest ($x/d_N = 1.96$). These effects were characterized by changes in the stagnation point pressure level and a shift in its position on the plate surface. For the downstream stations representing impingement of essentially fully developed jet velocity profiles, the stagnation point pressure was relatively insensitive to impingement angle in the range $90^\circ \geq \alpha \geq 75^\circ$. For smaller angles, the observed drop-off became nearly linear. The over-all behavior exhibited roughly a $\sin^2\alpha$-dependence. For impingement of the jet core, little change in pressure level was noted until α was decreased below 60°. The shift of the stagnation point also followed a similar pattern. Downstream locations showed a fairly linear change with α in the range $90^\circ \geq \alpha \geq 60^\circ$. At $x/d_N = 1.96$, a higher rate of change was generally observed through the entire α range. It is apparent that the different behavior observed for core impingement is due to the flat velocity profile in that portion of the free jet.

The stagnation point radial velocity gradient $[(du_e/dr)_{r=0}]_1$ was next computed for each pressure distribution. Again, a similarity was revealed in the α-dependence for all three jet strengths, and here, too, the case of core impingement was found to differ from the others. In general, a steady drop in $[(du_e/dr)_{r=0}]_1$ was observed for increasing obliqueness, with a tendency

toward less α-dependence with increasing impingement distance. For core impingement, very little change was noted for $90^\circ \geq \alpha \geq 75^\circ$. For smaller angles, however, a distinct increase appeared with a peak value occurring near $\alpha = 60^\circ$ for two of the three jets. Data for the moderately underexpanded jet were not sufficient to define this peak, although they did show the increase. The actual magnitude of $[(du_e/dr)_{r=0}]_1$ was found to depend on jet strength. Values for the moderately underexpanded jet were higher than those for the subsonic jet for corresponding axial locations and impingement angles. Such differences in magnitude, however, diminished with increasing impingement distance. The highly underexpanded jet gave higher values throughout except for cases of normal or near-normal impingement at $x/d_N = 1.96$, where lower values typical of the two weaker jets were found. These latter cases are thought to be the result of the strong stand-off shock occurring for this condition. It is apparent that for highly oblique flows the effect of this shock in flattening the pressure distribution is altered enough to produce a much sharper maximum pressure peak leading to a higher value of $[(du_e/dr)_{r=0}]_1$. When the axial distance is increased to $x/d_N = 7.32$, normal impingement produces the separated stagnation point flow discussed earlier. The central peak of this distribution thus produces a negative value of $[(du_e/dr)_{r=0}]_1$. As obliqueness is introduced, the distribution appears to change until at some angle the stagnation point of the separated region can no longer be distinguished. The outer peaks due to the supersonic flow surrounding the core then become highly asymmetric. Because of the highly complex flow structure under such conditions, it was felt that meaningful values of $[(du_e/dr)_{r=0}]_1$ for this case could not be deduced from the available data.

The correlation of values of $[(du_e/dr)_{r=0}]_1$ with local free jet conditions at the impingement station was found to be somewhat inconsistent. In general, however, a decreasing trend was noted in the value of the nondimensional form $(r_{.5}/V_c)/[(du_e/dr)_{r=0}]_1$ as obliqueness increased for all the jets at all but the closest impingement distance. For $90^\circ \geq \alpha \geq 75^\circ$, at $x/d_N = 1.96$, nondimensional values correlated quite well, while the behavior for $\alpha < 75^\circ$ was similar to that for $[(du_e/dr)_{r=0}]_1$ alone with peaks of different magnitudes near $\alpha = 60^\circ$.

The azimuthal distribution of the wall jet was found to be essentially as expected, with more mass and momentum flux concentrated near $\phi = 0$ for increased obliqueness (decreased α). Distributions of radial momentum flux per radian revealed little difference among the impingement conditions except far downstream where there was less dependence on ϕ for a given α. At a fixed distance, the flux of the highly underexpanded jet tended to be more concentrated near $\phi = 0$ than that of the weaker jets.

Wall jet velocity profiles were characterized by their maximum velocities u_{max} and half-velocity thicknesses $n_{.5}$. Similar results were obtained under all conditions except, again, for stations far downstream. In general, u_{max} dropped off more rapidly with ϕ for smaller values of α, whereas $n_{.5}$ was found to be relatively independent of both ϕ and α. This constant thickness, of course, reflects the relative insensitivity of the rate of wall jet spread to its momentum level. Variations from the general behavior for downstream locations were felt to be at least partly the result of the large extent of the impingement regime relative to the plate size. Under these conditions, it is doubtful if a fully developed wall jet was formed at the point of

measurement.

The over-all shape of the velocity profile was also found to be similar in all those cases for which it was determined in detail. A comparison of the measured profiles with one computed using Glauert's method showed excellent agreement (Figure 41) except in the outer edge where the measurement technique was of little value.

Measurements of the velocity profile at two larger radii indicated that, for the wall jet sectors involved ($\phi = 0^{\circ}$ and 180°), the decay behavior was virtually independent of that in the neighboring sectors.

This investigation was made to study the properties of the flow produced by an axially symmetric jet impinging obliquely on a circular flat plate. In the region of strong interaction close to the impingement point, surface pressure distributions were measured along a diameter normal to the plate tilt axis for a variety of conditions. In the region of the wall jet produced by the interaction, velocity profiles were measured. These measurements revealed several important features of oblique impingement flows. In addition, it was possible to compare these features with those investigated previously for normal impingement alone. In this previous study [1], the radial velocity gradient $(du_e/dr)_{r=0}$ at the stagnation point of the impinging flow was evaluated from the pressure distributions near the impingement point. It was found that values of $(du_e/dr)_{r=0}$ could be correlated with the properties of the free jet at the plane of impingement, thereby providing a means of estimating such values for any known jet flow. For oblique impingement, however, several factors were observed which alter the normal result. These factors include changes in the pressure distribution shape, the pressure level, the position of the stagnation point, and the introduction of a dependence of $(du_e/dr)_{r=0}$ on ϕ. In addition, the distributions of mass and momentum fluxes in the resulting wall jet are no longer axially symmetric.

In general, the pressure distribution shape becomes flatter and slightly asymmetric as impingement angle decreases through the range $90^\circ \geq \alpha \geq 45^\circ$. The exact nature of these changes is found to depend upon the impingement condition as determined by jet strength and impingement distance. The shock structure of underexpanded jets does produce local changes in the pressure distributions when impingement occurs within the region containing

shocks.

For impingement at distances greater than the jet core length, no substantial change in stagnation point pressure level is observed for any of the jets tested until α is less than 75°. Beyond this point, a steady drop-off occurs.

The stagnation point shift also depends very little on jet strength, there being a fairly linear dependence on α for most of the range investigated ($90^{\circ} \geq \alpha \geq 45^{\circ}$). This dependence is stronger, however, when the core impinges.

Because of the ϕ-dependence of the stagnation point radial velocity gradient under conditions of oblique impingement, the values measured for a single value of ϕ are designated as $[(du_e/dr)_{r=0}]_1$. When this gradient is nondimensionalized with local free jet properties, a general decrease is observed as α decreases for all cases except those for which the jet core impinges. For $\alpha = 45^{\circ}$, the value of $(r_{.5}/V_c)[(du_e/dr)_{r=0}]_1$ may be as low as 50 per cent of its value for $\alpha = 90^{\circ}$. For core impingement, the exact behavior depends upon the local character of the core as determined by the jet strength.

Measurements of wall jet velocity profiles show that at a given radial distance, the thickness $n_{.5}$ varies only slightly with azimuthal position ϕ for a wide range of impingement conditions ($1.96 \leq x/d_N \leq 39.1$, $90^{\circ} \geq \alpha \geq 45^{\circ}$, and $p_{\infty}/p^{o}_{sc} = .800, .372$, and $.148$). Only for the largest impingement distance -- where there is doubt as to the development of the wall jet -- is there any marked dependence of $n_{.5}$ on ϕ or α. In addition, the basic profile shape remains essentially similar for all azimuthal stations when nondimensionalized on the half-velocity thickness and the maximum velocity. This similarity also holds for typical profiles measured at radii of 1.5 and 2 times the initial radius.

Azimuthal distributions of radial momentum flux per radian in the wall jet are found to depend strongly on impingement angle. Flux distributions increase near $\phi = 0$ as α decreases. For a given jet strength, this increase diminished as impingement distance increased. For a fixed distance, however, there was only a slight change in the distributions as jet strength increased. This change was marked by an increase in the concentration of momentum flux near $\phi = 0$ when the jet with the highest momentum level impinged $(p_\infty/p^o_{sc} = .148)$.

A check of the wall jet momentum flux level at two larger radii revealed that, to first order, the decay behavior of each azimuthal wall jet sector was independent of its neighbors.

1. Snedeker, R.S., and Donaldson, C.duP. Experiments on free and impinging underexpanded jets from a convergent nozzle. Aeronautical Research Associates of Princeton, Inc. Report No. 63, September 1964.

2. Anderson, A.R., Johns, F.R., and Hawkes, W.M. Nondimensional characteristics of free and deflected supersonic jets exhausting into quiescent air. U.S. Naval Air Development Center, NADC-ED-5401, 1954.

3. Henderson, L.F. The impingement of a supersonic jet on a flat plate. Australian Defence Scientific Service, Department of Supply, Mech. Engineering Note 233.

4. Stitt, L.E. Interaction of highly underexpanded jets with simulated lunar surfaces. NASA TN D-1095, 1961.

5. Vick, A.R., and Andrews, E.H. An experimental investigation of highly underexpanded free jets impinging upon a parallel flat surface. NASA TN D-2326, 1964.

6. Glauert, M.B. The wall jet. J. Fluid Mech. 1, 6, 625-643, (1956).

Unclassified
Security Classification

DOCUMENT CONTROL DATA - R&D
(Security classification of title, body of abstract and indexing annotation must be entered when the overall report is classified)

1. ORIGINATING ACTIVITY (Corporate author)
Aeronautical Research Associates of Princeton, Inc.
50 Washington Road
Princeton, New Jersey 08540

2a. REPORT SECURITY CLASSIFICATION
Unclassified

2b. GROUP
N/A

3. REPORT TITLE
Experiments on the Oblique Impingement of Underexpanded Jets on a Flat Plate.

4. DESCRIPTIVE NOTES (Type of report and inclusive dates)

5. AUTHOR(S) (Last name, first name, initial)
Snedeker, Richard S. and Donaldson, Coleman duP.

6. REPORT DATE
April 1965

7a. TOTAL NO. OF PAGES
112

7b. NO. OF REFS
6

8a. CONTRACT OR GRANT NO.
Nonr-3903(00)(X)

b. PROJECT NO.

c. ARPA Order No. 149-60

d. NRL Req. No. 00173-3-006031

9a. ORIGINATOR'S REPORT NUMBER(S)
ARAP Report No. 64

9b. OTHER REPORT NO(S) (Any other numbers that may be assigned this report)

10. AVAILABILITY/LIMITATION NOTICES
Qualified requesters may obtain copies of this report from DDC.

11. SUPPLEMENTARY NOTES

12. SPONSORING MILITARY ACTIVITY
ARPA through NRL

13. ABSTRACT

An experimental investigation was made of the general behavior of an air jet impinging obliquely on a circular flat plate. Surface pressure distributions and velocity profiles of the resulting wall jet were measured. Typical stagnation point radial velocity gradients, their dependence on impingement angle, and their correlation with local free jet properties were also determined. Throughout the range of impingement angles studied ($90^\circ \geq \alpha \geq 45^\circ$), the wall jet thickness was found to be relatively constant around the plate perimeter. The azimuthal variation of momentum flux per radian depended strongly on impingement angle and only slightly on jet strength and impingement distance.

DD FORM 1 JAN 64 1473

Unclassified
Security Classification

14. KEY WORDS	LINK A		LINK B		LINK C	
	ROLE	WT	ROLE	WT	ROLE	WT
Jet impingement Radial wall jet Oblique impingement						

INSTRUCTIONS

1. ORIGINATING ACTIVITY: Enter the name and address of the contractor, subcontractor, grantee, Department of Defense activity or other organization *(corporate author)* issuing the report.

2a. REPORT SECURITY CLASSIFICATION: Enter the overall security classification of the report. Indicate whether "Restricted Data" is included. Marking is to be in accordance with appropriate security regulations.

2b. GROUP: Automatic downgrading is specified in DoD Directive 5200.10 and Armed Forces Industrial Manual. Enter the group number. Also, when applicable, show that optional markings have been used for Group 3 and Group 4 as authorized.

3. REPORT TITLE: Enter the complete report title in all capital letters. Titles in all cases should be unclassified. If a meaningful title cannot be selected without classification, show title classification in all capitals in parenthesis immediately following the title.

4. DESCRIPTIVE NOTES: If appropriate, enter the type of report, e.g., interim, progress, summary, annual, or final. Give the inclusive dates when a specific reporting period is covered.

5. AUTHOR(S): Enter the name(s) of author(s) as shown on or in the report. Enter last name, first name, middle initial. If military, show rank and branch of service. The name of the principal author is an absolute minimum requirement.

6. REPORT DATE: Enter the date of the report as day, month, year; or month, year. If more than one date appears on the report, use date of publication.

7a. TOTAL NUMBER OF PAGES: The total page count should follow normal pagination procedures, i.e., enter the number of pages containing information.

7b. NUMBER OF REFERENCES: Enter the total number of references cited in the report.

8a. CONTRACT OR GRANT NUMBER: If appropriate, enter the applicable number of the contract or grant under which the report was written.

8b, 8c, & 8d. PROJECT NUMBER: Enter the appropriate military department identification, such as project number, subproject number, system numbers, task number, etc.

9a. ORIGINATOR'S REPORT NUMBER(S): Enter the official report number by which the document will be identified and controlled by the originating activity. This number must be unique to this report.

9b. OTHER REPORT NUMBER(S): If the report has been assigned any other report numbers *(either by the originator or by the sponsor)*, also enter this number(s).

10. AVAILABILITY/LIMITATION NOTICES: Enter any limitations on further dissemination of the report, other than those imposed by security classification, using standard statements such as:

(1) "Qualified requesters may obtain copies of this report from DDC."

(2) "Foreign announcement and dissemination of this report by DDC is not authorized."

(3) "U. S. Government agencies may obtain copies of this report directly from DDC. Other qualified DDC users shall request through _____."

(4) "U. S. military agencies may obtain copies of this report directly from DDC. Other qualified users shall request through _____."

(5) "All distribution of this report is controlled. Qualified DDC users shall request through _____."

If the report has been furnished to the Office of Technical Services, Department of Commerce, for sale to the public, indicate this fact and enter the price, if known.

11. SUPPLEMENTARY NOTES: Use for additional explanatory notes.

12. SPONSORING MILITARY ACTIVITY: Enter the name of the departmental project office or laboratory sponsoring *(paying for)* the research and development. Include address.

13. ABSTRACT: Enter an abstract giving a brief and factual summary of the document indicative of the report, even though it may also appear elsewhere in the body of the technical report. If additional space is required, a continuation sheet shall be attached.

It is highly desirable that the abstract of classified reports be unclassified. Each paragraph of the abstract shall end with an indication of the military security classification of the information in the paragraph, represented as *(TS)*, *(S)*, *(C)*, or *(U)*.

There is no limitation on the length of the abstract. However, the suggested length is from 150 to 225 words.

14. KEY WORDS: Key words are technically meaningful terms or short phrases that characterize a report and may be used as index entries for cataloging the report. Key words must be selected so that no security classification is required. Identifiers, such as equipment model designation, trade name, military project code name, geographic location, may be used as key words but will be followed by an indication of technical context. The assignment of links, roles, and weights is optional.

DD FORM 1 JAN 64 1473 (BACK)